APPLIED PHYSICS

2`25



Applied Physics 2025, No. 2

The journal was founded in 1994

The scientific and technical peer-reviewed journal is intended for the publication of articles on the latest achievements in the field of physics with prospects for advancements (technical and scientific) applications.

The periodicity is 6 issues per year.

Founder and publisher:

Research, Development and Production Center ORION, Joint-Stock Company –
Russian Federation State Science Center
(RD&P Center ORION, JSC)
9, Kosinskaya st., Moscow, 111538 Russia

The journal is included into the List of peer-reviewed science press of the State Commission for Academic Degrees and Titles of Russian Federation. The Journal is included in Scientific Electronic Library eLIBRARY.RU, SCOPUS, Chemical Abstracts (CA), Russian Science Citation Index (RSCI), Directory of Open Access Journals (DOAJ), Directory of Open Access Scholarly Resources (ROAD), Google Scholar.

Editor-in-Chief:

Igor Burlakov,

Dr. Sci. (Eng.), Professor,
Research, Development and Production Center ORION, Joint-Stock Company –
Russian Federation State Science Center

Editorial office address:

9, Kosinskaya st., Moscow, 111538, Russia, RD&P Center ORION, JSC.
Phone: 8(499) 374-82-40
E-mail: advance@orion-ir.ru
Internet: applphys.orion-ir.ru

The registration PI No. FS 77-73641
was issued in September 21, 2018
by the Federal Service for Supervision
of Communications, Information Technology, and Mass Media of Russia

Editorial Board

Stepan Andreev Dr. Sci. (Phys.-Math.), Prokhorov General Physics Institute of the

Russian Academy of Sciences, Moscow, Russia

Konstantin Boltar Dr. Sci. (Phys.-Math.), Professor, RD&P Center ORION, Moscow,

Russia

Leonid Vasilyak Dr. Sci. (Phys.-Math.), Professor (Deputy Editor-in-Chief), Joint

Institute for High Temperatures of Russian Academy of Sciences,

Moscow, Russia

Namik Gusein-zade Dr. Sci. (Phys.-Math.), Professor, Prokhorov General Physics

Institute of the Russian Academy of Sciences, Moscow, Russia

Vyacheslav Ivanov PhD (Phys.-Math.), Associate Professor, Prokhorov General Physics

Institute of the Russian Academy of Sciences, Moscow, Russia

Victor Ivanov Dr. Sci. (Phys.-Math.), Professor, Corresponding Member of the

Russian Academy of Sciences, Moscow Institute of Physics and

Technology, Dolgoprudny, Moscow Region, Russian

Vitaly Konov Dr. Sci. (Phys.-Math.), Academician of the Russian Academy of

Sciences, Prokhorov General Physics Institute of the Russian

Academy of Sciences, Moscow, Russia

Evgeniy Klimanov Dr. Sci. (Eng.), Professor, RD&P Center ORION, Moscow, Russia

Yuri Lebedev Dr. Sci. (Phys.-Math.), A. V. Topchiev Institute of Petrochemical

Synthesis of the Russian Academy of Sciences, Moscow, Russia

Michael Lyamshev PhD (Phys.-Math.), Prokhorov General Physics Institute of the

Russian Academy of Sciences, Moscow, Russia

Sergey Maiorov Dr. Sci. (Phys.-Math.), Joint Institute for High Temperatures of

Russian Academy of Sciences, Moscow, Russia

Sergey Nikitov Dr. Sci. (Phys.-Math.), Professor, Academician of the Russian

Academy of Sciences, Kotelnikov Institute of RadioEngineering and

Electronics of Russian Academy of Sciences, Moscow, Russia

Vladimir Ponomarenko Dr. Sci. (Phys.-Math.), Professor, RD&P Center ORION, Moscow,

Russia

Sergey Popov Dr. Sci. (Eng.), Shvabe Holding, Moscow, Russia

Vyacheslav Kholodnov Dr. Sci. (Phys.-Math.), Professor, Kotelnikov Institute of

RadioEngineering and Electronics of Russian Academy of Sciences,

Moscow, Russia

Vladislav Khomich Dr. Sci. (Phys.-Math.), Academician of the Russian Academy of

Sciences, Branch of Federal State Budgetary Scientific Institution for Electrophysics and Electric Power of Russian Academy of Sciences,

Moscow, Russia

Natalia Iakovleva Dr. Sci. (Eng.), RD&P Center ORION, Moscow, Russia

Vladimir Yamshchikov Dr. Sci. (Eng.), Corresponding Member of the Russian Academy of

Sciences, Branch of Federal State Budgetary Scientific Institution for Electrophysics and Electric Power of Russian Academy of Sciences,

Moscow, Russia

APPLIED PHYSICS [in Russian]

THE SCIENTIFIC AND TECHNICAL JOURNAL

| 2025, № 2 | Founded in 1994 | Moscow |
|--|--|-------------------|
| | CONTENTS | |
| | GENERAL PHYSICS | |
| Experimental evaluation of <i>Denisov D. G.</i> | laser radiation quality in the differential scattering method | 5 |
| | PHOTOELECTRONICS | |
| colloidal quantum dots PbS Ponomarenko V. P., Popov V Deev G. Yu., Dragunov D. H Ilyinov D. V., Petrushina V Spirin M. G., Tovstun S. A. | y 640×512 with an extended sensitivity range of 0.4–2.0 μm based of CQDs with an electron-blocking p-NiO _x layer V. S., Pankov M. A., Khamidullin K. A., Deomidov A. D., Fedorov A. A., E., Epifanov O. V., Zaripov S. I., Lazarev P. S., Mirofyanchenko E. V. A., Burlakov I. D., Polessky A. V., Startsev V. V., Brichkin S. A., Gapanovich M. V., Gak V. Yu., Gadomska A. V., Pevtsov D. I. S., Demkin D. V., Ivanova V. A., Ivanov V. V., Razumov V. F. | A., V., B., |
| • | rnthesis of environmentally friendly colloidal quantum dots CuInS ₂ halagin A. Yu., Lim V. V., Milenkovich T., Vershinina O. V., Yakovlev V. C | O., 21 |
| _ | of mixed plasmon-phonon modes p -InSb and p -GaSb at $T = 295$ K V ., Zhuravlev E. O., Kozlov R. Yu., Komarovskiy N. Yu., Kusnetsov A. I | N., |
| | yer during diffusion processes in silicon N., Irodov N. A., Klimanov E. A., Lyalikov A. V., Malygin V. A E. A. | A., 39 |
| | s of CdTe/GaAs(100) epitaxial films grown in different temperatu | ıre |
| conditions Grekova A. A., Klimov E. A., | Vinichenko A. N., Burlakov I. D. | 46 |
| | PLASMA PHYSICS AND PLASMA METHODS | |
| | e of plasma processes in the vacuum diode of Kalmar high-curre development of shock-wave processes in targets | ent |
| | , Smirnova A. R., Strizhakov M. G., Sunchugashev K. A., Yusupova L. M | M., 55 |
| Visualization of the electric Panov V. A., Saveliev A. S., K | field in transformer oil using suspended water microdroplets <i>Yulikov Yu. M.</i> | 62 |

| INFORMATION Rules for authors | 103 |
|--|-----|
| Synthesis of TiN coatings in Cu vapor on T15K6 alloy using the hybrid plasma technology Semenov A. P., Tsyrenov D. BD., Ulakhanov N. S., Semenova I. A. | 97 |
| Frolov N. Yu., Klokov A. Yu., Sharkov A. I., Nikolaev S. N., Chernopitsky M. A., Chentsov S. I., Pugachev M. V., Shupletsov A. V., Krivobok V. S., Kuntsevich A. Yu. | 90 |
| Study of acoustic properties of van der Waals heterostructures containing the WSe ₂ monolayer using the hypersonic microscopy | |
| Optical properties of calcium tungstate doped with various lanthanides (Pr, Nd, Eu, Ce, Sm) Kuznetsova P. D., Mukhanova E. A., Volik K. K., Pankin I. A., Soldatov A. V. | 84 |
| PHYSICAL SCIENCE OF MATERIALS | |
| High-current photoemission glow discharge in Xe-Cs mixture Martsinovsky A. M., Gavrish S. V., Korenyugin D. G., Guslin A. S., Kuzin V. N. | 76 |
| in the alternating current plasma torch Dudnik Yu. D., Safronov A. A., Shiryaev V. N., Vasilyev M. I., Vasilieva O. B. | 69 |
| Study of the dynamics of arc discharge burning in the methane-nydrogen-containing atmosphere | |

= GENERAL PHYSICS =

UDC 535.42, 535.51 PACS: 03.65.Nk EDN: XDPAWH

Experimental evaluation of laser radiation quality in the differential scattering method

© D. G. Denisov

Bauman Moscow State Technical University, Moscow, 105005 Russia E-mail: denisov_dg@mail.ru

Received 02.12.2024; revised 26.12.2024; accepted 07.04.2025 Scientific specialty code: 2.2.6

The influence of the lens and mirror optical circuits of the channel illuminating a prototype of an optical-electronic system for measuring the parameters of angstrom-level roughness of optical surfaces on the quality of laser radiation was researched and experimentally analyzed. Based on the prototype developed using lens and mirror optical circuits, a quantitative assessment was given of such laser radiation quality indicators as the M^2 parameter and the contrast function of the speckle structure in the cross-section of its energy profile. Based on the findings of the described comparative analysis of the influence of two optical circuits of the prototype illumination channel on the target indicators of the laser radiation quality, recommendations were made whether it is advisable to use a lens optical system in the illumination channel in terms of the minimum measurement error.

Keywords: lens and mirror optical systems; M² parameter; speckle structure contrast; laser beam energy profile; laser radiation; differential scattering method.

DOI: 10.51368/1996-0948-2025-2-5-11

Introduction

The scientific papers previously published [1–4] describe the main scientific principles of the differential scattering method for quality control of optical surfaces. Papers [1, 2] have demonstrated the influence of limiting differential factors in the scattering method on the monitoring of angstrom-level optical surfaces. It is also worth noting the necessity of producing the high-quality laser radiation [5], primarily in the plane of the controlled optical surface, fluctuations since additional intensity occurring in the energy profile of the laser beam can lead to the formation of the speckle pattern in the recorded scattering indicatrix [1–8]. Thus, in development of a method for monitoring the roughness of angstrom-level optical surfaces, aspects related to the quality of the laser radiation illuminated spot formed in the plane of a part under control (lateral region) are of importance and relevance.

Main part

The following quantitative indicators were analyzed as the output characteristics of the laser radiation formed by lens and mirror optical systems in the plane of the optical surface under study [1, 5] (see Table 1).

Table 1

List of the main analyzed characteristics of the laser radiation formed by the illumination channel based on the lens and mirror optical systems of the developed prototype

| No. | Parameter | Best values of the characteristics |
|-----|--|------------------------------------|
| 1 | Contrast function of speckle structure in the cross-section of the laser beam energy profile – $C_{\rm S}$, p. u. | |
| | $C_S = \frac{\sigma_I}{I}$, $\sigma_I - RMS$ value of intensity fluctuations in the video image | < 0.5 |
| | showing the distribution of the laser beam energy profile, I – average value of intensity in the video image showing the distribution of the laser beam energy profile | |
| 2 | Laser beam quality parameter, p. u. | _ |
| | $M^2 = rac{\pi \cdot 	heta_{ m real} \cdot { m D}_{ m real}}{4 \cdot \lambda} = rac{\pi \cdot { m D}_{ m real}^2}{4 \cdot \lambda \cdot { m z}_{ m c}}$ | $1 \le M^2 \le 1,2$ |
| | θ_{real} – divergence of a real laser beam; D_{real} – diameter in the cross-section of | |
| | the real laser beam waist; z_c – laser beam confocality parameter (near-zone | |
| | length); λ– laser radiation wavelength | |

To evaluate the characteristics of the optical radiation formed by the illumination channel in the differential scattering method (see Table 1), a prototype was developed with an option of modifying the illumination channel when installing both lens and mirror optical systems that were preliminarily

calculated in the Zemax automated design system.

The functional diagrams developed for two versions of the prototype illumination channel based on lens and mirror optical systems are shown in Figures 1 and 2, respectively.

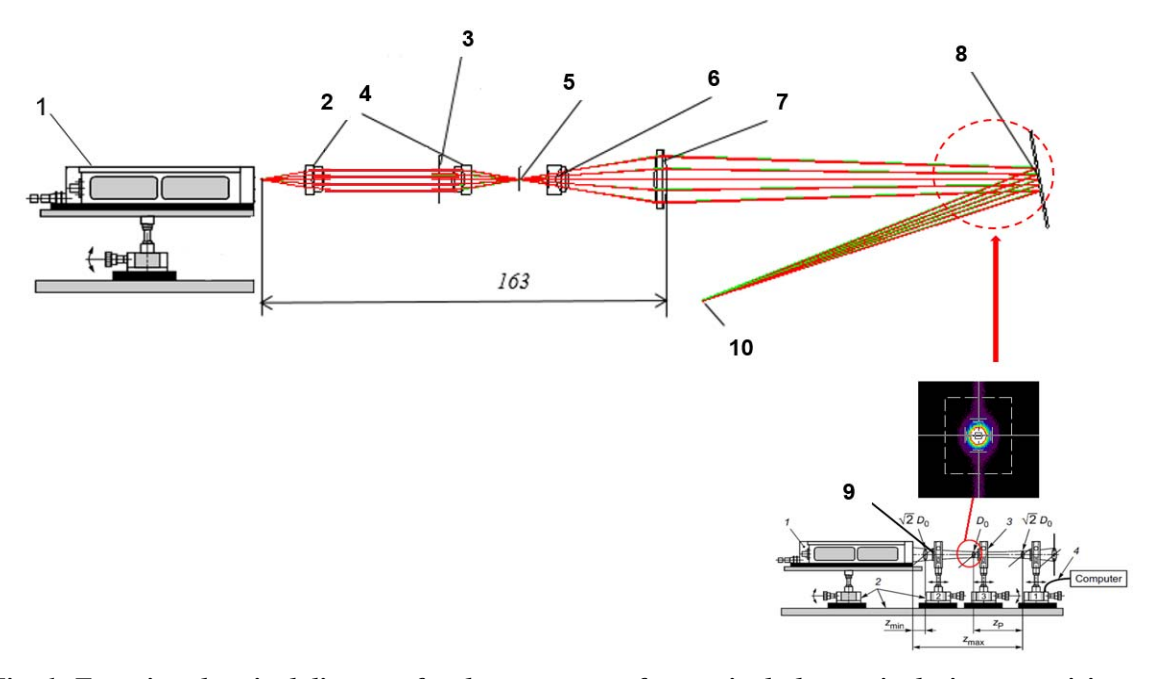


Fig. 1. Functional optical diagram for the prototype of an optical-electronic device comprising an illumination channel based on a lens optical system: 1 – laser radiation source; 2, 4, 6, 7 – lens optical system objectives; 3 – diaphragm; 4 – microdiaphragm; 8 – surface of an optical part under control; 9 – M^2 sensor using the confocality measuring method; 10 – plane of analyzing the scattered laser radiation (plane of the photoreceiver – photomultiplier)

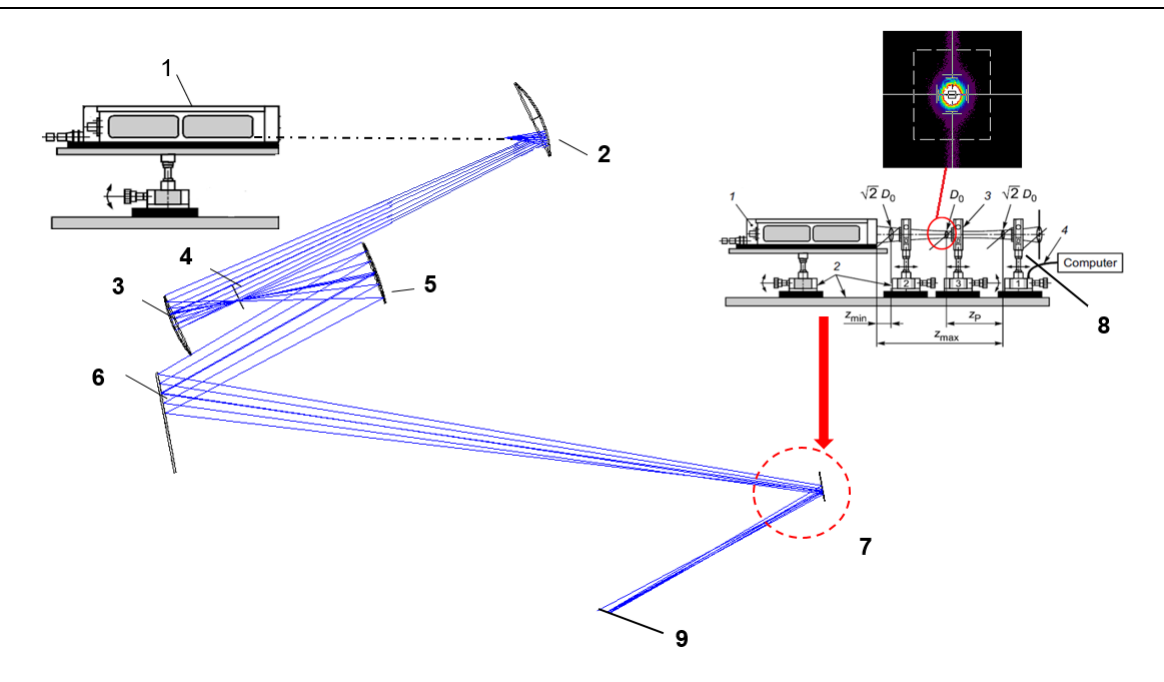


Fig. 2. Functional optical diagram for the prototype of an optical-electronic device comprising an illumination channel based on a mirror optical system: 1 – laser radiation source; 2 (R_3 = 40 mm; D_3 = 32 mm) – spherical mirror; 3 (R_3 = 50 mm; D_3 = 25.4 mm) – spherical mirror, 4 – microdiaphragm, 5 (R_3 = 100; D_3 = 25.4) – spherical mirror, 6 (R_3 = ∞ ; D_3 = 25.4) – flat mirror; 7 – surface of an optical part under control; 8 – M^2 -sensor using the confocality measuring method; 19 – plane of analyzing the scattered laser radiation (plane of the photoreceiver – photomultiplier)

In the course of the prototype development, according to the functional optical schemes shown in Figures 1 and 2, five lasers were analyzed as laser radiation sources. These included gas lasers based on the He-Ne active medium having the following main generation lines: 6328 nm, 6120 nm, 543.5 nm, 632 nm, as well as a solid-state laser based on YAG-Nd at the generation wavelength of 473 nm.

Upon a comparative analysis of the steady state of quantitative energy indicators and characteristics, a laser with a generation wavelength of 473 nm was chosen as a radiation source for the comparative analysis of optical circuits, since it provides the maximum stability, on the one hand, and generates at the shortest wavelength, on the other hand, which is important for evaluation of intensity fluctuations in the energy profile.

At first the initial quality of the laser beam of a solid-state laser source based on the active medium and matrix – YAG:Nd – was measured according to the method presented in the author's paper published previously using the M² sensor [5].

According to the European standard ISO 11146-1-2005, such evaluation parameters as the propagation factor K and M² factor, have been introduced to evaluate the quality of radiation generated by a resonator. The latter describes the difference between the real laser beam's structure and the ideal mode structure TEM_{00} [5] and is defined as the ratio of angular divergence of a real laser beam and the angular divergence of ideal (or diffraction) laser According to the method described [5], the quality of the original laser beam prior to the optical system was measured. For this purpose, the minimum cross-section of the laser source beam was measured using the M² sensor. As the experiment showed, this crosssection for a given laser is located on the output partially transparent mirror, which is indicative of a plane-spherical, i.e. stable, resonator. After that the M² sensor was moved relative to the recorded minimum

cross-section of the laser beam through the distance, at which this cross-section increased by $\sqrt{2}$, which corresponds to the mirror position of the equivalent confocal resonator [5]. The measured distance was recorded and assumed as the laser beam confocality parameter or the value describing its near zone or the Rayleigh parameter (see Fig. 3).

Analysis of the original laser beam and beams passed through the lens and mirror optical systems registered distributions of the laser beam's energy profile, including typical intensity fluctuations determined by statistical values (see Table 1):

 σ_I – RMS value of intensity fluctuations in the video image showing the distribution of the laser beam's energy profile, W;

I – average value of intensity in the video image showing the distribution of the laser beam's energy profile, W;

 $C_s = \frac{\sigma_I}{I}$ – contrast function of speckle structure in the cross-section of the laser beam energy profile – C_s , p. u.

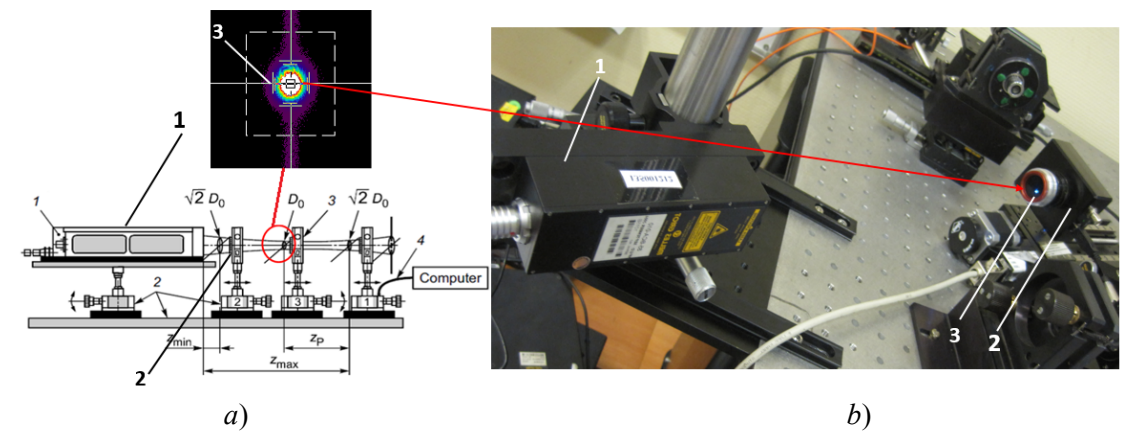


Fig. 3. Concerning the method of measuring the initial intensity distribution in the energy profile of the Gaussian laser beam: 1 – solid-state laser source at the wavelength of 473 nm; 2 – M^2 sensor; 3 – registered intensity distribution in the laser beam energy profile. a) – sequence of iterative measurements of the quality parameter of the Gaussian laser beam; b) – photo of the overall view of the stand for measuring initial parameters of the Gaussian laser beam

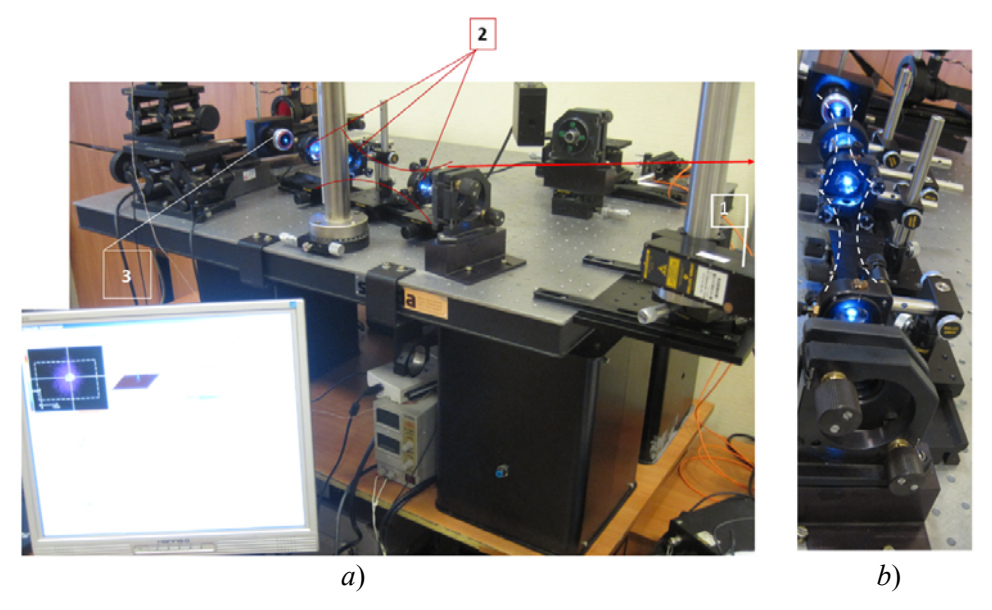


Fig. 4. Photo of the overall view of the stand for measuring the quality parameter and statistical values describing fluctuations of the intensity of laser radiation passed through the lens optical system: 1 – laser radiation source; 2 – objectives of the lens optical system; 3 – M^2 sensor using the confocality measuring method; a) – photo of the entire measuring stand; a0) – photo of the lens optical system and conditional transformation of the laser beam through its optical elements prior to the a1 sensor

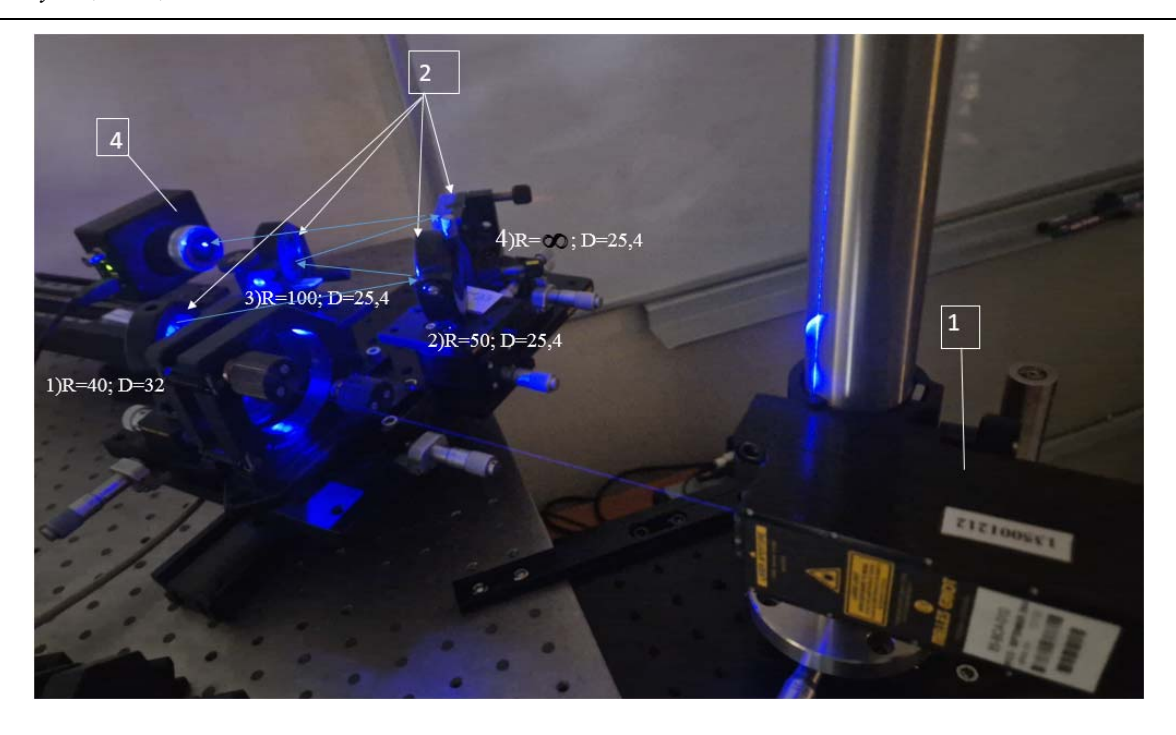


Fig. 5. Photo of the overall view of the stand for measuring the quality parameter and statistical values describing fluctuations of the intensity of laser radiation passed through the mirror optical system: 1- laser radiation source; 2- optical system mirrors; $3-M^2$ sensor using the confocality parameter measuring method

Based on the developed functional optical systems for the prototype comprising an illumination channel based on lens (see Fig. 1) and mirror (see Fig. 2) optical circuits, corresponding measuring stands were developed (see Fig. 4, 5).

Figure 4 shows the overall view of the stand for measuring the quality parameter and statistical values describing fluctuations of the intensity of laser radiation passed through the lens optical system.

Figure 5 shows the overall view of the stand for measuring the quality parameter and statistical values describing fluctuations of the intensity of laser radiation passed through the mirror optical system.

Conclusion

During the experimental studies of passing the optical path of the lens and mirror optical systems shown in Figures 4 and 5, the intensity distribution in the laser beam's energy profile was measured and its quality was evaluated, according to the parameters

given in Table 1. Results of the experimental studies are presented in Figure 6 and Table 2.

Based on the obtained experimental data, a comparative analysis of the characteristics of laser radiation that passed through lens and mirror optical systems is presented (see Table 2).

the completed experimental Thus, comparative analysis of the characteristics of laser radiation generated by optical systems (see Table 2) shows that the lens optical system is more preferable because the contrast level of the speckle structure (speckle pattern) in the cross-section of the laser beam's energy profile is minimum. This argument is important when laser radiation interacts with a scattering optical surface having the angstrom-level roughness, which forms low-intensity scattered informative laser radiation. The second key criterion determining the feasibility of using a lens optical system is the laser beam quality parameter, which ensures the required dimensions of the lateral region (illuminated region) of the optical part under control and the specified energy in the illuminated spot.

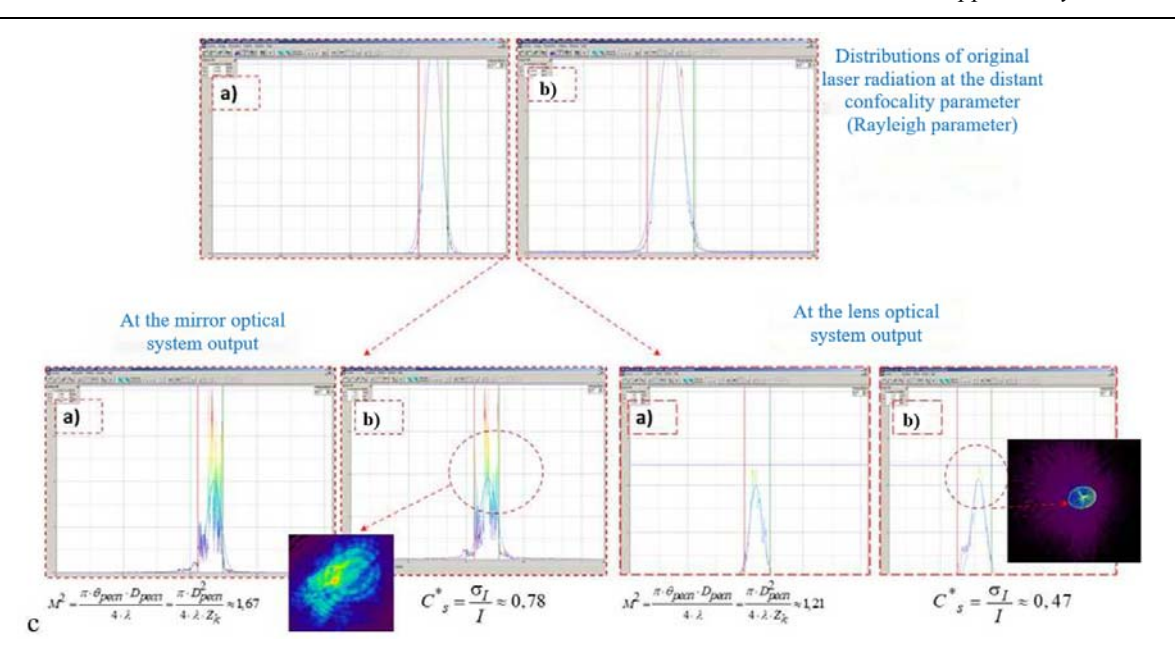


Fig. 6. Concerning the definition and research of the laser beam quality parameter and speckle structure contrast formed in the plane of the optical part under control for mirror and lens optical systems:

a) – cross-section of the Gaussian beam profile along axis x; b) – cross-section of the Gaussian beam profile along axis y

Table 2
Comparison of the main characteristics of laser radiation that has passed through lens
and mirror optical systems

| No. | Parameter | Characteristic values (ideal case) | Characteristic values after passing the lens optical system | Characteristic values after passing the mirror optical system |
|-----|---|------------------------------------|---|---|
| 1* | Contrast function of speckle structure in the cross-section of the laser beam energy profile $-C_s$, p. u. $C_s = \frac{\sigma_I}{I}, \sigma_I - RMS value of$ | | | |
| | intensity fluctuations in the video image showing the distribution of the laser beam energy profile, I – average value of intensity in the video image showing the distribution of the laser beam energy profile | < 0.5 | 0.47 | 0.78 |
| 2 | Laser beam quality parameter, p. u. $M^2 = \frac{\pi \cdot \theta_{real} \cdot D_{real}}{4 \cdot \lambda} = \frac{\pi \cdot D_{real}^2}{4 \cdot \lambda \cdot z_c}$ $\theta_{real} - \text{divergence of a real laser}$ beam; $D_{real} - \text{diameter in the cross-section of the real laser beam waist;}$ $z_c - \text{laser beam confocality}$ parameter (near-zone length); $\lambda - \text{laser radiation wavelength}$ | $1 \le M^2 \le 1,2$ | 1.21 | 1.67 |

^{* –} abnormal emissions resulting from instability of laser radiation intensity fluctuations were filtered off during calculation.

REFERENCES

- 1. Denisov D. G., Applied Physics, No. 1, 89–96 (2022) [in Russian].
- 2. Denisov D. G. and Karasik V. E., Bulletin of the Bauman Moscow State Technical University. Instrument Engineering series, No. 2 (83), 36–47 (2011).
- 3. Rytov S. M. Introduction to statistical radiophysics. Part II. Random Fields. Moscow, Nauka Publ., 1966.
- 4. Beckman P. and Spitzikino A. Scattering of electromagnetic waves on a rough surface. Norwood, Pergamon Press, ARTEK HOUSE, 1987.
- 5. Denisov D. G. and Karasik V. E., Measurement methods **52** (3), 260–265 (2009).
- 6. Goodman J. W. Speckle phenomena in optics: theory and applications. Colorado, Roberts and Company, 2006.
- 7. Franson M. Literature review. Moscow, MIR, 1980.
- 8. Goodman J. Statistical characteristics. Moscow, Mir Publ., 1988.

About the author

Dmitry Gennadievich Denisov, Associate Professor, Candidate of Technical Sciences, Bauman Moscow State Technical University (105005, Russia, Moscow, 2-nd Baumanskaya Ulitsa, 5). E-mail: denisov_dg@mail.ru SPIN code 8152-8378, Author ID 798946

PHOTOELECTRONICS :

UDC 621. PACS: 85, 85.60.–q

EDN: GETOGH

Uncooled photosensor array 640×512 with an extended sensitivity range of 0.4–2.0 µm based on colloidal quantum dots PbS CQDs with an electron-blocking p-NiO $_x$ layer

© V. P. Ponomarenko^{1,2}, V. S. Popov^{1,2,*}, M. A. Pankov¹, K. A. Khamidullin¹, A. D. Deomidov¹, A. A. Fedorov¹, G. Yu. Deev¹, D. E. Dragunov¹, O. V. Epifanov¹, P. I. Zaripov¹, P. S. Lazarev¹, E. V. Mirofyanchenko¹, D. V. Ilyinov¹, V. A. Petrushina¹, I. D. Burlakov¹, A. V. Polessky¹, V. V. Startsev¹, S. B. Brichkin^{2,3}, M. G. Spirin^{2,3}, S. A. Tovstun^{2,3}, M. V. Gapanovich^{2,3}, V. Yu. Gak^{2,3}, A. V. Gadomskaya^{2,3}, D. N. Pevtsov², A. V. Katsaba², A. S. Kirichenko², D. V. Dyomkin², V. A. Ivanova², V. V. Ivanov², V. F. Razumov^{2,3}

¹RD&P Center ORION, JSC, Moscow, 111538 Russia

*E-mail: popov.vs@mipt.ru

² Moscow Institute of Physics and Technology (National Research University),

Moscow Region, Dolgoprudny, 141701 Russia

³ Federal Research Center for Problems of Chemical Physics and Medicinal Chemistry
of the Russian Academy of Sciences Moscow Region, Chernogolovka, 142432 Russia

Received 03.03.2025; revised 25.03.2025; accepted 07.04.2025 Scientific specialty code: 1.3.11

Night vision devices with an extended sensitivity range of 0.4 μ m to 2.0 μ m are essential for scientific, civil and special-purpose applications. The architecture and basic specifications of the array photosensor of the 640×512 format (15 μ m pitch) with the extended sensitivity range (0.4-2.0 μ m) developed on the basis of PbS CQP colloidal quantum dots are described. The major part of the photocurrent is generated in CQD layer n-PbS-TBAI. The layer has been made by substituting the initial ligand (oleic acid) with iodine during treatment of the CQD layer with tetra-n-butylammonium iodide (TBAI). The electron-blocking layer (hole transport layer) has been created on the basis of p-NiO_x. The hole-blocking layer (electron transport layer) has been created on the basis of n-ZnO.

Keywords: colloidal quantum dot (CQD); ligand; transport layer; photosensor.

DOI: 10.51368/1996-0948-2025-2-12-20

1. Introduction

The recent period has been marked by the rapid growth in the research aimed at creating array photosensors (FPA) using materials and structures of limited dimensions [1–3]. A new trend in the field of photosensors can be clearly seen in the last two decades. This trend is associated with the use of so-called quasi-zero-dimensional colloidal quantum dots (CQDs), the spectral properties of which are determined by the average size of semiconductor nanoparticles that vary within the range of 2–10 nm. The development of this direction led to the creation in 2020 of the first serial-producted

matrices and cameras that are based on CQDs and operate in the spectral range from 0.4 to $2.1 \mu m$ [3].

The use of colloidal quantum dots allows to significantly simplify the technology, relieve the limitations imposed on the pitch of photosensitive elements [4] and significantly decrease the FPA cost [5].

The technology of manufacturing array photosensors using CQDs, which was named the monolithic-hybrid technology [4, 6], is based on application of liquid suspensions photosensitive containing nanoparticles directly on the surface of a silicon ROIC reading and pre-processing photo signals without the use of microcontacts made of indium or other materials. Such photosensors frontal illumination. which distinguishes them from sensors based on epitaxial 3D materials. such In_{0.53}Ga_{0.47}As/InP. In the latter photosensors, before being absorbed by the photosensitive layer $(In_{0.53}Ga_{0.47}As)$ the radiation from objects in the viewed scene has to pass through a wide-band gap single-crystal substrate (InP) of the epitaxial layer, which is opaque to the visible region (0.4–0.76 µm), thus limiting the colour sensitivity of the photosensor to the wavelength range of 0.9-1.6 µm. Due to the possibility of using the frontal illumination of the photosensitive layer without the need for process operations aimed at thinning the substrates [7, 8], which

greatly complicate the technology of manufacturing devices, the wide spectrality of QCD-based FPAs is ensured. For example, the use of PbS CQDs with colloidal quantum dots sized about 10 nm for making a photosensitive array layer enables registering the electromagnetic radiation within a wide spectral range of 0.4 to 2.1 µm [3].

The paper [9] describes the uncooled array photosensor 640×512 (15 µm pitch) developed by us for the spectral range of 0.4–2.0 µm and based on colloidal quantum dots PbS CQDs, where the electron-blocking hole transport layer was made of *p*-PbS-EDT CQDs (Fig. 1*a*).

This paper describes a new array photosensors (FPA) developed by us for the spectral range of 0.4–2.0 µm that features the 640×512 format and a pitch of photosensitive elements of 15 µm and is made of colloidal quantum dots PbS CQDs on the surface of the silicon ROIC reading *p*-channel photosignals. Unlike paper [9], here the electron-blocking layer (hole transport layer) is made of not liquid CQD suspension p-PbS-EDT, but of pproduced by magnetron NiO_r material sputtering. This material has recently started to be used for production of solar cells as a hole transport layer and has proven itself well due to its higher mobility and stability of properties as compared to organic materials [10, 11]. Other layers were made similarly to those in paper [9].

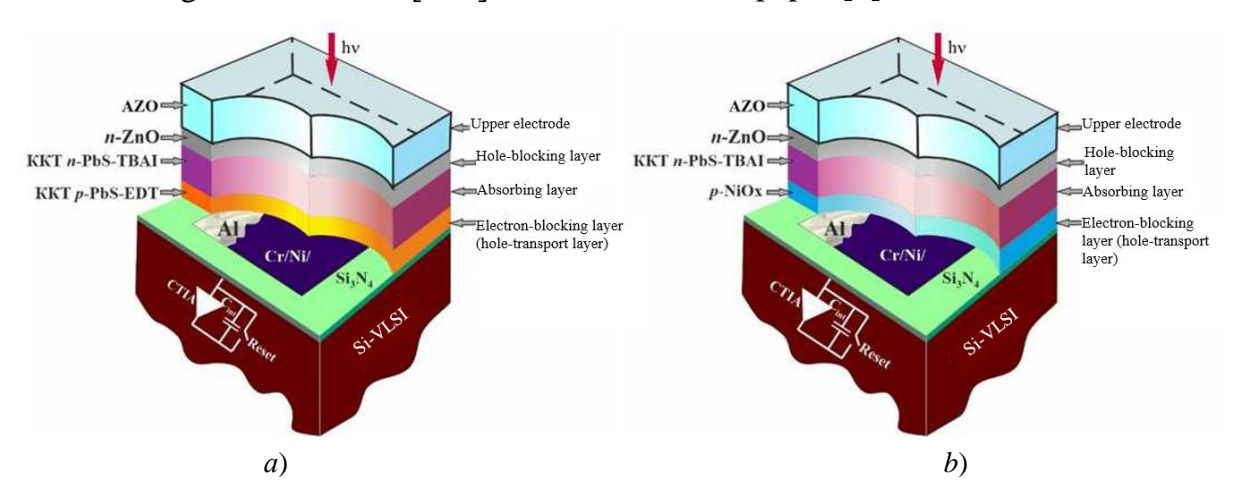


Fig. 1. Architectures of FPA 640×512 (15 µm pitch) based on PbS CQDs: a) – FPA sensing element with the electron-blocking layer (hole transport layer) made of CQDs p-PbS-EDT [9]; b) – FPA sensing element with the electron-blocking layer (hole transport layer) made of p-NiO_x material

2. Architecture of array photosensor 640×512 with the electron-blocking and hole-transport layer based on *p*-NiO_x

The architecture of each photosensitive element developed by the authors of the new 640×512 array photosensor has the form $Cr/Ni/p-NiO_x$ CQD/n-PbS-TBAI/n-ZnO/AZO (Fig. 1b). The major part of photocarriers is generated by radiation in CQD layer n-PbS-TBAI. After photoexcitons decay, resulting electrons and holes are separated with the energy barrier of the p-n junction type at the contact of the n-PbS-TBAI CQD and p-NiO $_x$ CQD layers. The PbS CQD layer of the electron conductivity type is manufactured by substituting the initial ligand (oleic acid) after

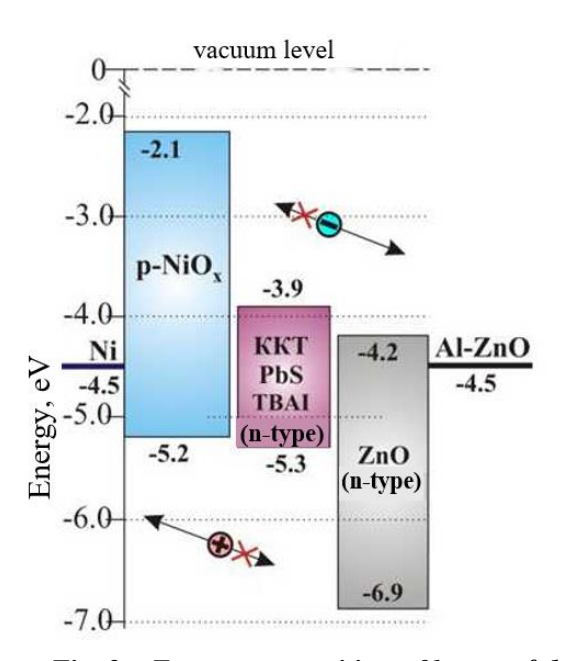


Fig. 2a. Energy composition of layers of the Cr/Ni/p-NiO_x/CQD n-PbS-TBAI/n-ZnO/AZO structure, on which basis array photosensor 640×512 made of PbS CQDs with the electron-blocking and hole-transport layer based on p-NiO_x was developed

3. Properties of array photosensor 640×512 with the electron-blocking and hole-transport layer based on p-NiO $_x$

A photograph of the finished array photosensitive element of the 640×512 format based on colloidal quantum dots PbS CQDs

treatment with *tetra-n-butylammonium iodide*. *Lead chloride* and *N*, *N'-diphenylthiourea* are used as precursors of lead and sulfur in the synthesis of PbS CQD. The coating of zinc oxide doped with aluminum to form a solid solution in the ZnO-Al₂O₃ (AZO) system is used as a coating transparent for the electrode radiation [12].

The energy composition of the structure's individual layers that specifies the directions of electron and hole transport in the layers of the photosensor with the Cr/Ni/p-NiO_x/KKT n-PbS-TBAI/n-ZnO/AZO architecture is shown in Fig. 2a along with a similar energy composition of the layers of the Cr/Ni/KKT p-PbS-EDT/KKT n-PbS-TBAI/n-ZnO/AZO structure, which is shown in Fig. 2b.

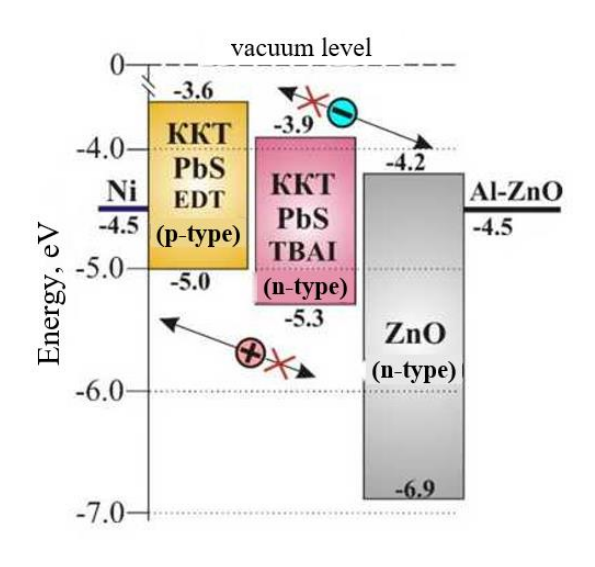


Fig. 2b. Energy composition of layers of the Cr/Ni/KKT p-PbS-EDT/KKT n-PbS-TBAI/n-ZnO/AZO structure, on which basis array photosensor 640×512 made of PbS CQDs with the electron-blocking and hole-transport layer based on PbS CQDs (p-EDT) [9] was developed

with the silicon ROIC reading and preprocessing photo signals and an upper electrode made of Al:ZnO (AZO) mounted on the raster for research is shown in 3a.

The study of the spectral dependence of the optical absorption of the suspension of lead sulfide's colloidal quantum dots in the *n-octane* solution, that were synthesized by the above-described method using PbCl₂ as a lead precursor, showed the first exciton peak occurs with a maximum located at the wavelength $\lambda_{max} \approx 1.8 \,\mu\text{m}$. Its full width at half maximum (FWHM) was 220 nm, which indicates a sufficiently high monodispersity of PbS nanocrystals [13] in the absorbing layer of PbS CQDs (n-TBAI) of the finished photosensor. Figure 3 shows array spectral dependence of the photosensitivity $S_i(\lambda)/S_i(\lambda_{max})$ reduced to unit for the array photosensor 640×512 with the silicon ROIC reading and pre-processing photo signals. The long-wave limit of photosensitivity is $\lambda_{lim} =$ = $1.96 \mu m$, the width of the sensitivity band falls within the wavelength range of $\Delta \lambda =$ = $0.4 \div 2.0 \,\mu m$. The use of the empirical

relationship $E_0 = 0.41 + (0.025d^2 + 0.283d)^{-1}$ that was derived in paper [13] and establishes the connection between the energy of optical transitions E_0 in the optical absorption spectra of the CQD solution and diameter d of the nanoparticles showed that the diameter of the colloidal quantum dots we used is $d \approx 9.5$ – 10 nm. The study of the nanoparticle shape by the high-resolution transmission electron microscopy showed that the prevailing CQD shape is a truncated octahedron (Fig. 4a). Each colloidal quantum dot has eight faces (111) and six faces (100), which is confirmed by the findings of the study conducted in [14]. The structure of faces (100) and (111) is shown in Fig. 4b. The photograph of CQDs obtained by the transmission microscopy method is shown in Fig. 4c.

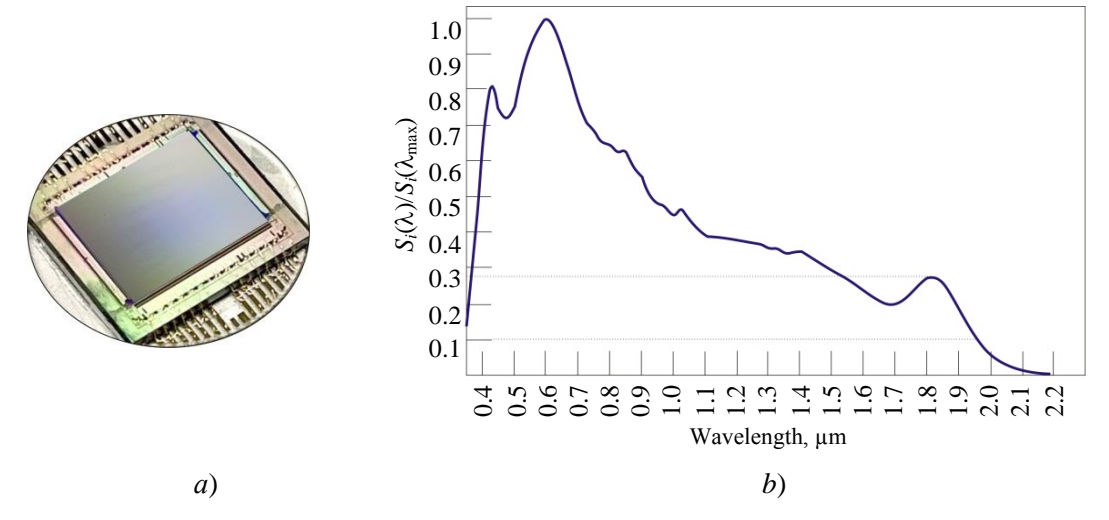


Fig. 3. Array photosensitive element (PSE) of the 640 \times 512 format based on colloidal quantum dots PbS CQDs with Cr/Ni/p-NiO $_x$ /KKT n-PbS-TBAI/n-ZnO/AZO architecture with silicon ROIC reading and pre-processing photo signals: a) – photo of raster-mounted PSE; b) – spectral dependence of photosensitivity reduced to unit at a room temperature

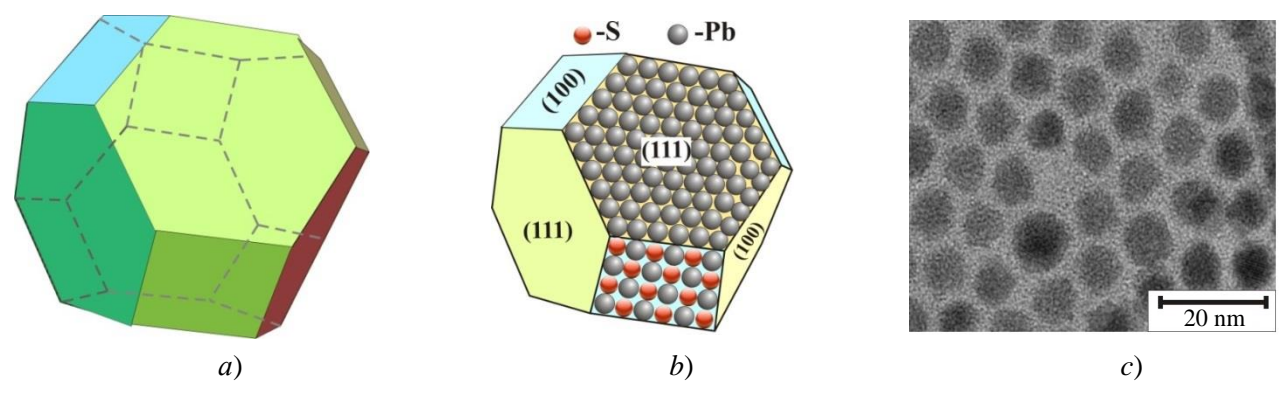


Fig. 4. a) – model of the CQD shape (truncated octahedron); b) – composition of CQD nanocrystal faces (100) and (111); c) – photo of the CQDs obtained by the TEM method

The current-voltage characteristic of one of the photosensitive elements, which was measured at the room temperature conditions of no illumination and under illumination from a monochromatic source with the wavelength of $\lambda = 0.94 \,\mu m$ and a power $P = 0.072 \text{ W} \cdot \text{cm}^{-2}$, is shown in Figure 5. The current-voltage characteristics (CVC) have a form typical for structures with an energy barrier of the p-n junction type. The monochromatic ampere-watt responsivity at zero bias is $S_0 = 0.35$ A/W and increases to $S_{-1} = 7.4$ A/W at back bias equaling to $V_{\text{bias}} =$ = -1.0 V. The average value of S_0 obtained by averaging the ampere-watt responsivity for 7 photosensitive elements is 0.27 A/W.

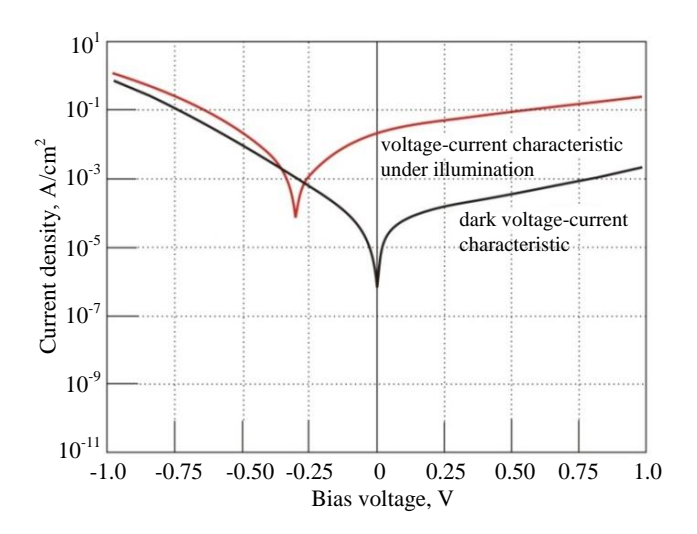


Fig. 5. Current-voltage characteristic of the photosensitive element under conditions of illumination from a monochromatic source ($\lambda = 0.94 \ \mu m$, $P = 0.072 \ W \ cm^{-2}$) and in conditions of no illumination

The spectral dependence of the specific detectivity of the uncooled single-element photosensor with the $Cr/Ni/p-NiO_x/KKT$ n-PbS-TBAI/n-ZnO/AZO architecture, which was measured under illumination from a black body with temperature $T_{BB} = 1273$ K at bias voltage V_{bias} equaling to 3.0 V is shown in Figure 6.

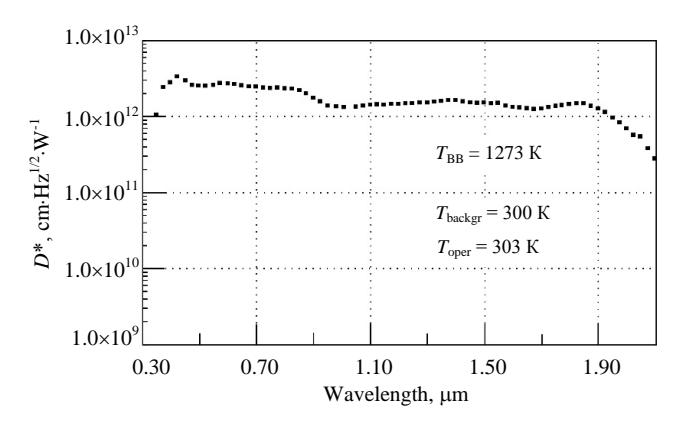
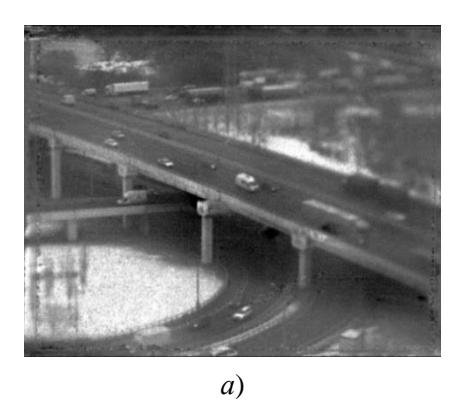


Fig. 6. Spectral dependence of the specific detectivity of the uncooled single-element photosensor with the $Cr/Ni/p-NiO_x/KKT$ n-PbS-TBAI/n-ZnO/AZO architecture, which was measured under illumination from a black body with temperature $T_{BB} = 1273 \ K \ (V_{bias} = 3.0 \ V)$

Figure 7 shows fragments of images of the transportation assembly, hands holding a soldering iron and a human face that were made in the daytime under illumination of the viewed scene of 300–500 lux using the array photosensor 640×512 (15 µm pitch). Single-point correction and signal calibration using a defocused image were used.



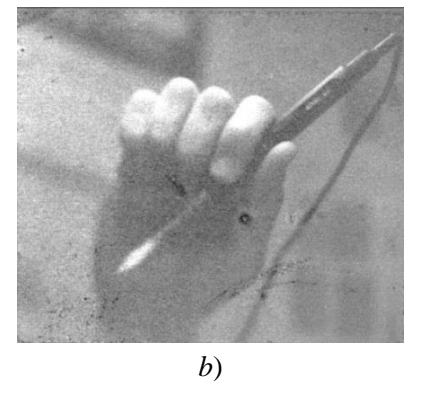




Fig. 7. Fragments of images made using the uncooled array photosensor 640×512 (15 µm pitch) based on colloidal quantum dots of PbS for the spectrum range of 0.4–2.0 µm; a) – transportation assembly (500 lux); b) – a hand holding a soldering iron (300 lux, $T_{soldering iron} = 300-350$ °C); image of a human face (300 lux); given in brackets is the illumination of the scene when the photos were taken

4. Conclusion

640×512 The array photosensor described herein and based colloidal on PbS dots of features quantum photosensitivity range of 0.4–2.0 µm, which is expanded as compared to the devices based on the $In_{0.53}Ga_{0.47}As$ solid solution. The analysis of using such expanded photosensitivity area in night vision devices, which is detailed in paper [15], has shown:

a) the average value of natural night illumination in the absence of the moon within the wavelength range $\lambda = 0.6$ –0.8 µm is $(1.5-3.0)\times10^{-5}$ W/n²·µm, while within the wavelength range of 1.4–1.8 µm it increases to $(6.0-7.0)\times10^{-4}$ W/m²·µm (Fig. 8);

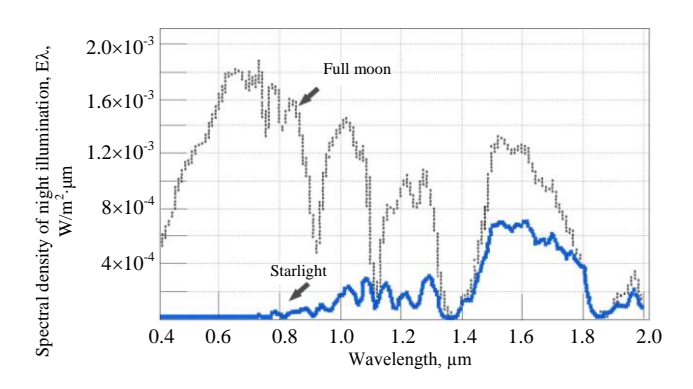


Fig. 8. Spectral density of night illumination under the full moon [16]

- b) the atmosphere transparency of the near IR region is noticeably higher than in the visible region. Thus, within the meteorological viewing range of $S_{\rm M}=10$ km, the transmittance of the 1 km thick atmospheric layer at the wavelength $\lambda=0.6$ μ m is 0.72, and in the center of the transparency window of 1.4–1.8 μ m it increases to 0.93;
- c) atmospheric haze brightness decreases by more than 10 times within the wavelength range of 1.4–1.8 µm as compared to the visible region;
- d) natural night illumination level within the spectrum range of $0.4-0.9 \,\mu m$ changes during the night from $10^{-1} \, W/m^2$ to $2.5 \times$

- $\times 10^{-5} \, \text{W/m}^2$ (i.e. almost by 4 orders of magnitude), and within the spectrum range of 1.4–1.8 μ m this change lies within the range of $1.6 \times 10^{-1} \, \text{W/m}^2$ to $(3-4) \times 10^{-3} \, \text{W/m}^2$;
- e) contrast value (observed object/background) in the wavelength range of 1.4–1.8 μ m is 1.4–1.5 times higher than within the range of 0.4–0.9 μ m.

This proves the potential of using the array photosensors described herein that feature the expanded sensitivity range of 0.4–2.0 µm for the creation of advanced domestic night vision devices.

This work was supported by the Advanced Research Foundation.

REFERENCES

- 1. Popov V. S. and Ponomarenko V. P. New photosensorics: 0D vs 2D. Moscow, MIPT, 2024.
- 2. Ponomarenko V. P., Popov V. S., Shuklov I. A., Ivanov V. V. and Razumov V. F., Russ. Chem. Rev. **93** (4), RCR5113 (2024). https://doi.org/10.59761/RCR5113.
- 3. Hinds S., Klem E., Gregory C., Hilton A., Hames G. and Violette K., Proc. of SPIE **11407** (2020). https://doi.org/ 10.1117/12.2559115.
- 4. Malinowski P. E., Georgitzikis E., Maes J., Vamvaka I., Frazzica F., Van Olmen J., De Moor P., Heremans P., Hens Z. and Cheyns D., Sensors **17**, 2867 (2017). https://doi.org/10.3390/s17122867.
- 5. Gréboval C., Darson D., Parahyba V., Alchaar R., Abadie C., Noguier V., Ferré S., Izquierdo E., Khalili A., Prado Y., Potet P. and Lhuillier E., Nanoscale **14** (26), 9359–9368 (2022). https://doi.org/10.1039/D2NR01313D
- 6. Popov V. S., Ponomarenko V. P. and Popov S. V., Journal of Communications Technology and Electronics **69** (4–6), 219–226 (2024). https://doi.org/ 10.51368/1996-0948-2023-6-45-53.
- 7. Burlakov I. D., Grinchenko L. Y., Dirochka A. I. and Zaletaev N. B., Usp. Prikl. Fiz. (Advances in Applied Physics) **2** (2), 131–136 (2014) [in Russian].
- 8. Martin T., Dixon P., Gagliardi M.-A. and Masaun N., Proc. of SPIE **5726**, 85–91 (2005). https://doi.org/ 10.1117/12.596409.
- 9. Ponomarenko V. P., Popov V. S., Pankov M. A., Khamidullin K. A., Deomidov A. D., Fedorov A. A., Deev G. Yu., Dragunov D. E.,

Epifanov O. V., Lazarev P. S., Mirofyanchenko E. V., Ilyinov D. V., Petrushina V. A., Burlakov I. D., Polessky A. V., Startsev V. V., Brichkin S. B., Spirin M. G., Tovstun S. A., Gapanovich M. V., Gak V. Yu., Gadomska A. V., Pevtsov D. N., Katsaba A. V., Kirichenko A. S., Demkin D. V., Ivanova V. A., Ivanov V. V. and Razumov V. F., Applied Physics, No. 1, 45–54 (2025). https://doi.org/ 10.51368/1996-0948-2025-1-45-54.

- 10. Yin X., Guo Y., Xie H., Que W. and Kong L. B., Sol. RRL, 1900001 (2018). https://doi.org/10.1002/solr.201900001.
- 11. Lian X., Chen J., Shan S., Wu G. and Chen H., ACS Appl. Mater. Interfaces **12** (41), 46340–46347 (2020). https://doi.org/10.1021/acsami.0c11731.
- 12. Ajili M., Jebbari N., Turki N. K. and Castagné M., International Renewable Energy

- Congress 2010 (IREC2010, November 5–7, Sousse, Tunisia), pp. 305–309.
- 13. Moreels I., Lambert K., Smeets D., De Muynck D., Nollet T., Martins J. C., Vanhaecke F., Vantomme A., Delerue C., Allan G. and Hens Z., ACS Nano **3** (10), 3023–3030 (2009). https://doi.org/10.1021/nn900863a.
- 14. Beygi H., Abdolkarim Sajjadi S., Babakhani A., Young J. F. and van Veggel F. C. J., Applied Surface Science **457**, 1–10 (2018). https://doi.org/10.1016/j.apsusc.2018.06.152.
- 15. Gusarova N. I., Koshchavtsev N. F. and Popov S. V., J. Commun. Technol. **61** (10), 1211–1214 (2016).
- 16. Voilmerhausen R. and Maurer T., Proc. of SPIE **5076**, 60–69 (2003). https://doi.org/10.1117/12.487189.

About authors

Vladimir Pavlovich Ponomarenko, Chief Designer, Head of Department, Doctor of Physics and Mathematics, Professor, RD&P Center ORION, JSC (111538, Russia, Moscow, Kosinskaya Ulitsa, 9), Moscow Institute of Physics and Technology (National Research University) (141701, Russia, Moscow Region, Dolgoprudny, Institutsky Per., 9). E-mail: 2392325@gmail.com SPIN code 6882-8721, Author ID 171358

Viktor Sergeevich Popov, Head of the Center, Head of the Laboratory, Associate Professor, Candidate of Chemical Sciences, RD&P Center ORION, JSC (111538, Russia, Moscow, Kosinskaya Ulitsa, 9), Moscow Institute of Physics and Technology (National Research University) (141701, Russia, Moscow Region, Dolgoprudny, Institutsky Per., 9). E-mail: popov.vs@mipt.ru SPIN code 5846-8066, Author ID 862015

Mikhail Aleksandrovich Pankov, Head of Laboratory, Candidate of Physics and Mathematics, RD&P Center ORION, JSC (111538, Russia, Moscow, Kosinskaya Ulitsa, 9). E-mail: mpa.off@gmail.com SPIN code 7160-9289, Author ID 145651

Kamil Alievich Khamidullin, Group Leader, Department Head, RD&P Center ORION, JSC (111538, Russia, Moscow, Kosinskaya Ulitsa, 9). E-mail: kamil1986@list.ru SPIN code 4091-3295, Author ID 710558

Alexander Dmitrievich Deomidov, Leading Engineer, RD&P Center ORION, JSC (111538, Russia, Moscow, Kosinskaya Ulitsa, 9). E-mail:aleks.deomidov@mail.ru SPIN code 7744-0080, Author ID 760104

Artem Alekseevich Fedorov, Engineer Cat. 2, RD&P Center ORION, JSC (111538, Russia, Moscow, Kosinskaya Ulitsa, 9).

German Yuryevich Deev, Engineer Cat. 2, RD&P Center ORION, JSC (111538, Russia, Moscow, Kosinskaya Ulitsa, 9). E-mail: deew.german@ya.ru SPIN code 9119-4550, Author ID 1281139

Denis Eduardovich Dragunov, Engineer Cat. 1, RD&P Center ORION, JSC (111538, Russia, Moscow, Kosinskaya Ulitsa, 9). E-mail: dragunov-de@gmail.com SPIN code 9757-8370, Author ID 1234132

Oleg Vladimirovich Epifanov, Leading Engineer, RD&P Center ORION, JSC (111538, Russia, Moscow, Kosinskaya Ulitsa, 9).

Shamil Ilnurovich Zaripov, Leading Engineer, RD&P Center ORION, JSC (111538, Russia, Moscow, Kosinskaya Ulitsa, 9).

Pavel Sergeevich Lazarev, Leading Engineer, RD&P Center ORION, JSC (111538, Russia, Moscow, Kosinskaya Ulitsa, 9).

Ekaterina Vasilievna Mirofyanchenko, Group Leader, Candidate of Technical Sciences, RD&P Center ORION, JSC (111538, Russia, Moscow, Kosinskaya Ulitsa, 9). E-mail: mirofianchenko@gmail.com SPIN code 1825-9300, Author ID 1157308

Denis Vladimirovich Ilyinov, Engineer Cat. 1, RD&P Center ORION, JSC (111538, Russia, Moscow, Kosinskaya Ulitsa, 9). E-mail: dv.iljinov@physics.msu.ru SPIN code 2401-2262, Author ID 1033906

Victoria Alekseevna Petrushina, Process Engineer, RD&P Center ORION, JSC (111538, Russia, Moscow, Kosinskaya Ulitsa, 9).

Igor Dmitrievich Burlakov, Deputy Director General for Innovations and Science, Doctor of Technical Sciences, Professor, RD&P Center ORION, JSC (111538, Russia, Moscow, Kosinskaya Ulitsa, 9). E-mail: idbur@orion-ir.ru SPIN code 6042-3634, Author ID 171368

Aleksey Viktorovich Poleskiy, Chief R&D Designer, Candidate of Technical Sciences, RD&P Center ORION, JSC (111538, Russia, Moscow, Kosinskaya Ulitsa, 9). E-mail: av22236@BK.ru SPIN code 3992-4520, Author ID 571156

Vadim Valerievich Startsev, General Director, Candidate of Technical Sciences, RD&P Center ORION, JSC (111538, Russia, Moscow, Kosinskaya Ulitsa, 9). E-mail: orion@orion-ir.ru SPIN code 4028-7138, Author ID 942991

Sergey Borisovich Brichkin, Department Head, Chief Researcher, Doctor of Chemical Sciences, Moscow Institute of Physics and Technology (National Research University) (141701, Russia, Moscow Region, Dolgoprudny, Institutsky Per., 9), Federal Research Center for Problems of Chemical Physics and Medicinal Chemistry of the Russian Academy of Sciences (142432, Russia, Moscow Region, Chernogolovka, Academician Semenov Prospekt, 1). E-mail: brichkin@icp.ac.ru SPIN code 1534-8054, Author ID 44021

Maxim Gennadievich Spirin, Senior Research Assistant, Leading Research Assistant, Doctor of Chemical Sciences, Moscow Institute of Physics and Technology (National Research University) (141701, Russia, Moscow Region, Dolgoprudny, Institutsky Per., 9), Federal Research Center for Problems of Chemical Physics and Medicinal Chemistry of the Russian Academy of Sciences (142432, Russia, Moscow Region, Chernogolovka, Academician Semenov Prospekt, 1). E-mail: max2004@icp.ac.ru SPIN code 9434-0999, Author ID 54508

Sergey Alexandrovich Tovstun, Senior Research Assistant, Candidate of Physics and Mathematics, Associate Professor, Moscow Institute of Physics and Technology (National Research University) (141701, Russia, Moscow Region, Dolgoprudny, Institutsky Per., 9), Federal Research Center for Problems of Chemical Physics and Medicinal Chemistry of the Russian Academy of Sciences (142432, Russia, Moscow Region, Chernogolovka, Academician Semenov Prospekt, 1). E-mail: tovstun@icp.ac.ru SPIN code 6114-3430, Author ID 874253

Mikhail Vyacheslavovich Gapanovich, Senior Research Assistant, Candidate of Chemical Sciences, Moscow Institute of Physics and Technology (National Research University) (141701, Russia, Moscow Region, Dolgoprudny, Institutsky Per., 9), Federal Research Center for Problems of Chemical Physics and Medicinal Chemistry of the Russian Academy of Sciences (142432, Russia, Moscow Region, Chernogolovka, Academician Semenov Prospekt, 1). E-mail: gmw1@mail.ru Author ID 156921

Vladimir Yurevich Gak, Research Assistant, Candidate of Chemical Sciences, Moscow Institute of Physics and Technology (National Research University) (141701, Russia, Moscow Region, Dolgoprudny, Institutsky 9), Federal Research Center for Problems of Chemical Physics and Medicinal Chemistry of the Russian Academy of Sciences (142432, Russia, Moscow Region, Chernogolovka, Academician Semenov Prospekt, 1). E-mail: gak@icp.ac.ru SPIN code 6311-9408, Author ID 56719

Anna Vladimirovna Gadomskaya, Senior Research Assistant, Candidate of Chemical Sciences, Moscow Institute of Physics and Technology (National Research University) (141701, Russia, Moscow Region, Dolgoprudny, Institutsky Per., 9), Federal Research Center for Problems of Chemical Physics and Medicinal Chemistry of the Russian Academy of Sciences (142432, Russia, Moscow Region, Chernogolovka, Academician Semenov Prospekt, 1).

Dmitry Nikolaevich Pevtsov, Process Engineer, Junior Research Assistant, Moscow Institute of Physics and Technology (National Research University) (141701, Russia, Moscow Region, Dolgoprudny, Institutsky Per., 9). E-mail: pevtsov.dn@phystech.edu SPIN code 3117-5473, Author ID 1147563

Alexey Viktorovich Katsaba, Senior Research Assistant, Deputy Head of Laboratory, Candidate of Physics and Mathematics, Moscow Institute of Physics and Technology (National Research University) (141701, Russia, Moscow Region, Dolgoprudny, Institutsky Per., 9). E-mail: atsaba@sci.lebedev.ru SPIN code 5974-0289, Author ID 724698

Alexey Sergeevich Kirichenko, Senior Research Assistant, Candidate of Physics and Mathematics, Moscow Institute of Physics and Technology (National Research University) (141701, Russia, Moscow Region, Dolgoprudny, Institutsky Per., 9). E-mail: kirichenko@cosmos.ru SPIN code 9922-1027, Author ID 342444

Dmitry Viktorovich Demkin, Junior Research Assistant, Moscow Institute of Physics and Technology (National Research University) (141701, Russia, Moscow Region, Dolgoprudny, Institutsky Per., 9).

Valeria Antonovna Ivanova, Research Assistant, Candidate of Physics and Mathematics, Moscow Institute of Physics and Technology (National Research University) (141701, Russia, Moscow Region, Dolgoprudny, Institutsky Per., 9). E-mail: adu_99@mail.ru SPIN code 4277-9943, Author ID 1205481

Viktor Vladimirovich Ivanov, Director of the Institute of Quantum Technologies of Moscow Institute of Physics and Technology, Doctor of Physics and Mathematics, Corresponding Member of the Russian Academy of Sciences, Moscow Institute of Physics and Technology (National Research University) (141701, Russia, Moscow Region, Dolgoprudny, Institutsky Per., 9). E-mail: Ivanov.vv@mirt.ru SPIN code 1856-3914, Author ID 19128

Vladimir Fedorovich Razumov, Senior Research Assistant, Head of Laboratory, Doctor of Physics and Mathematics, Corresponding Member of the Russian Academy of Sciences, Moscow Institute of Physics and Technology (National Research University) (141701, Russia, Moscow Region, Dolgoprudny, Institutsky Per., 9). Federal Research Center for Problems of Chemical Physics and Medicinal Chemistry of the Russian Academy of Sciences (142432, Russia, Moscow Region, Chernogolovka, Academician Semenov Prospekt, 1). E-mail: azumov@icp.ac.ru SPIN code 1361-7759, Author ID 44050

PHOTOELECTRONICS =

UDC 621. PACS: 85.60.-g

EDN: KSQPZI

New sulfur precursor for synthesis of environmentally friendly colloidal quantum dots $CuInS_2$

© I. A. Shuklov*, A. V. Seraya, A. Y. Shalagin, V. V. Lim, T. Milenkovich, O. V. Vershinina, V. O. Yakovlev, V. S. Popov, V. V. Ivanov

Moscow Institute of Physics and Technology (National Research University),
Dolgoprudny, Moscow Region, 141701 Russia

* E-mail: shuklov.ia@mipt.ru

Received 29.11.2024; revised 4.02.2025; accepted 10.02.2025 Scientific specialty code: 1.3.11

A new sulfur precursor has been developed by dissolving the elemental sulfur in decene-1 at elevated temperatures and pressures. The synthesis of environmentally friendly colloidal quantum dots CuInS₂ for the visible range has been studied in details using this precursor. The influence of various reaction conditions like temperature, concentration as well as nature of indium precursor has been studied. For the obtained samples of nanoparticles, their composition and spectral characteristics have been described. The applicability of this sulfur precursor to obtain AgInS₂ nanoparticles has been demonstrated. Based on the materials derived, thin films have been produced and basic possiblity of photosensor preparation has been demonstrated.

Keywords: copper indium sulfide; hot injection synthesis; precursor; quantum dots.

DOI: 10.51368/1996-0948-2025-2-21-30

Opportunity for convenient directional change of the sensitivity spectrum range and of applying to substrates make the colloidal solutions of quantum dots particularly interesting for applications in electronics [1, 2]. In particular, the use of colloidal quantum dots for the visible range has already found commercial applications [3]. TV and computer monitors based on the QLED technology can be found in electronics supermarkets. This technology has been optimized to cut down the cost of devices and ensure their mass production. The synthesis of CdSe CQDs used in this technology as phosphors is well established [4]. However, a significant disadvantage of this technology is

the high toxicity of cadmium compounds used in production of CdSe CQDs and risk of environmental pollution in case of damaging the devices based on them [5, 6]. This circumstance is a strong constraint to production of solar cells based on CdSe CQDs.

As an alternative to CdSe CQDs, a number of other nanocrystals absorbing in the visible range can be used. Such nanocrystals are based on less toxic and more environmentally friendly inorganic materials, for example, perovskites $CsPbX_3$ or ternary indium chalcogenides I-III-VI of type $MInZ_2$ (M = Cu, Ag, Z = S, Se, Te) having a chalcopyrite crystal structure. The perovskites

featuring good optical properties have a very low stability to hydrolysis in humid air with a relative humidity of 50 % and higher [7, 8]. High sensitivity to moisture is one of the most important and difficult problems for implementation of perovskite-based solar cells. Ternary indium chalcogenides such as CuInS₂ and AgInS₂ seem to be more attractive materials because they exhibit absorption and luminescence in the visible range while being completely unsusceptible to hydrolysis [9]. Besides, quantum dots have high potential for being used in photocatalysis for wastewater treatment and water photodecomposition [10].

CuInS₂ has a band gap estimated to be 1.53 eV and exciton Bohr radius of 4 nm [11]. AgInS₂ has a band gap estimated to be 1.87 eV for the bulk material and exciton Bohr radius of 5.5 nm.

Triple points of indium sulfides are synthesized either by solvothermal or hightemperature colloidal method. Dodecanethiol-1 is most often used as a sulfur precursor for of CuInS₂ nanoparticles synthesis temperatures of 220–250 °C [12, 13]. In some cases, bis-trimethylsilyl sulfide [14], di-tertbutyl disulfide [15] and diphenylphosphine sulfide [16] were used. All the above reagents are sulfur precursors and are not produced by the Russian chemical industry, thus making the search for effective alternatives promising.

Findings and discussion

As part of our research efforts to find the alternative methods of synthesizing chalcogenide quantum dots, methods for obtaining CQDs of PbS and MTe (M = Cd, Hg, Pb, Zn) were proposed [17, 18].

To get the quantum dots of indium sulfides, it was decided to develop a sulfur precursor based on Russian-made decene-1. A precursor based on the elemental selenium dissolved in decene-1 was successfully used by us for synthesizing colloidal quantum dots

of HgSe [19]. Similarly, the elemental selenium solution in decene-1 was proposed for use. Sulfur vulcanization of rubber using elemental sulfur and the its related polymerization of alkenes in the presence of sulfur are fairly well-studied processes [20]. Reagents based on sulfur solutions in a longer-chain alkene, specifically octadecene-1, were previously used for synthesizing nanoparticles of PbS [21] and CuInS₂ [22], [23]. Unfortunately, Russian-made CdS octadecene-1 is currently not commercially available, for which reason we used decene-1.

Sulfur may be inserted into the C-H bond at lower temperatures than selenium. Sulfur is actually completely dissolved in decene-1 as early as at a temperature of 120 °C. Polysulfides prevail in resulting sulfur solution, which is confirmed by the chemical behaviour and spectral characteristics of resulting solutions. Thus, upon cooling the solutions made at 150 °C, the elemental sulfur is released to pass into solution again upon heating (Fig. 1). Temperature increase to 170 °C leads to irreversible dissolution of sulfur and getting solutions with a more intense color. Simultaneously, colored products can be observed in the absorption spectrum, the spectra of these products being similar to those of the described organic polysulfides [24, 25]. The absorption edge shifts to the region of longer waves during the reaction.

To study the formation of CuInS₂ nanoparticles, precursor formed a dissolving 0.4 M of sulfur in 10 ml of decene-1 at 150 °C was selected. Russian-made decane and cetane were tested as high-temperature use solvents. The of $(T_{boil} = 174 \, ^{\circ}C)$ allows synthesizing temperatures up to 150 °C, while the use of cetane $(T_{boil} = 286 \, ^{\circ}C)$ – at temperatures up to 250 °C. Higher synthesis temperatures are not achievable because initiating a reaction in the argon flow results in removal of the solvent with an inert gas flow from the reaction mixture at temperatures approaching boiling points. Indium halides (InCl₃ and InI₃) and

Table 1

indium stearate were tested as indium starting reagents. Due to their high hygroscopicity, indium halides are less convenient as metal precursors. For all tested systems, the mixture of copper chloride and indium salts forms homogeneous solutions in the oleylamine+alkane mixture at temperatures of about 100 °C. CuInS₂ CQD were synthesized by injecting the sulfur precursor into a mixture of metal precursors (see Table 1).

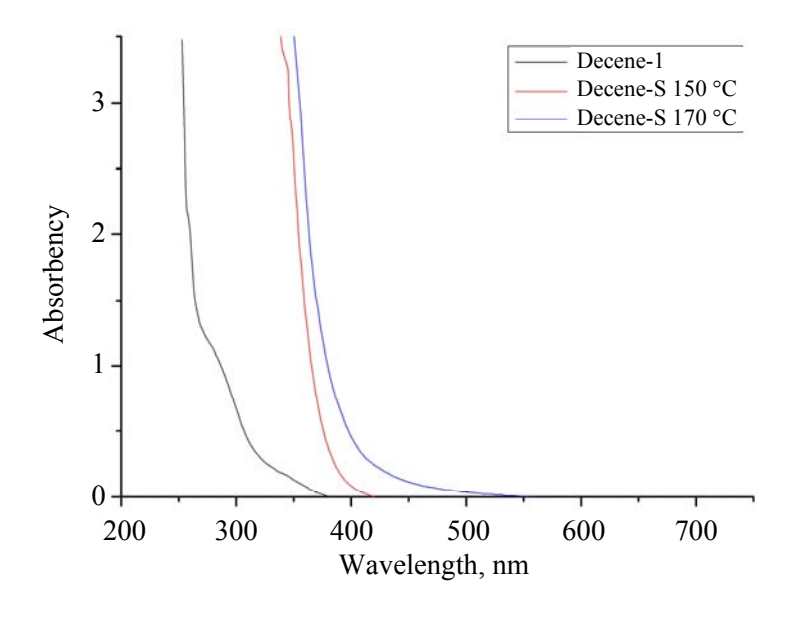


Fig. 1. Absorption spectra of decene and 0.4 M of elemental sulfur solution in 1-decene at different dissolution temperatures

Syntheses of CuInS₂, variations of indium precursors

| In precursor | Solvent | Temperature, °C | Particle size, nm | Standard size deviation, nm |
|------------------------------------|---------|-----------------|-------------------|-----------------------------|
| InCl ₃ | decane | 150 | 9.0 | 2.07 |
| InCl ₃ | cetane | 150 | 14.3 | 2.05 |
| InI_3 | decane | 150 | 4.9 | 0.84 |
| $In(OOCC_{17}H_{33})_3$ $(InSt_3)$ | decane | 150 | 19 | 3.30 |

Indium chloride, indium iodide and indium stearate were studied as indium precursors. When synthesizing CuInS₂ under the same conditions at 150 °C with the reaction terminated after 90 minutes, average particle size strongly depends on the metal precursor. The size and structure quantum characteristics of dots were determined by the transmission electron microscopy. The smallest average diameter equaling to 5 nm was determined for the particles obtained with indium iodide. While indium stearate was found to have the highest average particle size of 19 nm. The influence

of the medium on the average particle size was also investigated, and syntheses were carried out in decane and cetane with indium chloride as a precursor. Cetane allows synthesizing at higher temperatures.

In decane, nanoparticles of a smaller average size of 9 nm were obtained, while in cetane, under similar conditions, the average size of dots was 14 nm. This may be caused by the large difference in viscosity of these two alkanes, specifically 0.850 mPa·s for decane and 3.03 mPa·s for cetane. In a more viscous solvent, larger nanoparticles were obtained [26]. The larger the nanoparticles,

the higher the values of standard size deviations of nanoparticles are. It is worth noting that since indium halides are highly hydroscopic, it is difficult to weigh these salts in the normal atmosphere, while using indium stearate does not require special conditions for weighing.

The obtained quantum dots exhibit a clearly distinct luminescence maximum at 540 nm with all the precursors that have been studied, as well as at all studied temperatures from 110 °C to 150 °C with InCl₃ as a precursor (Fig. 2a). Similar behaviour was described previously for CuInS₂ nanoparticles synthesized by the solvothermal method [27]. This is explained by the fact that the size of the obtained nanoparticles exceeds the Bohr exciton radius for the given material. The luminescence intensity depends on the reaction conditions.

The shape of the absorption spectrum depends on the maximum particle size and size distribution with an absorption edge of about 650 nm (Fig. 2b). Analysis of TEM images (Fig. 3a) showed that the obtained CuInS₂ nanoparticles have the shape of tetrahedron and truncated tetrahedron, which is typical for this material. The size distribution (Fig. 3b) is approximated by the lognormal function, the

average particle size is about 9 nm.

Selected diffraction area electron (SAED) patterns obtained from the nanoparticles (Fig. 4a) indicate the presence of a crystalline phase of chalcopyrite CuInS₂2 with tetragonal syngony. The diffraction pattern contains reflections (112), (204), (312),which correspond to interplanar distances of 3.196, 1.959, 1.666 Å. The transmittance spectrum shows signals of stretching vibrations of C-H groups at 2923 cm⁻¹ (methylene) and 2853 cm⁻¹ (methyl), as well as deformations of CH2 group at 1464 cm⁻¹. Also a very broad absorption signal can be observed in the IR range, which is probably associated with an intraband transition in nanocrystals.

Based on the obtained sol, the creation of thin films of CQDs was studied. When applied on glass surfaces or on gold interdigitated electrodes on oxidized silicon, thin layer samples with a ligand shell substituted by thiocyanate anions were obtained using NH₄SCN in isopropanol (Fig. 5). According to AFM data, the obtained films have a smooth, even and uniform surface without pronounced edge effects with an observed average roughness of 10 nm at the film thickness of about 100 nm.

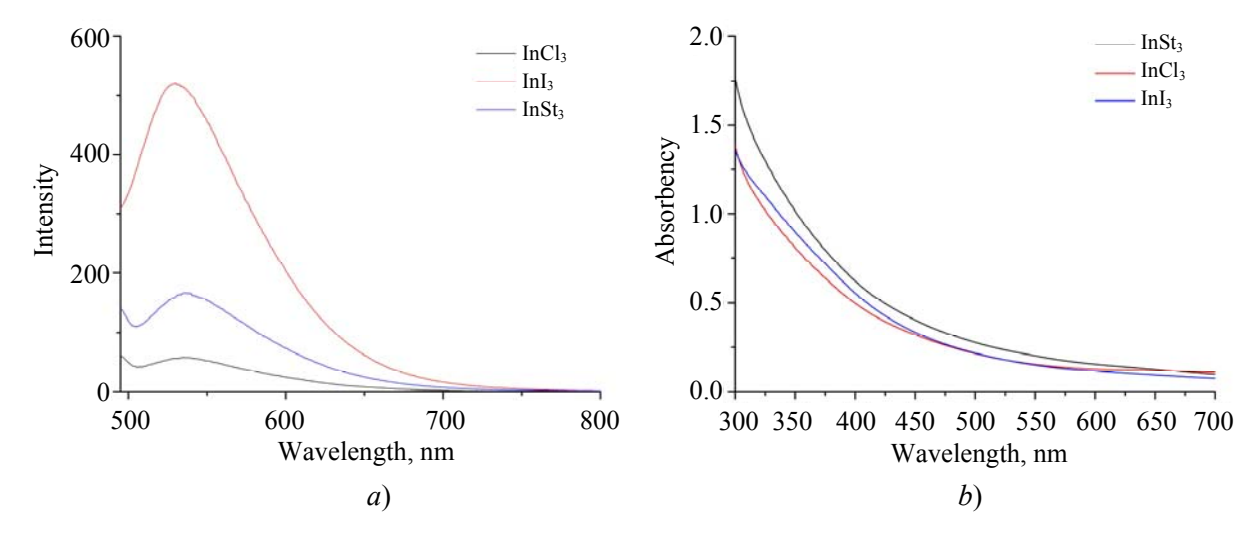


Fig. 2. Spectra of a) luminescence and b) absorption (visible range, 300–700 nm) of CuInS₂ CQDs obtained using different precursors at 150 °C in decane

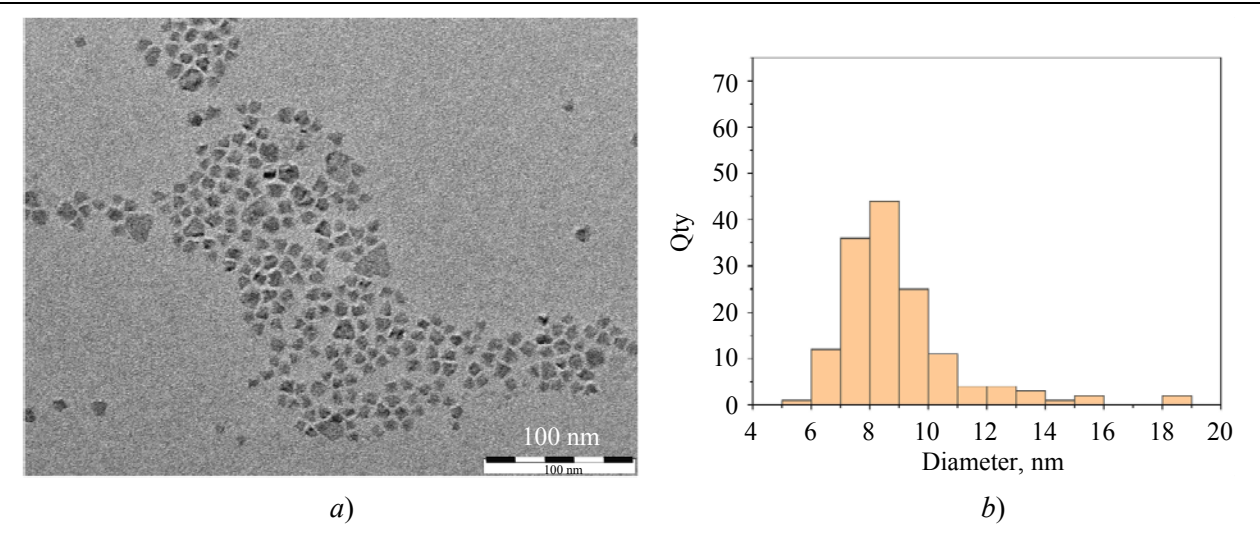


Fig. 3. a) TEM image and b) size distribution of CuInS₂ CQDs

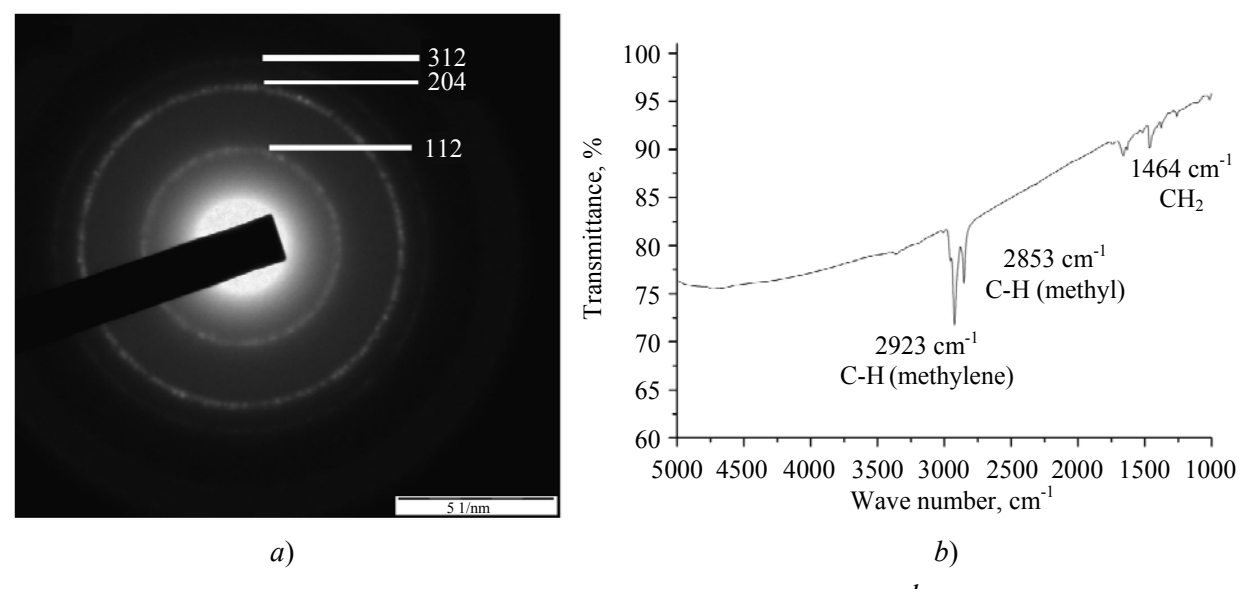


Fig. 4. a) SAED image; b) IR spectra in the range of 5000–1000 cm⁻¹; of CuInS₂ nanoparticles

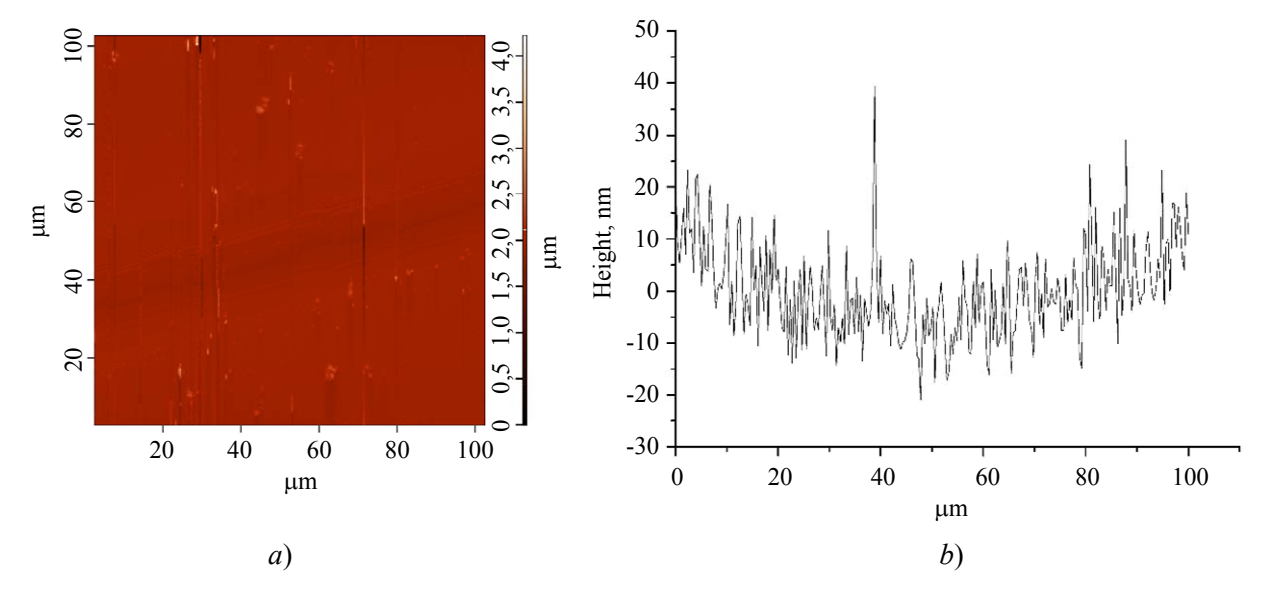


Fig. 5. Surface image and cut profile of CuInS₂ CQD film obtained by substitution of ligands

Photoresponses were measured using a proprietary setup, comprising Keithley 2636 B source measurement unit, with the sample illuminated orthogonally from a LED at the wavelength of 405 nm. During measurements, the cell containing the sample was blown with argon to eliminate effects induced by the surrounding atmosphere. In the course of measurements, the current flowing through a single photoresistor was measured over time at the constant voltage on the sample equaling to 1 V. The illumination duration was 30 s with a duty cycle of 2 (Fig. 6).

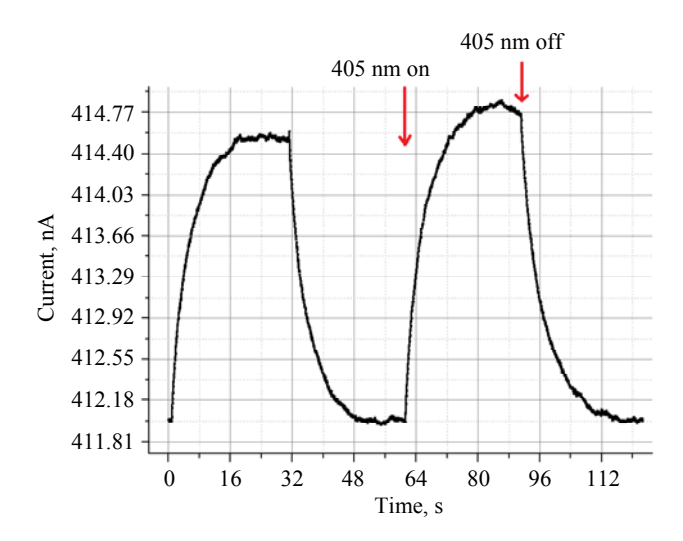


Fig. 6. Typical current vs. time dependence when switching the illumination on and off from the 405 nm source

The average photocurrent amplitude for the sample was 2.5 nA. The ampere-watt responsivity averaged to 19.5 μ A/W. Photocurrent rise time (time required for the photocurrent to increase from 10% to 90% of the maximum) and fall time (time required for the photocurrent to decrease from 90% to 10% of the maximum) of:

$$t_{0.1-0.9} = 10.8 \text{ s}$$

 $t_{0.9-0.1} = 9.21 \text{ s}$

The obtained high values of rise and fall times are generally not typical for detection processes based on the photon mechanism and may be contributed from thermal processes occurring in parallel.

The method developed for synthesizing CuInS₂ nanoparticles was used for synthesis of AgInS₂ nanoparticles. The method was established to be less general when applied to silver than when applied to copper. It is impossible to use indium halides precursor for the synthesis of these nanoparticles, since they form insoluble silver halides in the reaction conditions. When a mixture of indium stearate and silver is used, colloidal nanoparticles of AgInS₂ with an absorption peak maximum at 585 nm can be obtained. Changing the reaction time allows varying the optical properties of the resulting nanocrystals (Fig. 7).

It is planned to additionally research the use of this precursor for synthesizing nanocrystals of ABS_2 chalcopyrites, where A = Cu, Ag; B = Ga, In, Bi.

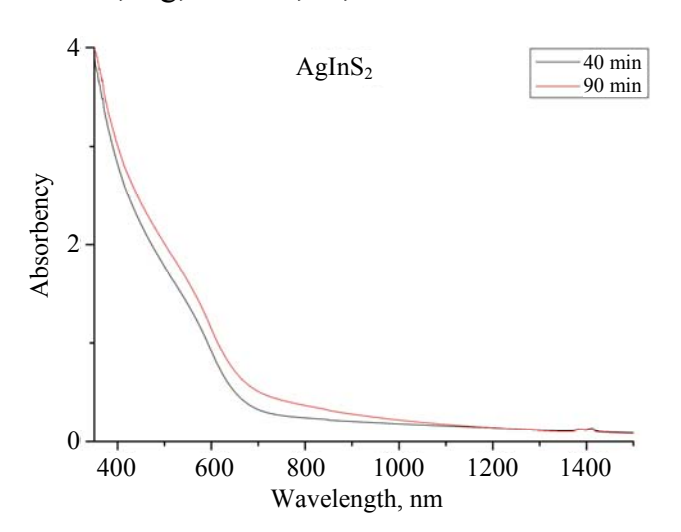


Fig. 7. Absorption spectra of AgInS₂ obtained at 150 $^{\circ}$ C

Experimental section

Chemicals.

The following chemicals were used for synthesis of CuInS₂ and AgInS₂ CQDs without further purification: copper chloride (99%, Lankhit), indium chloride (99%, Lankhit), indium iodide (99%, Lankhit), (99.99999%, Reakhim), decene-1 (90%, Vekton), silver nitrate (reagent grade, Vekton), hexane (99% **HPLC** MacronFineChemicals) and ethanol (reagent grade, Khimmed), decane (high purity, reagent grade), cetane (high purity, reagent grade), oleylamine (80–90 %, Acros), which was dried by heating (100 °C) under reduced pressure (1 mbar). Indium stearate was produced from metallic indium according to the method described in the literature [28]. Silver stearate was produced from silver nitrate [29].

Characterization.

The size, morphology and structure of nanoparticles was studied using JEM-2100 transmission electron microscope (TEM) by JEOL (Japan) featuring the accelerating voltage of 200 kV. The crystal structure was analyzed by comparing the interplanar distances measured on the obtained SAED images to the values from the database of crystal structures. The optical properties were evaluated by spectrophotometry methods using a spectrophotometer (JASCO V-770, JACSO) and by spectrometry using an IR Fourier spectrometer (Spectrum PerkinElmer) equipped with a multiple attenuated total internal reflection (MATIR) attachment fitted with Ge and ZnSe prisms (incidence angle – 45°, number of reflections – Keithley 4200A-SCS 25), source measurement unit, 405 nm laser. The surface morphology of thin films was studied using NT-MDT Solver-PRO atomic force microscope in the tapping mode.

Preparation of the sulfur precursor

The elemental sulfur (0.4 mmol (128 mg)) was placed in a thick-walled glass reactor together with 10 ml of 1-decene. The reaction mixture was heated at 150 °C in an oil bath while stirring it for 1 hour. The resulting light-yellow solution was used as a sulfur precursor for synthesizing nanocrystals.

General method for synthesis of $CuInS_2$ CQDs based on indium halides.

CuCl (2.97 mg, 0.03 mmol) and InX_3 (0.03 mmol, 6.7 mg of $InCl_3$ or 14.8 mg of

InI₃) were dissolved in a mixture of 0.2 ml of oleylamine and 5 ml of decane. The resulting mixture was heated in the argon flow at 110 °C for 60 min to form a homogeneous solution. The resulting mixture was diluted with decane to 30 ml and heated to 150 °C. A sulfur solution in decene-1 (7 ml) was injected at the specified temperature.

After the sulfur precursor was injected, the temperature of the reaction mixture drops and is maintained at the required level of the synthesis temperature. The reaction mixture turns brown as the reaction runs. After 90 minutes the flask is immersed in an ice bath. CuInS₂ nanoparticles are released by triple re-precipitation. CQDs were released purified adding and by 1:2 methanol:isopropanol mixture followed by centrifugation and re-dispersion in tetrachloroethylene characterization for purpose.

Method for synthesis of CuInS₂ CQDs based on indium stearate.

CuCl (2.97 mg, 0.03 mmol) and indium stearate (0.03 mmol, 6.7 mg of InCl₃ or 14.8 mg of InI₃) were dissolved in a mixture of 0.2 ml of oleylamine and 5 ml of decane. The resulting mixture was heated in the argon flow at 110 °C for 60 min to form a homogeneous solution. The resulting mixture was diluted with decane to 30 ml and heated to 150 °C. A sulfur solution in decene-1 (7 ml) was injected at the specified temperature.

After the sulfur precursor was injected, the temperature of the reaction mixture drops and is maintained at the required level of the synthesis temperature. The reaction mixture turns brown as the reaction runs. After 90 minutes the flask is immersed in an ice bath. CuInS₂ nanoparticles are released by triple re-precipitation. CQDs were released and purified by adding 1:2 methanol:isopropanol mixture followed by centrifugation re-dispersion and in tetrachloroethylene characterization for purpose.

*Method for synthesis of AgInS*₂ *CQDs*.

Silver stearate (11.8 mg, 0.03 mmol) and indium stearate (29.1 mg, 0.03 mmol) were dissolved in a mixture of 0.6 ml of oleylamine and 2 ml of decane. The resulting mixture was heated in the argon flow at 110 °C for 60 min to form a homogeneous solution. The resulting mixture was diluted with 22 ml of decane and heated to 150 °C. A sulfur solution in decene-1 (0.4 M, 6 ml) was injected at 150 °C. After the sulfur precursor was injected, the temperature of the reaction mixture drops and is maintained at the required level of the synthesis temperature. The reaction mixture turns brown as the reaction runs. After 90 minutes the flask is immersed in an ice bath. AgInS₂ nanoparticles released are by triple re-precipitation. CQDs were released and purified by adding 1:2 methanol:isopropanol mixture followed by centrifugation and re-dispersion in n-hexane.

Method of manufacturing a photoresistor based on CuInS₂ CQDs

50 µl of CuInS₂ colloidal quantum dots sol of the 10 mg/ml concentraion in hexane were deposited onto interdigital electrodes using spin-coating (speed - 4000 rpm, time 45 s). Ligands were substituted by applying 100 µl of the prepared solution of ammonium thiocyanate of the 20 mg/ml concentration in isopropanol to a fixed substrate, followed by acceleration to 4000 rpm by the spin-coating method (time 45 s). Excess of thiocyanate and reaction products were removed by applying 100 µl of isopropanol to the substrate by the spin-coating method (speed – 4000 rpm, time – 45 s). To achieve the required thickness, the application and substitution procedure was repeated.

Conclusion

For the first time, a sulfur precursor was obtained by dissolving sulfur in decene-1 at

an elevated temperature. Its optical properties and composition were studied by the spectrophotometry method. The new sulfur precursor was shown to be fit for preparation of colloidal quantum dots of indium chalcopyrites (CuInS₂ and AgInS₂) The resulting colloidal nanocrystals have a potential to replace environmentally-unsafe CQDs of cadmium selenide used in monitors and other photoelectronic devices, as well as for photocatalytic applications.

As an indium precursor, it is more practical to use indium stearate, due to its very low hygroscopicity as compared to indium halides. The resulting CuInS₂ nanocrystals feature a maximum in the emission spectrum in the visible range at 540 nm. On the basis of the resulting nanocrystals, photosensitive elements of the photoresistive type were created, with an ampere-watt responsivity of 19.5 µA/W, with the sample illuminated at a wavelength of 405 nm.

The paper has been prepared with the support by the Ministry of Science and Higher Education of the Russian Federation under agreement No. 075-03-2024-107 dated 17.01.2024. (Project No. FSMG-2024-0009).

REFERENCES

- 1. Ponomarenko V. P., Popov V. S., Shuklov I. A., Ivanov V. V. and Razumov V. F., Russ. Chem. Rev. **93** (4), RCR5113 (2024).
- 2. Shuklov I. A. and Razumov V. F., Russ. Chem. Rev. **89** (3), 379 (2020).
- 3. Shu Y., Lin X., Qin H., Hu Z., Jin Y. and Peng X., Angewandte Chemie **132** (50), 22496–22507 (2020).
- 4. Pu Y., Cai F., Wang D., Wang J.-X. and Chen J.-F., Industrial & Engineering Chemistry Research. **57** (6), 1790–1802 (2018).
- 5. Chakraborty D., Ethiraj K. R., Chandrasekaran N. and Mukherjee A., Environmental Pollution **270**, 116049 (2021).
- 6. Sharma V. K., McDonald T. J., Sohn M., Anquandah G. A. K., Pettine M. and Zboril R., Chemosphere **188**, 403–413 (2017).

- 7. Kore B. P., Jamshidi M. and Gardner J. M., Materials Advances. **5** (6), 2200–2217 (2024).
- 8. Zhou C., Tarasov A. B., Goodilin E. A., Chen P., Wang H. and Chen Q., Journal of Energy Chemistry. **65**, 219–235 (2022).
- 9. Yang W., Gong X. and Chang J., Journal of Nanoscience and Nanotechnology **16** (3), 2172–2183 (2016).
- 10. Coughlan C., Ibáñez M., Dobrozhan O., Singh A., Cabot A. and Ryan K. M., Chemical Reviews **117** (9), 5865–6109 (2017).
- 11. Czekelius C., Hilgendorff M., Spanhel L., Bedja I., Lerch M., Müller G., Bloeck U., Su D.-S. and Giersig M., Advanced Materials **11** (8), 643–646 (1999).
- 12. Zhong H., Zhou Y., Ye M., He Y., Ye J., He C., Yang C. and Li Y., Chemistry of Materials **20** (20), 6434–6443 (2008).
- 13. Rahman A., Jennings J. R. and Khan M. M., Materials Science in Semiconductor Processing **169**, 107930 (2024).
- 14. Niezgoda J. S., Harrison M. A., McBride J. R. and Rosenthal S. J., Chemistry of Materials **24** (16), 3294–3298 (2012).
- 15. Norako M. E., Franzman M. A. and Brutchey R. L., Chemistry of Materials **21** (18), 4299–4304 (2009).
- 16. Yu K., Ng P., Ouyang J., Zaman M. B., Abulrob A., Baral T. N., Fatehi D., Jakubek Z. J., Kingston D., Wu X., Liu X., Hebert C., Leek D. M. and Whitfield D. M., ACS Applied Materials & Interfaces 5 (8), 2870–2880 (2013).
- 17. Shuklov I. A., Mardini A. A., Skabitsky I. V., Dubrovina N. V., Perepukhov A. M.,

- Lizunova A. A. and Razumov V. F., Nano-Structures & Nano-Objects **35**, 101020 (2023).
- 18. Shuklov I. A., Toknova V. F., Lizunova A. A. and Razumov V. F., Materials Today Chemistry **18**, 100357 (2020).
- 19. Shuklov I. A., Milenkovich T., Majorova A. V., Vershinina O. V., Ivanova V. A., Pavlova V. D. and Popov V. S., Applied Physics, No. 1, 43–50 (2024) [in Russian].
- 20. Mutlu H., Ceper E. B., Li X., Yang J., Dong W., Ozmen M. M. *and* Theato P., Macromol. Rapid Commun. **40** (1), 1800650 (2019).
- 21. McPhail M. R. and Weiss E. A., Chem. Mater. **26** (11), 3377–3384 (2014).
- 22. Xia C., Winckelmans N., Prins P. T., Bals S., Gerritsen H. C. and de Mello Donegá C., Journal of the American Chemical Society **140** (17), 5755–5763 (2018).
- 23. Li Z., Ji Y., Xie R., Grisham S. Y. and Peng X., J. Am. Chem. Soc. **133** (43), 17248–17256 (2011).
- 24. Nakabayashi T., Tsurugi J. and Yabuta T., The Journal of Organic Chemistry **29** (5), 1236–1238 (1964).
- 25. Field L. Disulfides and Polysulfides. Organic Chemistry of Sulfur. Oae S. Boston, MA: Springer US, 1977, pp. 303–382.
- 26. Kim Y. H. and Lee J.-S., ACS Omega **7** (49), 45277–45286 (2022).
- 27. Li T.-L. and Teng H., Journal of Materials Chemistry **20** (18), 3656–3664 (2010).
- 28. Dou Q. and Ng K. M., Powder Technology **301**, 949–958 (2016).
- 29. Malik W. U., Jain A. K. and Jhamb O. P., J. Chem. Soc. A 1514–1517 (1971).

About authors

Ivan Alekseevich Shuklov, Leading Research Assistant, Associate Professor, Dr. rer. nat., Moscow Institute of Physics and Technology (National Research University) (141701, Russia, Moscow Region, Dolgoprudny, Institutsky Per., 9). E-mail: shuklov.ia@mipt.ru SPIN code 4060-7233, Author ID 1146575

Alexandra Valerievna Seraya, Engineer, Moscow Institute of Physics and Technology (National Research University) (141701, Russia, Moscow Region, Dolgoprudny, Institutsky Per., 9). E-mail: seraiaaleksandra@gmail.com SPIN code 8568-5395, Author ID 1288527

Vladimir Valerievich Lim, maintenance man, bachelor, Moscow Institute of Physics and Technology (National Research University) (141701, Russia, Moscow Region, Dolgoprudny, Institutsky Per., 9). E-mail: lim.vv@mipt.ru

Aleksandr Yurevich Shalagin, maintenance man, bachelor, Moscow Institute of Physics and Technology (National Research University) (141701, Russia, Moscow Region, Dolgoprudny, Institutsky Per., 9). E-mail: shalagin.au@mipt.ru SPIN code 9769-2552

Teodora Milenkovich, Junior Research Assistant, graduate student, Moscow Institute of Physics and Technology (National Research University) (141701, Russia, Moscow Region, Dolgoprudny, Institutsky Per., 9). E-mail: tmilenkovich@mail.ru

Olesya Valerievna Vershinina, Junior Research Assistant, graduate student, Moscow Institute of Physics and Technology (National Research University) (141701, Russia, Moscow Region, Dolgoprudny, Institutsky Per., 9). E-mail: seraia.ov@phystech.edu

Viktor Olegovich Yakovlev, Junior Research Assistant, master, Moscow Institute of Physics and Technology (National Research University) (141701, Russia, Moscow Region, Dolgoprudny, Institutsky Per., 9). E-mail: iakovlev.vo@mipt.ru

Viktor Sergeevich Popov, Head of Laboratory, Leading Research Assistant, Associate Professor, Candidate of Chemical Sciences, Moscow Institute of Physics and Technology (National Research University) (141701, Russia, Moscow Region, Dolgoprudny, Institutsky Per., 9). E-mail: popov.vs@mipt.ru SPIN code 1128-2332, Author ID 625948

Viktor Vladimirovich Ivanov, Senior Research Assistan, Professor, Doctor of Physics and Mathematics, Corresponding Member of the Russian Academy of Sciences. Moscow Institute of Physics and Technology (National Research University) (141701, Russia, Moscow Region, Dolgoprudny, Institutsky Per., 9). E-mail: Ivanov.vv@mirt.ru SPIN code 1856-3914, Author ID 19128

= PHOTOELECTRONICS =

UDC 538.958 PACS: 81.15.Hi EDN: KIJRKJ

Calculation of frequencies of mixed plasmon-phonon modes p-InSb and p-GaSb at T = 295 K

© A. G. Belov¹, E. V. Molodtsova¹, E. O. Zhuravlev¹, P. Yu. Kozlov¹, H. Yu. Komarovsky^{1,2,*}, A. N. Kuznetsov³, H. A. Larionov³

¹ Giredmet JSC, Moscow, 111524 Russia

* E-mail: nickkomarovskiy@mail.ru

² NUST MISIS, Moscow, 119049 Russia

³ RD&P Center ORION, JSC, Moscow, 111538 Russia

Received 22.01.2025; revised 21.02.2025; accepted 07.04.2025 Scientific specialty code: 2.2.3, 2.6.1

Theoretical calculations were carried out and values of light- and heavy-hole concentrations, as well as the effective mass of light holes, were derived for various values of the reduced Fermi level for p-InSb and p-GaSb at T=295 K. The calculations took into account the non-parabolic nature of the light-hole band. The values of wave numbers corresponding to the plasma frequency, as well as the frequency of the high-frequency mixed plasmon-phonon mode, were calculated. Calibration curves were built to relate the concentrations of light and heavy holes to the characteristic wave number corresponding to the frequency of the high-frequency mixed plasmon-phonon mode. These curves were shown to be described by second-degree polynomials.

Keywords: p-type indium antimonide; *p*-type gallium antimonide; light and heavy holes; mixed plasmon-phonon modes; free carrier concentration.

DOI: 10.51368/1996-0948-2025-2-31-38

Introduction

Giredmet JSC has been working to create a contactless, non-destructive method for monitoring the free carrier concentrations (FCC) in various semiconductor materials for several years. The method is based on the analysis of infrared reflection spectra of heavily doped semiconductor samples and finding the concentration of free electrons or holes (depending on the conductivity type of

the material). FCC is determined by the value of the characteristic wave number (v_+) corresponding to the frequency of the high-frequency mixed plasmon-phonon mode.

The efforts taken have laid the groundwork and studied the samples of *n*-InSb [1], *n*-InAs [2], *n*-GaSb [3], *n*-GaAs [4, 5], *p*-GaAs [6], with the optical measurements compared to the Hall data obtained for the same samples [2–6]. This article continues an earlier series of works.

It will describe the algorithm developed for determining the concentrations of light and heavy holes in heavily doped *p*-InSb and *p*-GaSb at the room temperature.

The infrared reflection spectrum of the sample under study is recorded using any optical instrument in the wave number range of $v \le 1500 \text{ cm}^{-1}$. The derived spectral dependence of the reflectivity is processed according to the standard procedure using the Kramers-Kronig relations. The frequency dependences of the real, ε_1 , and imaginary, ε_2 , parts of the complex dielectric permittivity $\varepsilon = \varepsilon_1 + i\varepsilon_2$, after which the so-called "loss function" is constructed:

$$LF = Im \left(-\frac{1}{\epsilon}\right) = \frac{\epsilon_2}{\epsilon_1^2 + \epsilon_2^2}.$$

The wave numbers matching the maxima of the loss function correspond to the frequencies of mixed plasmon-phonon modes: ν_- – low-frequency one, and ν_+ – high-frequency one. It is only the high-frequency mode that will be of interest for us, since it is directly related to free charge carriers (the low-frequency mode is

determined mainly by the crystal lattice of the material and is not suitable for determining the FCC value). By determining the value of v_+ by means of the calculated calibration curves, one can calculate the concentration values of light and heavy holes. Building these curves is the goal of this paper.

All the calculations were made for T = 295 K. Results of the calculations given herein are assumed to be further used for comparing the optical and electrophysical measurements of hole concentrations in p-InSb and p-GaSb samples.

Theoretical calculations

The valence band of all A_3B_5 semiconductors is known to consist of two subbands (light and heavy holes) degenerated at point Γ of the Brillouin zone. Fig. 1 shows the band structures of InSb (a) [7] and GaSb (b) [8]. The heavy-hole bands for these materials are isotropic and parabolic. The light-hole bands are described by the Kane dispersion law [9], i.e. the effective mass of light holes increases as the energy grows.

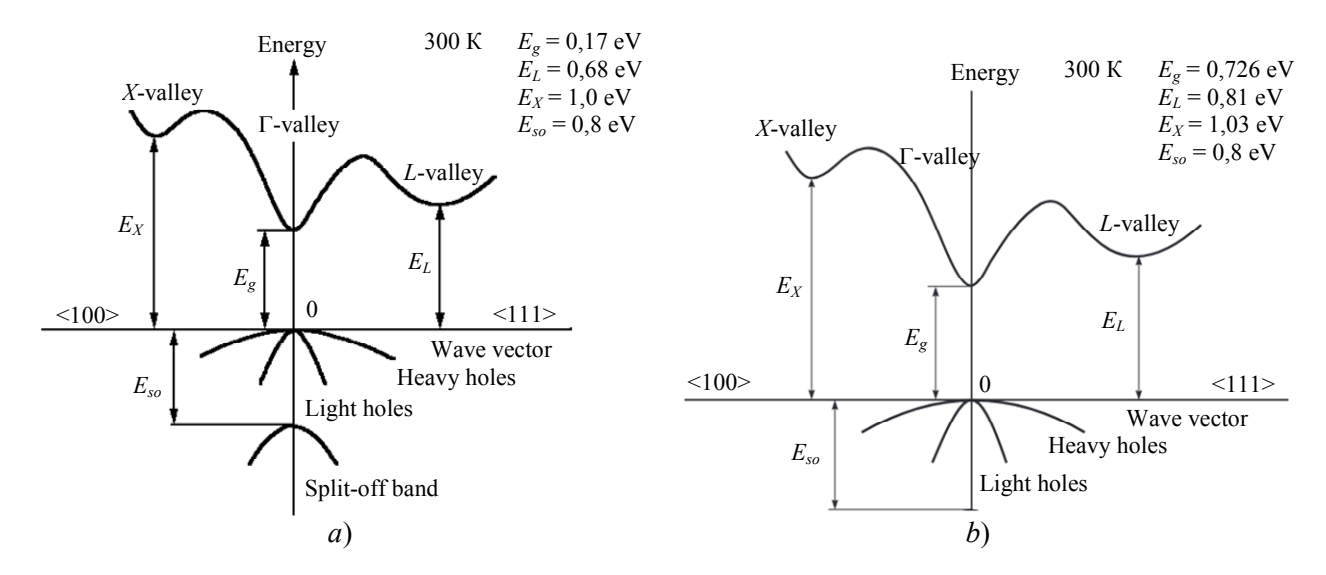


Fig. 1. Band structure of InSb (a) [7] and GaSb (b) [8]

When free charge carriers of two types are present, the plasma frequency is known to be written as [10]:

$$\omega_{p}^{2} = \frac{4\pi e^{2}}{\varepsilon_{\infty}} \times \left(\frac{p_{H}}{m_{p_{H}}} + \frac{p_{L}}{m_{p_{L}}}\right) =$$

$$= \frac{4\pi e^{2} p_{H}}{\varepsilon_{\infty} m_{p_{H}}} \times \left(1 + \frac{p_{L} m_{p_{H}}}{p_{H} m_{p_{L}}}\right). \tag{1}$$

Here $p_{\rm H}$, $p_{\rm L}$ are concentrations of heavy and light holes, respectively; $m_{p_{\rm H}}$ and $m_{p_{\rm L}}$ are their optical effective masses; ε_{∞} is the high-frequency dielectric permittivity; $e = 4.8 \times 10^{-10}$ units. CGSE – electron charge.

The second term in the brackets of formula (1) characterizes the contribution of light holes to the plasma frequency.

For the concentration of heavy holes (parabolic band) the relation [11] is true:

$$p_{\rm H} = \frac{8\pi}{3h^3} \times \left(2m_{p_{\rm H}}kT\right)^{\frac{3}{2}} \times F_{\frac{3}{2}}(\eta)$$
 (2)

Here $F_{\frac{3}{2}}(\eta)$ is one-parameter Fermi integral:

$$F_{\frac{3}{2}}(\eta) = \int_{0}^{\infty} \left(-\frac{\partial f_0}{\partial x}\right) x^{\frac{3}{2}} dx, \tag{3}$$

where
$$f_0(x,\eta) = \left[1 + \exp(x - \eta)\right]^{-1}$$
; (4)

 $\eta = \frac{E_F}{kT}$ is the reduced Fermi level (counted down from the top of the heavy-hole valence band – see Fig. 1).

The light-hole band is non-parabolic (Kane model [9]); in this case, the light-hole concentration is described by relation [11]:

$$p_{L} = \frac{\sqrt{3}}{2\sqrt{2}\pi^{2}} \times \frac{\left(kTE_{g}\right)^{\frac{3}{2}}}{P_{cv}^{3}} \times {}^{0}L_{0}^{\frac{3}{2}}(\eta, \beta)$$
 (5)

The effective mass of light holes can be calculated by formula [12, Appendix A]:

$$\frac{m_{p_{L}}}{m_{0}} = \frac{3\hbar^{2}E_{g}}{4P_{cv}^{2}m_{0}} \times \frac{{}^{0}L_{0}^{\frac{3}{2}}(\eta,\beta)}{{}^{0}L_{1}^{\frac{3}{2}}(\eta,\beta)}$$
(6)

Here E_g is semiconductor's band gap; $k = 1.38 \times 10^{-16}$ erg/K is Boltzmann constant; (for T = 295 K kT = 25.4 meV); $\hbar = h/2\pi$, where $h = 6.62 \times 10^{-27}$ erg·s is Plank's constant; $m_0 = 9.11 \times 10^{-28}$ g is free-electron mass; $P_{cv} = 8.7 \times 10^{-8}$ eV·cm [13] is matrix element of interaction between the light-hole valence band and conduction band, considered to be the same for all compounds A_3B_5 ; $\beta = kT/E_g$ is parameter characterizing the non-parabolic nature of the light-hole band.

Formulas (5) and (6) use two-parameter Fermi integrals:

$$^{m}L_{k}^{n}\left(\eta,\beta\right) = \int_{0}^{\infty} \left(-\frac{\partial f_{0}}{\partial x}\right) \frac{x^{m}\left(x+\beta x^{2}\right)^{n}}{\left(1+2\beta x\right)^{k}} dx \qquad (7)$$

The two-parameter integral ${}^{0}L_{0}^{\frac{3}{2}}(\eta, \beta)$ changes for a one-parameter integral $F_{\frac{3}{2}}(\eta)$ at

 $\beta \rightarrow 0$, the case when the non-parabolic nature of the band can be neglected.

Since the materials under consideration contain one heavy-hole band and one light-hole band, and both are isotropic, values of states density effective masses coincide with values of the optical effective masses – see formulas (1), (2), (5), (6).

Semiconductor materials A₃B₅ contain a noticeable proportion of ionic bond, therefore longitudinal optical vibrations of the crystal lattice (LO phonons) can interact with longitudinal collective vibrations of the system of free charge carriers – plasmons (plasmon-phonon coupling). This coupling shall be considered when building calibration curves relating the FCC values to the characteristic wave numbers.

If the damping of plasmons and LO phonons is neglected, the frequency dependence of the permittivity is written as:

$$\varepsilon(\omega) = \varepsilon_{\infty} \left[1 - \left(\frac{\omega_{p}}{\omega} \right)^{2} \right] + \frac{\varepsilon_{0} - \varepsilon_{\infty}}{1 - \left(\frac{\omega}{\omega_{LO}} \right)^{2} \times \frac{\varepsilon_{0}}{\varepsilon_{\infty}}}, \quad (8)$$

where ϵ_0 is static dielectric permittivity; ω is circular frequency; ω_{LO} is the frequency of the longitudinal optical phonon. The first term in formula (8) describes the plasmons' contribution, and the second term – the contribution from longitudinal optical phonons.

Longitudinal vibrations (which is what mixed plasmon-phonon modes are) are known to be able to exist in a medium only if the dielectric permittivity turns to zero. Accordingly, after equating expression (8) to zero and solving the biquadratic equation, thus switching from frequencies to wave numbers for v_- and v_+ , we will have:

$$v_{\pm}^{2} = \frac{1}{2} \left[\left(v_{p}^{2} + v_{LO}^{2} \right) \pm \sqrt{\left(v_{p}^{2} + v_{LO}^{2} \right)^{2} - 4 \frac{\varepsilon_{\infty}}{\varepsilon_{0}} v_{p}^{2} v_{LO}^{2}} \right]$$
(9)

Further only high-frequency mode v_+ will be of interest for us.

The calculating algorithm is as follows:

- setting the value η and calculating the values $p_{\rm H}$, $p_{\rm L}$ and $\frac{m_{p_{\rm L}}}{m_0}$ by formulas (2), (5) and (6);

- substituting the derived values into formula (1) and calculating the value of plasma frequency ω_p and the corresponding wave number value: $v_p = \frac{\omega_p}{2\pi c}$, where $c = 3 \times 10^{10}$ cm/s is the speed of light in a vacuum;

- substituting the derived value of v_p into formula (9) and calculating the value of v_+ ;
- changing the value η and repeating the above steps;
- building calibration curves of the heavy- and light-hole concentrations vs. characteristic wave number: $p_H = f_1(v_+)$ and $p_L = f_2(v_+)$.

The following parameter values were used in the calculations:

for InSb:

$$E_g = 0.17 \text{ eV}$$
 [7]; $\beta = 0.149$; $\epsilon_0 = 18.0$, $\epsilon_{\infty} = 15.68$ [13]; $m_{p_{\text{H}}} = 0.43 m_0$; [7]; $v_{\text{LO}} = 197.2 \text{ cm}^{-1}$ [13]; for GaSb:

$$E_g = 0.728 \text{ eV [8]};$$
 $\beta = 0.0349;$ $\epsilon_0 = 16.4, \ \epsilon_\infty = 15.2 \text{ [13]}; \ m_{p_{\text{H}}} = 0.40 \ m_0; \ \text{[8]};$ $v_{\text{LO}} = 240.3 \text{ cm}^{-1} \text{ [13]}.$

Considering the above, formulas (2), (5) and (6) can be reduced to the following: for InSb:

$$p_{\rm H} = 5.185 \times 10^{18} \times F_{\frac{3}{2}}(\eta);$$
 (10)

$$p_{\rm L} = 2.676 \times 10^{16} \times {}^{0}L_{0}^{\frac{3}{2}} (\eta; 0.149)$$
 (11)

$$\frac{m_{p_{\rm L}}}{m_0} = 0.0128 \frac{{}^{0}L_0^{\frac{3}{2}}(\eta; \ 0.149)}{{}^{0}L_1^{\frac{3}{2}}(\eta; \ 0.149)}; \tag{12}$$

for GaSb:

for InSb:

$$p_{\rm H} = 4.651 \times 10^{18} \times F_{\frac{3}{2}}(\eta); \qquad (13)$$

$$v_p = 1.152 \times 10^{-7} \times \sqrt{p_{\rm H} \left(1 + \frac{p_{\rm L} m_{p_{\rm H}}}{p_{\rm T} m_{p_{\rm L}}}\right)}; \qquad (16)$$

$$p_{\rm L} = 2.376 \times 10^{17} \times {}^{0}L_{0}^{\frac{3}{2}} (\eta; 0.0349)$$
 (14)

for GaSb:

$$\frac{m_{p_{\rm L}}}{m_0} = 0.0550 \frac{{}^{0}L_0^{\frac{3}{2}}(\eta; 0.0349)}{{}^{0}L_1^{\frac{3}{2}}(\eta; 0.0349)}$$
(15)
$$v_{\rm p} = 1.213 \times 10^{-7} \times \sqrt{p_{\rm H} \left(1 + \frac{p_{\rm L} m_{p_{\rm H}}}{p_{\rm H} m_{p_{\rm L}}}\right)}$$
(17)

Formula (1) can be transformed as follows:

Tables 1 and 2 present the parameter values calculated by the above formulas.

Table 2

Table 1
Calculation results for p-InSb (T = 295 K)

| η | $p_{ m H},{ m cm}^{-3}$ | $p_{\mathrm{L}},\mathrm{cm}^{	ext{-}3}$ | $\frac{m_{p_{\mathrm{L}}}}{m_{0}}$ | v_p , cm ⁻¹ | ν ₊ , cm ⁻¹ |
|------|-------------------------|---|------------------------------------|--------------------------|-----------------------------------|
| -1.0 | 2.261×10 ¹⁸ | 1.939×10^{16} | 2.285×10 ⁻² | 186.6 | 224.1 |
| -0.5 | 3.500×10^{18} | 3.040×10^{16} | 2.315×10 ⁻² | 232.2 | 253.9 |
| 0 | 5.273×10 ¹⁸ | 4.664×10^{16} | 2.359×10 ⁻² | 285.0 | 298.8 |
| 0.5 | 7.700×10^{18} | 6.971×10^{16} | 2.417×10 ⁻² | 344.4 | 354.2 |
| 1.0 | 10.863×10 ¹⁸ | 10.124×10 ¹⁶ | 2.492×10 ⁻² | 409.0 | 416.5 |
| 1.5 | 14.782×10 ¹⁸ | 14.272×10 ¹⁶ | 2.583×10 ⁻² | 477.1 | 483.2 |
| 2.0 | 19.464×10 ¹⁸ | 19.555×10 ¹⁶ | 2.690×10 ⁻² | 547.5 | 552.6 |
| 2.5 | 24.862×10 ¹⁸ | 26.097×10 ¹⁶ | 2.810×10 ⁻² | 618.8 | 623.2 |
| 3.0 | 30.934×10 ¹⁸ | 34.017×10 ¹⁶ | 2.941×10 ⁻² | 690.2 | 694.1 |

Calculation results for p-GaSb (T = 295 K)

| Cucumon resums for p Gusto (1 273 K) | | | | | | |
|--------------------------------------|--|-------------------------------|------------------------|--------------------------|-----------------------------------|--|
| η | <i>p</i> _H , cm ⁻³ | $p_{ m L}$, cm $^{	ext{-}3}$ | $rac{m_{p_L}}{m_0}$ | v_p , cm ⁻¹ | ν ₊ , cm ⁻¹ | |
| -1.0 | 2.028×10 ¹⁸ | 1.188×10 ¹⁷ | 6.513×10 ⁻² | 186.5 | 250.9 | |
| -0.5 | 3.139×10 ¹⁸ | 1.839×10^{17} | 6.535×10 ⁻² | 232.0 | 266.4 | |
| 0 | 4.730×10 ¹⁸ | 2.787×10^{17} | 6.580×10 ⁻² | 284.7 | 302.1 | |
| 0.5 | 6.907×10^{18} | 4.098×10^{17} | 6.635×10 ⁻² | 344.1 | 354.6 | |
| 1.0 | 9.744×10 ¹⁸ | 5.833×10 ¹⁷ | 6.711×10 ⁻² | 408.7 | 416.1 | |
| 1.5 | 13.260×10 ¹⁸ | 8.028×10^{17} | 6.802×10 ⁻² | 476.6 | 482.3 | |
| 2.0 | 17.460×10 ¹⁸ | 10.706×10 ¹⁷ | 6.907×10 ⁻² | 546.8 | 551.5 | |
| 2.5 | 22.301×10 ¹⁸ | 17.530×10 ¹⁷ | 7.158×10 ⁻² | 627.5 | 631.4 | |
| 3.0 | 27.748×10 ¹⁸ | 26.302×10 ¹⁷ | 7.445×10 ⁻² | 708.1 | 711.4 | |

As can be seen in Tables 1 and 2, the difference between the values of v_p and v_+ decreases as the hole concentrations increase, i.e. the influence of plasmon-phonon coupling weakens.

Using the data in Tables 1 and 2, one can built calibration curves relating hole concentrations to the characteristic wave number v_+ :

for InSb:

for heavy holes:

$$p_{\rm H} = 6.012 \times 10^{13} \times (\nu_{+})^{2} + 5.387 \times 10^{15} \times (\nu_{+}) - 1.814 \times 10^{18};$$
(18)

for light holes:

$$p_{L} = 9.628 \times 10^{11} \times (v_{+})^{2} - 2.136 \times 10^{14} \times (v_{+}) + 2.209 \times 10^{16};$$
(19)

for GaSb: for heavy holes:

$$p_{\rm H} = 3.246 \times 10^{13} \times (\nu_{+})^{2} + 2.390 \times 10^{16} \times (\nu_{+}) - 5.699 \times 10^{18};$$
(20)

for light holes:

$$p_{L} = 1.106 \times 10^{13} \times (v_{+})^{2} - 5.539 \times 10^{15} \times (v_{+}) + 8.965 \times 10^{16}.$$
 (21)

All the calibration curves are described by second-degree polynomials.

Fig. 2 shows the calibration curves for heavy holes for p-InSb, p-GaAs and p-GaSb at T = 295 K for comparison purpose.

As can be seen in Fig. 2, the difference between the values of heavy-hole concentration for the listed semiconductor materials increases as the values of ν_+ increase.

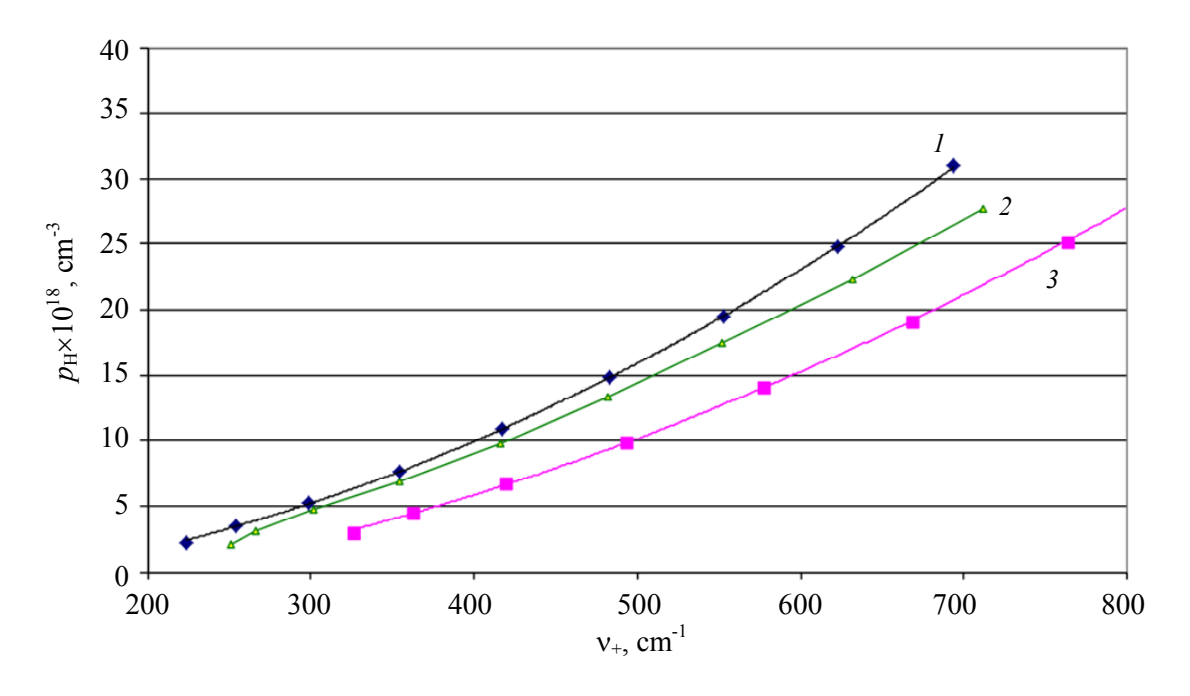


Fig. 2. Calculated calibration curves of the heavy-hole concentration: vs the characteristic wave number: curve 1 - p-Insb; curve 2 - p-GaSb; curve 3 - p-GaAs

The findings described in this paper are planned to be used for analyzing the data of optical and electrophysical measurements of *p*-InSb and *p*-GaSb samples. The same approaches were earlier used by us for *n*-GaSb [3] and *p*-GaAs [6] materials.

Conclusion

Calculations were carried out to derive the values of concentrations of light and heavy holes, effective mass of light holes, as well as frequencies of plasmons and mixed plasmon-phonon modes for p-InSb and p-GaSb at T = 295 K for various values of the reduced Fermi level. The calculations took into account the non-parabolic nature of the light-hole band.

Calibration curves were built to relate the concentrations of light and heavy holes to the characteristic wave number corresponding to the frequency of the high-frequency mixed plasmon-phonon mode. All the curves derived were shown to be described by second-degree polynomials.

REFERENCES

- 1. Belova I. M., Belov A. G., Kanevskiy V. E. and Lysenko A. P., Izvestiya vuzov. Elektronika **22** (3), 201–210 (2017). doi:10.214151/1561-5405-2017-22-3-201-210 [in Russian].
- 2. Yugova T. G., Belov A. G., Kanevskiy V. E., Kladova E. I., Knyazev S. N. and Parfent'eva I. B., Izvestiya vuzov. Materialy elektronnoy tekhniki **24** (3), 153–161 (2021). https://doi.org/10.17073/1609-3577-2021-3-153-161 [in Russian].

- 3. Belov A. G. Molodtsova E. V., Kormilitsina S. S., Kozlov R. Yu., Zhuravlev E. O., Klimin S. A., Novikova N. N. and Yakovlev V. A., Optika i spektroskopiya **131** (7), 919–925 (2023). doi: 10.21883/OS.2023.07.56126,4318-23 [in Russian].
- 4. Yugova T. G., Belov A. G., Kanevskij V. E., Kladova E. I. and Knyazev S. N., Izvestiya vuzov. Materialy elektronnoj tekhniki **23** (1), 27–33 (2020). doi: 10.17073/1609-3577-2020-1-27-33 [in Russian].
- 5. Komarovskiy N. Yu., Belov A. G., Kladova E. I., Knyazev S. N., Molodtsova E. V., Parfent'eva I. B. and Trofimov A. A., Applied Physics, № 6, 54–59 (2023). doi: 10.51368/1996-0948-2023-6-54-59 [in Russian].
- 6. Belov A. G., Kanevskiy V. E., Kladova E. I., Knyazev S. N., Komarovskiy N. Yu., Parfent'eva I. B. and Chernyshova E. V., Izvestiya vuzov. Materialy elektronnoy tekhniki **26** (3), 171–180 (2023).

https://doi.org/10.17073/1609-3577j.met202304.525 [in Russian].

- 7. New semiconductor materials. Biology systems. Characteristic and properties. Band structure and carrier concentration of indium antimonide (InSb). URL https://www.ioffe.ru/SVA/NSM/Semicond/InSb/bandstr.html.
- 8. New semiconductor materials. Biology systems. Characteristic and properties. Band structure and carrier concentration of gallium antimonide (GaSb). URL https://www.ioffe.ru/SVA/NSM/Semicond/GaSb/bandstr.html.
- 9. Kane E. O., Journal of Physics and Chemistry of Solids **1** (4), 249–261 (1957).

https://doi.org/10.1016/0022-3697(57)90013-6.

- 10. Pozhela Yu. K., Plazma i tokovye neustojchivosti v poluprovodnikah. Moscow, Nauka, 1977 [in Russian].
- 11. Askerov B. M., Kineticheskie effekty v poluprovodnikah. Moscow, Nauka, 1970 [in Russian].
- 12. Ravich Yu. I., Efimova B. A. and Smirnov I. A., Metody issledovaniya poluprovodnikov v primenenii k hal'kogenidam svintsa PbTe, PbSe, PbS. Moscow, Nauka, 1968 [in Russian].
- 13. Madelung O., Fizika poluprovodnikovyh soedineniy elementov III-V grupp; per. s angl. Moscow, Mir, 1967 [in Russian].

About authors

Alexander Georgievich Belov, Leading Research Assistant, Candidate of Physics and Mathematics, Giredmet JSC (111524, Russia, Moscow, Elektrodnaya Ulitsa, 2, bld 1). E-mail: IADenisov@rosatom.ru SPIN code 9546-0477, Author ID 38536

Elena Vladimirovna Molodtsova, Leading Research Assistant, Candidate of Technical Sciences, Giredmet JSC (111524, Russia, Moscow, Elektrodnaya Ulitsa, 2, bld 1). E-mail: evmol@bk.ru

Evgeny Olegovich Zhuravlev, Research Assistant, Giredmet JSC (111524, Russia, Moscow, Elektrodnaya Ulitsa, 2, bld 1).

Roman Yurievich Kozlov, Head of Laboratory, Giredmet JSC (111524, Russia, Moscow, Elektrodnaya Ulitsa, 2, bld 1). E-mail: RYKozlov@rosatom.ru

Nikita Yuryevich Komarovsky, Head of the research group, Giredmet JSC (111524, Russia, Moscow, Elektrodnaya Ulitsa, 2, bld 1), NUST MISIS (119049, Russia, Moscow, Leninsky Prospekt, 4, bld. 1). E-mail: nickkomarovskiy@mail.ru SPIN code 9642-8920, Author ID 1248206

Anton Nikolaevich Kuznetsov, Head of the Photonuclear Experiments Data Center, RD&P Center ORION, JSC (111538, Russia, Moscow, Kosinskaya Ulitsa, 9). E-mail: Kuznetsov.Ant.N@yandex.ru

Nikita Alexandrovich Larionov, Engineer Cat. 1, RD&P Center ORION, JSC (111538, Russia, Moscow, Kosinskaya Ulitsa, 9). E-mail: nikitalarionov16@yandex.ru SPIN code 1288-6349, Author ID 1242982

= PHOTOELECTRONICS =

UDC 621 EDN: GYTPJU

Defects formation in SiO₂ layer during diffusion processes in silicon

© K. O. Boltar^{1,2}, M. N. Vildyaeva¹, N. A. Irodov¹, E. A. Klimanov^{1,3,*}, A. V. Lyalikov¹, V. A. Malygin¹, D. S. Molchanov¹, E. A. Makarova¹

¹ RD&P Center ORION, JSC, Moscow, 111538 Russia

* E-mail: klimanov3@mail.ru

² Moscow Institute of Physics and Technology (National Research University),

Moscow Region, Dolgoprudny, 141701 Russia

³ MIREA – Russian Technological University (RTU MIREA), Moscow, 119454 Russia

Received 13.12.2024; revised 13.03.2025; accepted 07.04.2025 Scientific specialty code: 1.3.11

The influence of diffusion of phosphorus from a liquid source (POCl3) and a solid source (aluminum metaphosphate (AMP)) on the formation of local defects in SiO_2 layers on the silicon surface has been analyzed. The probable cause of defects formation has been established to be local melt-through of the oxide layer by liquid phosphorus-silicate glass due to a silicon-rich solid phase formation. The defect depth is proportional to its diameter and decreases as the process temperature drops.

Keywords: defect, diffusion, silicon. DOI: 10.51368/1996-0948-2025-2-39-45

1. Introduction

The cycle of manufacturing silicon photodiodes typically involves the diffusion concentrations of high of boron phosphorus to form doped regions and p-niunctions. The process of phosphorus diffusion often leads to the formation of local defects in the dielectric layers acting as a protective mask [1–4]. The said defects can give rise to the local n^+ channels in p^+ -n junctions, thus causing leakage currents therein, as well as defects in MOS-IC and CCD structures.

The goal of this paper is to study the formation patterns of these defects in order to

determine the conditions reducing their influence on leakage currents of p^+-n junctions.

2. Experiment

To determine the defect parameters (morphology, size and concentration), samples with p^+-n junctions sized $1.4\times1.4 \text{ mm}^2$ were made using wafers of monocrystalline silicon (Cz-Si) of *n*-type with a diameter of 100 mm, a specific resistance of $4-5 \Omega \cdot \text{cm}$ and orientation (100).

The manufacturing cycle included the oxidation in H₂O+HCl, vapor,

photolithography, predeposition (deposition) of boron from boron nitride BN wafers at a temperature of 1000 °C, boron diffusion (drive-in), predeposition (deposition) of phosphorus from a liquid source (POCl₃) and solid source wafers (aluminum metaphosphate (AMP) at temperatures of 900–1050 °C. The duration of phosphorus predeposition at different temperatures was selected within the range of 10–40 minutes in order to ensure the same thickness of the phosphorsilicate glass (PSG).

The concentration and distribution of local defects over the plate were determined on the manufactured samples using an optical microscope. A scanning electron microscope, an atomic force microscope and a profilometer were used to determine the size and shape of defects. The constituent elements of defects were determined by X-ray spectroscopy.

3. Results

Major results are summarized below.

- 1. Most oxide defects that can be observed are pits of round shape with a diameter of 2 to 40 μm , with the depth proportional to their diameter (Fig. 1). When the defect depth reached the value equal to the SiO₂ thickness, through holes could be seen (in an oxide of 0.4 μm in thickness with a pit diameter more than 10 μm). The distributions of defects by diameter and depth are correlated with each other and are shown in Fig. 2.
- 2. The defect surface profile depends on its depth and diameter. Smooth walls can be observed on the surface profile of the defect with a depth of $0.15\text{--}0.2~\mu\text{m}$. If the defect depth increases and approach to the dielectric thickness, a rough profile can be observed (Fig. 3).

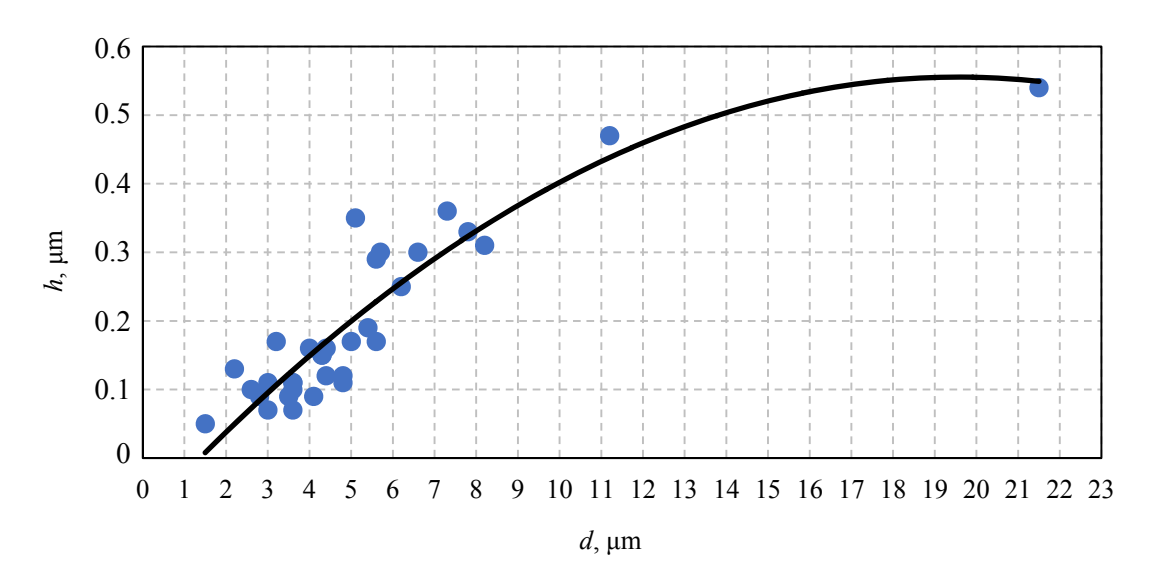
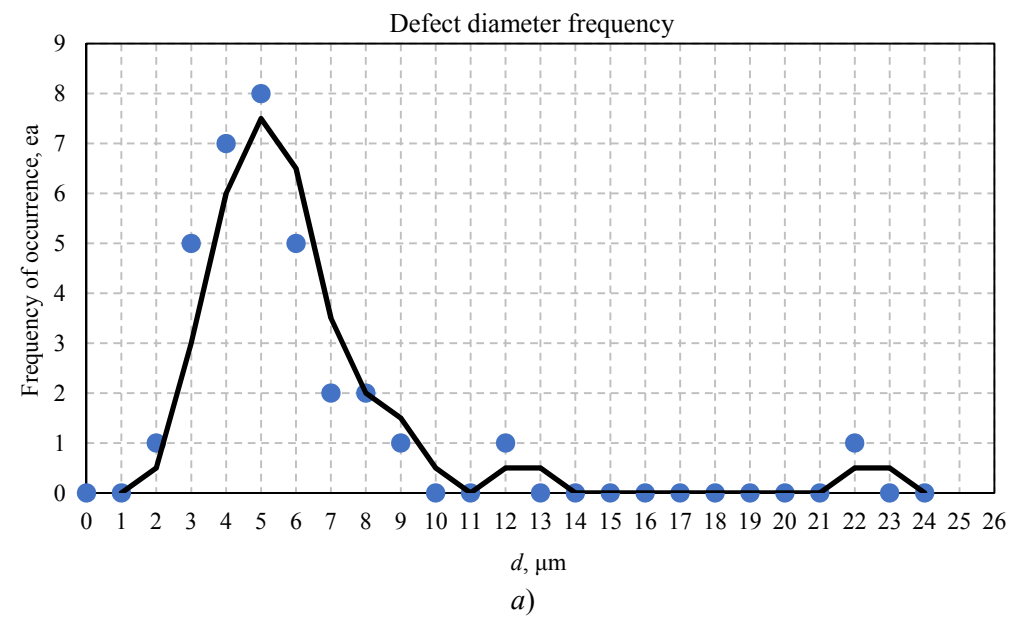


Fig. 1. Defect depth vs defect diameter



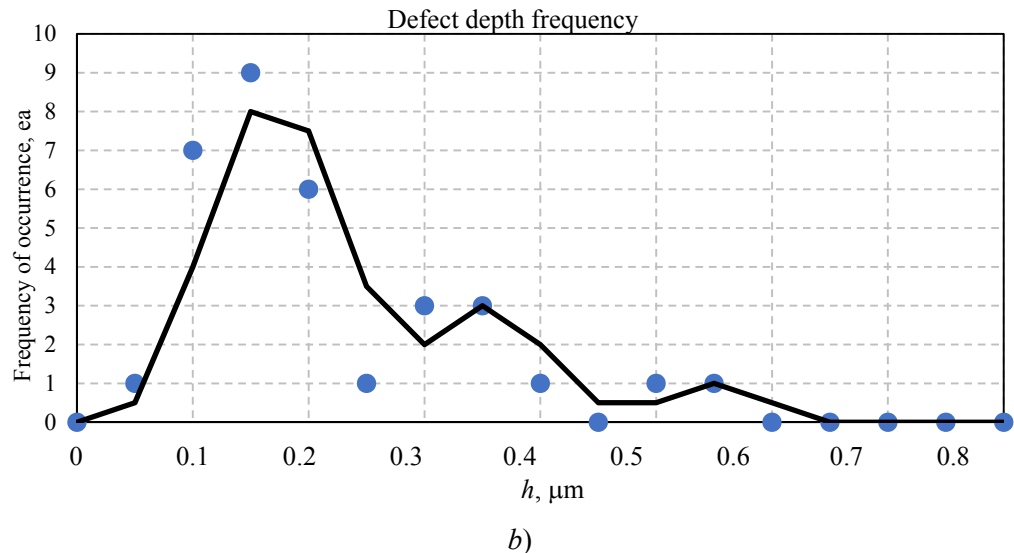


Fig. 2. Frequency of defect occurrence vs. diameter and depth



Fig. 3. Defect surface profil

In the center, the defect is often shaped as a rosette (Fig. 4). The atomic fraction of silicon in the defect reaches 65–68% (in SiO_2 – 47%), the atomic fraction of oxygen is 19–35% (in SiO_2 – 53%), and that of phosphorus is 0.7%. The accuracy of determining the concentration of elements ranged from 5 to 20% of the given values for different elements and samples (Table 1).

3. The distribution of defects over the plate area is random, regardless of the source of diffusant (POCl₃ or AMP) used and layout of plates in the reactor: vertical or horizontal relative to the gas flow.

4. The density of defects depends on the quality and thickness of the protective dielectric film: the film of the same sample is thinner over a thicker (field) oxide formed in the *n*-region than over an oxide grown in the p^{+} -region pre-doped as a result of boron diffusion. Boron diffusion did not result in the formation of defects in the field oxide. Decrease of the phosphorus concentration (increase of surface resistance Rs) leads to decrease of the defects density (for example, when the process temperature drops) (Table. 2).

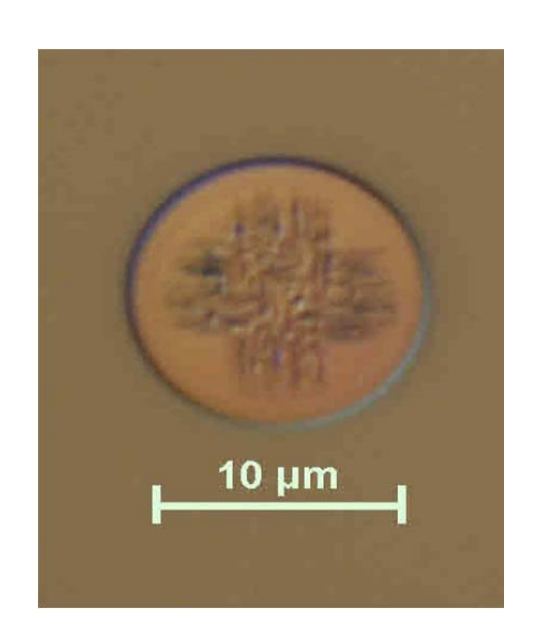


Fig. 4. Optical view of the "rosette" defect in the central area

Table 1

Content of elements in the solid phase (Net Int. – Total intensity of the peak corresponding to the element, minus the background)

| Element | Weight % | Atomic % | Net Int. | Error % |
|---------|----------|----------|----------|---------|
| СК | 5.8 | 11.6 | 15.1 | 12.0 |
| ОК | 13.1 | 19.5 | 197.2 | 10.5 |
| Si K | 80.2 | 68.2 | 15980.8 | 4.5 |
| PΚ | 0.9 | 0.7 | 39.4 | 11.3 |

Table 2

POCl₂

| Temperature, °C | 900 | 970 | 1000 | 1050 | | |
|--|-------|------|------|------|--|--|
| Defect density | 8.1 | 13.8 | 13.0 | 46.6 | | |
| $D < 10 \; \mu \text{m}, \; \text{mm}^{-2}$ | | | | | | |
| Defect density | 2.0 | 2.5 | 3.0 | 8.9 | | |
| $D=10-40 \ \mu \text{m}, \ \text{mm}^{-2}$ | | | | | | |
| Defect density | 0.4 | 0.5 | 0.7 | 0.7 | | |
| <i>D</i> > 40 μm, mm ⁻² | | | | | | |
| Average value of surface resistance, Rs, Ω/\Box | 157.4 | 24.5 | 12.4 | 4.5 | | |
| | | | | | | |

POCl₃

POCl₃

Defect density vs. surface resistance (Rs) and diffusion temperature

5. Heat treatment in the reactor in the absence of a diffusant does not lead to defects. Consequently, formation of defects has nothing to do with particles entering the samples from the reactor walls or from the carrier gas flow (N_2, O_2) .

Diffusant source

4. Discussion

Mechanism of microdefect formation [7] can be local melt-through of the oxide layer by liquid phosphorus-silicate glass (PSG) at the diffusion temperature. When the PSG layer solidifies during cooling of the samples, local areas with the increased concentration of phosphorus (P₂O₅) may form, their solidification temperature being lower than in the rest of the PSG layer. Such liquid drop dissolves phosphorus and other impurities when cooled, which reduces its solidification temperature. Liquid phase regions that diffuse into the SiO₂ layer are formed, which results in pits of various depths determined by the defect radius (liquid phase amount) (see Fig. 1). When the pit depth exceeds the oxide thickness, the liquid glass interacts with silicon to form a siliconand phosphorus-rich crystalline phase at the pit bottom (see Fig. 3, 4 and Table 1).

Formation of the crystalline phase while a through defect is developing may be related to the devitrification of amorphous SiO₂ under the influence of liquid phosphorsilicate glass acting as a mineralizer, with the siliconrich phase formed. Local melting of the oxide can be accelerated by defective areas formed in it during growth [1].

AMP

As can be seen on the curve in Fig. 1, defects larger than 10 µm in diameter have a depth more than 0.4 µm, which results in a through hole in the oxide of the specified thickness and interaction with silicon to form n^{+} -channels and a rosette-shaped solid phase. Smaller defects do not reach the silicon surface and cannot be a reason for impaired current-voltage characteristics. The curve shows that the more the oxide thickness, the weaker the influence of larger diameter defects on the current-voltage characteristics is. Thus, when the oxide thickness is $0.6 \mu m$, defects with a diameter of about 20 µm are not through.

Maxima occurring in the size distributions of pit diameters and depths (see Fig. 2) may be caused by the curve of the density of liquid phase nucleation centers vs. substrate temperature, which has a maximum at a certain value of liquid vapor supersaturation [5, 6]. Since the diffusion

process was completed by slow cooling of the samples in the furnace, there is a temperature range where the maximum number of centers form. The radius of the arising particles of the new phase is determined by the supersaturation value [5]:

$$R = \frac{2\sigma v}{RT \ln \frac{p}{p_0}},$$

where σ is surface tension at the liquid-vapor interface, v is molar volume of the liquid, $\ln p/p_0$ is supersaturation value, p, p_0 are vapor pressure over the drop and equilibrium pressure value.

Since decrease in the phosphorus concentration in PSG should reduce the probability of local areas with the increased concentration of P_2O_5 , decrease of the surface resistance as the diffusion temperature grows leads to the increase of defect diameter (see Table 2) and depth, thus impairing the current-voltage characteristics of the p-n junctions. It should be considered that the surface resistance shall not exceed $150 \ \Omega/\Box$ to ensure low contact resistance.

Conclusions

1. The influence of diffusion of phosphorus from a liquid source (POCl3) and a solid source (aluminum metaphosphate (AMP)) on the formation of local defects in SiO₂ layers and on the silicon surface has been analyzed.

- 2. The probable cause of defect formation has been established to be local melt-through of the oxide layer by liquid phosphorus-silicate glass due to a silicon-rich solid phase formed.
- 3. The defect depth is proportional to its diameter and decreases as the process temperature drops and the oxide thickness increases, which reduces the probability of n^+ channels in silicon.
- 4. The defect density is higher on the oxide built up on the boron-doped p^+ -regions.

REFERENCES

- 1. Blackstone S., Henry W., Jastrzebski L. and Fisher A. W., Journal of Electrochemical Society **3**, 667–668 (1982).
- 2. Storch W., Mohr U., Elstner L. and Leihkauf R., Phys. Stat. sol.(a) **132**, K109 (1992).
- 3. Miyashita M., Fukui H., Kubota A., Samata S., Hiratsuca H. and Matsushita Y. International Conference on Solid State Devices and Materials. Yocohama, 1991, pp. 568–570.
- 4. Pani S. K., Hogan R. H., Pandurangan M., Zhang J. and Koesan P., J. Vac. Sci. Technol. B **35** (6), 061206-1/5 (2017).
- 5. Tairov Yu. M. and Tsvetkov V. F. Texnologiya poluprovodnikovy`x i die`lektricheskix materialov, Moscow, Vy`sshaya shkola, 1983.
- 6. Fizicheskaya ximiya silikatov / Ed Pashhenko A. A., Moscow, Vy`sshaya shkola, 1986.
- 7. Vil'dyaeva M. N., Makarova E. A., Klimanov E. A., Lyalikov A. V. and Malygin V. A., Applied Physics, № 5, 53 (2021).
- 8. Bare G., Madar R. and Bernard C., Journal of Electrochemical Society **138** (9), 2830–2835 (1991).

About authors

Konstantin Olegovich Boltar, Head of Scientific and Technical Complex, Doctor of Physics and Mathematics, RD&P Center ORION, JSC (111538, Russia, Moscow, Kosinskaya Ulitsa, 9). Moscow Institute of Physics and Technology (National Research University) (141701, Russia, Moscow Region, Dolgoprudny, Institutsky Per., 9). E-mail: boltarko@yandex.ru SPIN code 9249-2720, Author ID 171355

Maria Nikolaevna Vildyaeva, Engineer Cat. 1, RD&P Center ORION, JSC (111538, Russia, Moscow, Kosinskaya Ulitsa, 9). E-mail: mari.vildyaeva@mail.ru

Nikita Alexandrovich Irodov, Head of the Area, RD&P Center ORION, JSC (111538, Russia, Moscow, Kosinskaya Ulitsa, 9). E-mail: irodov.mephi@yandex.ru SPIN code 8864-8834, Author ID 777457

Evgeniy Alekseevich Klimanov, Senior Research Assistant, Professor, Doctor of Technical Sciences, RD&P Center ORION, JSC (111538, Russia, Moscow, Kosinskaya Ulitsa, 9). MIREA – Russian Technological University (RTU MIREA) (119454, Russia, Moscow, Prospekt Vernadskogo, 78). E-mail: klimanov3@mail.ru SPIN code 7697-4688, Author ID 171375

Alexey Vladimirovich Lyalikov, Leading Engineer, RD&P Center ORION, JSC (111538, Russia, Moscow, Kosinskaya Ulitsa, 9).

Vladislav Anatolievich Malygin, Engineer, RD&P Center ORION, JSC (111538, Russia, Moscow, Kosinskaya Ulitsa, 9). E-mail: mva1431@yandex.ru SPIN code 9416-8272, Author ID 1240051

Dmitry Sergeevich Molchanov, Engineer, RD&P Center ORION, JSC (111538, Russia, Moscow, Kosinskaya Ulitsa, 9).

Elina Alekseevna Makarova, Engineer Cat. 2, RD&P Center ORION, JSC (111538, Russia, Moscow, Kosinskaya Ulitsa, 9).

PHOTOELECTRONICS =

UDC 535 PACS: 81.15.Hi

EDN: UPMEMZ

Study of optical properties of CdTe/GaAs(100) epitaxial films grown in different temperature conditions

© A. A. Grekova^{1,2,*}, E. A. Klimov¹, A. N. Vinichenko^{1,2}, I. D. Burlakov¹

¹ RD&P Center ORION, JSC, Moscow, 111538 Russia * E-mail: ingo.tyan2@mail.ru ² National Research Nuclear University MEPhI, Moscow, 115409 Russia Received 03.03.2025; revised 20.03.2025; accepted 07.04.2025 Scientific specialty code: 1.3.11

The influence of the growth temperature of cadmium telluride epitaxial films grown by molecular beam epitaxy on semi-insulating GaAs(100) substrates on the optical and structural properties of CdTe was investigated. The spectra of ellipsometric parameters Ψ and Δ were determined by the spectroscopic ellipsometry. The study revealed that the Van Hove singularities E_1 and E_0 corresponding to 3.3 and 1.46 eV are the distinctive features of the CdTe compound. Surface roughness, resulting from non-optimal substrate temperatures, was identified as the primary factor increasing the oscillation amplitude $\Psi(\lambda)$ in the transparent spectral region ($E < E_g$). A correlation between ellipsometric parameters Ψ and Δ and RMS roughness R_q of the film surface was established. The non-optimal temperature was found to result in development of surface morphology and reduction of range $\Delta(\lambda)$. Thus, the average value $\Delta(\lambda)$ is an indirect criterion for evaluating the surface morphology of CdTe epitaxial films. The range of optimal growth temperatures for CdTe epitaxial structures to achieve the minimum surface roughness was determined. The obtained data will be useful for growing CdHgTe on GaAs(100) substrate using CdTe buffer layers.

Keywords: CdTe, spectral ellipsometry, molecular beam epitaxy.

DOI: 10.51368/1996-0948-2025-2-46-54

Introduction

The advancement of optoelectronics requires the materials capable of absorbing long-wave radiation. For this reason compounds of the A₂B₆ chemical group, including ZnTe, CdTe, HgTe, CdHgTe, are

widely used as base materials in various photodetectors [1, 2]. These compouds were selected among many other semiconductor structures based on the data obtained from strategic objects in the IR wavelength range of $1-12~\mu m$. However, mechanical stresses in the crystal lattice of these materials result –

cause scattering of electromagnetic radiation. As a result, the obtained images become blurred and difficult to analyze.

In turn, the structural quality of the resulting A₂B₆-compounds, like that of other materials, is directly dependent on their synthesis method. One of the main modern methods for producing single-crystal semiconductor compounds is molecular beam epitaxy (MBE) [3–6]. The main advantage of this method is its precise control over parameters that affect growth mechanisms. Such parameters are the temperature of the substrate and molecular sources. These parameters critically affect the growth rate of compounds and the crystalline quality of epitaxial films. Non-optimal selection of parameters leads either to polycrystalline structure formation of A₂B₆compounds or in numerous defects within the material bulk [7]. Low growth temperatures of A₂B₆-compounds decrease the binding energy between Cd, Te, Hg and Zn atoms, which potentially causing amorphous phase formation on the growing film surface [4, 8– 10]. Conversely, exceeding the optimal epitaxial growth temperatures can lead to the accumulation of non-stoichiometric tellurium inclusions throughout the film volume [11]. The substrate material and orientation critically affects important role in the epitaxy of A₂B₆-compounds. A significant lattice mismatch between the substrate and the deposited material promotes the formation of structural defects in the grown material. In the case of A₂B₆-compounds, the most thermodynamically favorable substrate is Cd_{0.96}Zn_{0.04}Te. The mole fraction of zinc variation enables tuning the lattice parameter of Cd_{1-x}Zn_xTe, thereby reducing the mismatch with Cd_xHg_{1-x}Te [12]. However, high-quality Cd_xHg_{1-x}Te-based substrates are prohibitively expensive and limited in size, so GaAs is used as an alternative [13]. Despite the high mismatch between Cd_xHg_{1-x}Te and GaAs (about 20 %). Successful epitaxial growth is

achieved through the implementation of CdTe, ZnTe buffer layers [1, 3, 7, 13, 14]. These buffer layers, preserve the substrate orientation and prevent defect propagation into the upper layers [3, 14, 15]. Importantly, the infrared absorption characteristics depend not only on the CMT active region quality, but also on the structural perfection of both the substrate and buffer layers. Therefore, optoelectronic performance of devices depends not only on the active region of Cd_xHg_{1-x}Te structures, but also on the crystalline quality of the entire heterostructure system [12, 16].

The crystalline quality of samples is evaluated through comprehensive analysis of these structural and optical characteristics, which directly correlate with the epitaxial growth conditions. They are directly related to the conditions of epitaxial growth of the layers under study [16]. Therefore, to develop the technology for production A₂B₆-compounds of molecular beam epitaxy, many different methods are required for post-growth analysis resulting samples. Key parameters including surface roughness and optical spectra characteristics are crucial optimizing growth conditions. In this study, the optical ellipsometry (OE) and atomic force microscopy (AFM) were employed to characterize optical and structural parameters. Ellipsometric measurements provided the spectra of $\Psi(\lambda)$ and $\Delta(\lambda)$ parameters [17]. The ellipsometric parameters Ψ and Δ components of the elliptical represent polarization of the beam reflected from the surface. These parameters provide information the roughness on and composition of sample compounds [18]. Optical ellipsometry is a rapid method for analyzing optical and structural characteristics of the grown films. Based on the data obtained by combination of OE and AFM, optimal growth temperatures for A₂B₆ based films can be determined.

The goal of this study is to determine the dependence of ellipsometric parameters $\Psi(\lambda)$ and $\Delta(\lambda)$ in epitaxial CdTe films on different temperatures of growth conditions by the optical ellipsometry ns using optical ellipsometry. Additionally, we seek determine the range of optimal growth temperatures to achieve minimum surface roughness of samples. The results of this work will be useful for determining the optimal temperature conditions for epitaxial growth of A₂B₆-compounds, and enable in situ monitoring of molecular beam epitaxy for $Cd_xHg_{1-x}Te$ layers on various substrates.

Experiment procedure

CdTe films (samples Nos. 5, 8, 15, and 18) were grown by molecular beam epitaxy in Riber Epineat Cluster ultra-high vacuum multi-chamber setup We used semi-insulating epi-ready GaAs(100) substrates and a binary CdTe source. The temperature was controlled using a thermocouple integrated in the sample heater. Molecular flows were measured with a

Bayard-Alpert sensor. Pre-growth treatment of the GaAs substrate included two stages. First, the sample holder with the substrate was degassed to remove volatile compounds and water vapour in the pre-treatment chamber at the temperature of 350 °C for 20 minutes. Secondly, in the growth reactor for A₃B₅ group materials, natural oxides were desorbed in the arsenic flow temperature of 680 °C for 5 minutes. followed by growth of the GaAs buffer layer of 0.5 µm in thickness. Then, to perform the epitaxial synthesis of CdTe films, the holder with the substrate was placed in the growth chamber for A₃B₅ group materials. CdTe structures were grown substrate at temperatures of 250, 325, 400 and 450 °C.

After epitaxial growth and ellipsometric measurements of CdTe films, the CdTe/GaAs(100) samples were unloaded from the MBE setup and measured by the atomic force microscopy method using NT-MTD Ntegra Maximus microscope in contact mode in the $10\times10~\mu m$ field. The average roughness (R_q) values of the samples are given in Table 1.

Table 1 Energy values and wavelengths corresponding to critical points E_1 and E_0 depending on the substrate temperature

| Sample number | Substrate temperature, °C | R_q , nm | Thickness, | λ, nm | E_1 , eV | λ, nm | E_g , eV |
|---------------|---------------------------|------------|------------|-------|------------|-------|------------|
| 8 | 250 | 17.00 | 4058 | 365 | 3.39 | 846 | 1.46 |
| 9 | 325 | 4.90 | 4256 | 376 | 3.30 | 842 | 1.47 |
| 18 | 400 | 0.85 | 4071 | 372 | 3.33 | 846 | 1.46 |
| 15 | 450 | 1.17 | 1452 | 373 | 3.34 | 893 | 1.39 |

SEC-1000 spectral ellipsometric complex (Russia, Novosibirsk, Institute of Semiconductor Physics of the Russian Academy of Science) was used as analytical equipment for obtaining ellipsometric spectra $\Psi(\lambda)$ $\Delta(\lambda)$ in the wavelength range of

350÷1000 nm (from 1.2 to 3.5 eV) [17]. The angle of incidence of linearly-polarized light on the sample under study was 70°. The highly stable OSRAM halogen lamp was used as a radiation source. Instrumentation errors in measurement of the refractive index

and thickness are 0.005 and 5 Å, respectively. Spectr software was used to analyze the ellipsometric spectra $\Psi(\lambda) \Delta(\lambda)$.

Discussion of the results

Different crystal structures exhibit distinct electronic properties, characterized by critical points (Van Hove singularities) in their band structure. These singularities manifest as maxima in the dielectric function spectra $[\epsilon_1(\lambda)$ and $\epsilon_2(\lambda)]$ or as features in the electronic band structure [19–21]. Lattice strains induced by defects (e.g., impurities, dislocations, vacancies) significantly alter the spectral positions and amplitudes of these critical points.

The structural quality of layers growing by the molecular beam epitaxy is directly on growth conditions. dependent the including temperatures of the substrate and molecular sources. A₂B₆-compound such as CdTe exhibit a low binding energy of about 572.6 eV, which for reason growth temperatures above 500 °C may be too high for the single crystal to grow [10]. Although CdTe films deposit on GaAs substrates below 200 °C, the growth mode transitions to 3D islanding [16], yielding polycrystalline films. This occurs due to insufficient kinetic energy for complete adatom dissociation and surface diffusion to stable lattice sites [22].

Substrate surface preparation is critical for growing high-quality CdTe epitaxial layers. Thermal decomposition of amorphous oxide layers with GaAs at temperatures above 700 °C is the main method of pre-growth treatment. High temperature causes the Ga-O and Ga-As bonds to break, facilitating while exposing oxygen, arsenic clean gallium-terminated surfaces. If thermal insufficient, near-surface impact is the oxygen or other near-surface defects can transite the orientation of growing CdTe from (100) to (111) [10, 23–26].

The in-situ optical research method such as ellipsometry can be found useful for describing the structure properties. This method measures two parameters, such as Ψ and Δ , corresponding to the ratio of amplitudes and phase difference of two components of the reflected ellipticallypolarized wave. Their values are directly dependent on the optical characteristics of the material, such as the refractive index and absorption coefficient. The spectrum of imaginary permittivity is often used to analyze crystal features. However, parameter Δ taken into account in this calculation can affect the qualitative identification of Van Hove singularities due to sensitivity to the film roughness [18], so it is advisable to analyze the spectra Ψ [19]. Here the dependence $\Psi(\lambda)$ was used to determine the structural features of epitaxial films of cadmium telluride. The spectrum $\Delta(\lambda)$ describing the development of the sample surface morphology was compared to the findings of atomic force microscopy.

The study examined four epitaxial CdTe films (samples No. 8, 9, 15, and 18) grown directly on semi-insulating GaAs(100) substrates. The growth temperatures varied between 250 °C and 450 °C, while the film thickness differed among samples (see Table 1). All other growth parameters and substrate pretreatment conditions were kept identical.

The wavelength range from 350 nm to approximately 850 nm ($E > E_g$) is particularly important for optical characterization, as this spectral region the film absorbs incident radiation, and Van Hove singularities in the spectrum $\Psi(\lambda)$ will be observed. Figure 1 shows the ellipsometric spectra of parameter Ψ for CdTe samples Nos. 8, 9, 15 and 18, and results of determining the energy position of

the critical points are given in Table 1. Van Hove singularity equaling E_1 to approximately 3.3 eV can be observed in each spectrum and is in good agreement with the literature data [27]. Comparison of spectra $\Psi(\lambda)$ revealed that the growth temperature in significantly this influences singularity's linewidth. Specifically, CdTe layers grown at 450 °C exhibit a narrower E₁ feature compared to samples prepared at temperatures. The reason is lower

additional absorption of incident radiation caused by defects found in samples Nos. 8, 9 and 18 near critical point E_1 . Structural imperfections generated during CdTe growth at suboptimal temperatures (250–325 °C) likely contribute to this additional absorption. AFM measurements confirm that growth at 400 °C (sample No. 15) yields the smoothest surface, with the lowest root-mean-square roughness R_q (Table 1).

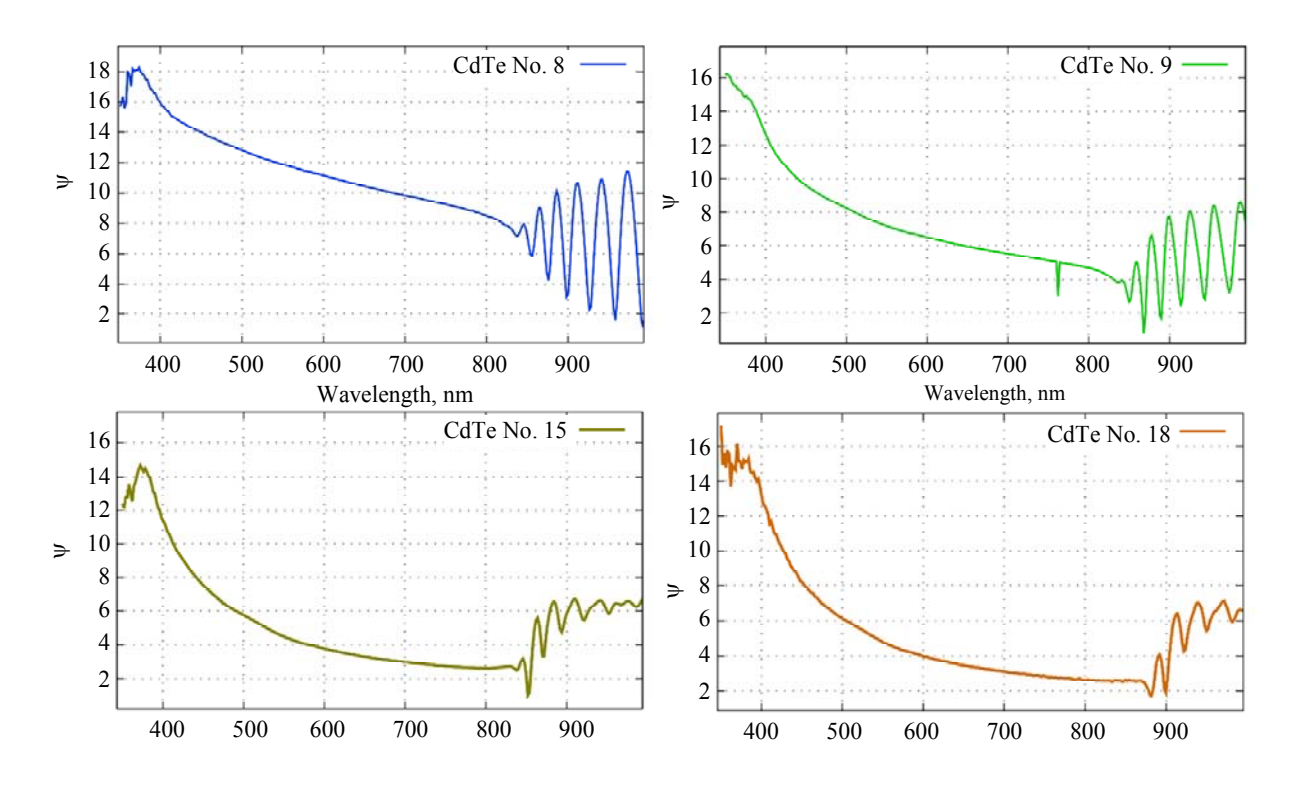


Fig. 1. Ellipsometric spectra of parameter ψ of CdTe/GaAs. Blue line – CdTe No. 8 (upper left corner); green line – CdTe No.9 (upper right corner); dark green line – CdTe No. 15 (lower left corner); orange line – CdTe No.18 (lower right corner)

The band gap is also directly dependent on characteristics of the crystal structure. In ellipsometric spectrum $\Psi(\lambda)$, the critical point corresponding to E_g of CdTe is the first minimum before the start of interference oscillations in the CdTe film. According to the values of Table 1, E_g corresponds to the literature data in the case of samples Nos. 8, 9

and 18 [27]. Large thickness of samples of about 4 μ m reduces to zero the probability of formation of interference oscillations in region $E > E_g$ due to the excessive depth of light penetration into the sample. For this reason no extremes are observed in this energy range $(E > E_g)$ in the spectra $\Psi(\lambda)$, and the band gap width is determined most

accurately. In the case of sample No. 15, which is about 1.5 μ m in thickness, the mismatch of E_g and literature data is due to incomplete absorption of incident radiation in this spectrum region and, consequently, the influence of interference observed in the film.

The oscillations observed in spectrum $\Psi(\lambda)$ shown in Figure 1 within wavelength range from approximately 850 to 1000 nm ($E < E_{\sigma}$) correspond to interference in the grown CdTe films [28]. Comparison of the dependencies under study has revealed that sample No. 8 has the highest oscillation amplitude, while decrease in the amplitude of these oscillations in other samples indicates a high absorption rate in CdTe films [28]. Figure 2 shows the ellipsometric spectra $\Delta(\lambda)$ for CdTe/GaAs(100) samples Nos. 8, 9, 15, 18. The above parameter is the phase difference of components of the ellipticallypolarized radiation reflected from the film surface, and therefore it is used to analyze the roughness of grown structures.

According to the data obtained by the atomic force microscopy method (see Table 1), sample No. 8 has the most developed morphology ($R_q = 17$ nm), which is consistent with the OE findings $\Delta(\lambda)$, since the average value Δ (70°) differs from the optimal one (140-150°) in the spectral region of 350-850 nm [29]. The low value of parameter Δ corresponds to the developed morphology of the film surface; the average value of parameter Δ for samples Nos. 15 and 18 was within the acceptable limits: 145°±5°. Thus, the data obtained by the spectral ellipsometry method indicate the low value of the RMS surface roughness of samples Nos. 15 and 18, which was confirmed by the atomic force microscopy method (see Table 1).

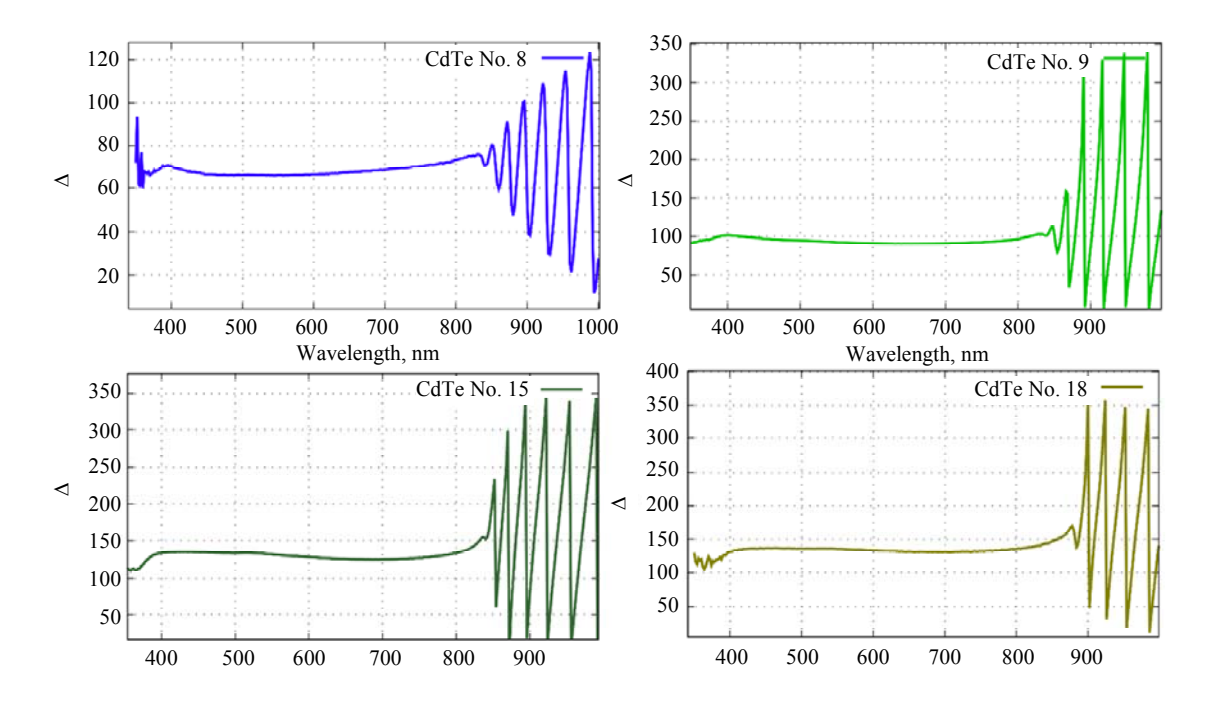


Fig. 2. Ellipsometric spectra of parameter △ of CdTe/GaAs samples. Blue line – sample 8; light green line – sample 9; dark green line – sample 15; brown line – sample 18

Conclusion

This research analyzed the ellipsometric spectra of parameters Ψ , Δ as a function of the growth temperature of CdTe films. A correlation between ellipsometric parameters Ψ and Δ and RMS roughness R_q of the film surface was established. Comparison of the dependencies $\Psi(\lambda)$ revealed that CdTe/GaAs(100) samples Nos. 15 and 18 synthesized at temperatures of 450 °C and 400 °C, respectively, scatter the optical radiation less than the others. This indicates a lower defect density in these films. Analysis of spectrum $\Delta(\lambda)$ allowed to establish that since the parameter Δ values for samples Nos. 15 and 18 were within the range of 145°±5°, the surface roughness of their CdTe films should be the lowest as compared to the other samples. The CdTe/GaAs(100) film No. 8 developed surface morphology confirmed by the atomic force microscopy measurements $(R_q = 17 \text{ nm})$ and could be observed in spectrum $\Delta(\lambda)$ ($\overline{\Delta} = 70^{\circ}$). Thus, the optimal temperature range for epitaxial growth of CdTe films is 400–450 °C, as this minimizes formation of surface morphology on the film surface. The critical point E_1 (3.3 eV), corresponding to the CdTe compound, manifests as a maximum in the $\Psi(\lambda)$ spectrum for light energies $E > E_g$. The halfwidth of this extremum provides a qualitative measure of defect formation in the growing CdTe structure. The findings of this work will be useful as the express method determining the crystal structure features of A₂B₆-compounds and monitoring the growth of CdTe, epitaxial ZnTe, and CdHgTe.

The authors are thankful to A. S. Sukhanova, engineer cat.2 of RD&P Center ORION, JSC, for the AFM measurements completed.

REFERENCES

- 1. Pan W. W., Gu R. J., Zhang Z. K., Lei W., Umana-Membreno G. A., Smith D. J., Antoszewski J. and Faraone L., J. Electron. Mater. **51**, 4869–4883 (2022). https://doi.org/10.1007/s11664-022-09725-1
- 2. Scarpulla M. A., McCandless B., Yan Y., Heben M. J., Phillips A. B., Wolden C., Metzger W. K., Xiong G., Mao D., Krasikov D., Sankin I., Grover S., Munshi A., Sampath W., Sites J. R., Bothwell A., Albin D., Reese M. O., Klie R., Romeo A., Nardone M., Walls M., Fiducia T., Abbas A. and Hayes S. M., Solar Energy Materials and Solar Cells. 255, 112289 (2023). https://doi.org/10.1016/j.solmat.2023.112289
- 3. Dvoretsky S. A., Mikhailov N. N., Remesnik V. G., Sidorov Y. G., Shvets V. A., Ikusov D. G., Varavin V. S., Yakushev M. V., Gumenjuk-Sichevska J. V., Golenkov A. G., Lysiuk I. O., Tsybrii Z. F., Shevchik-Shekera A. V., Sizov F. F., Latyshev A. V. and Aseev A. L., Opto-Electronics Review 27, 282–290 (2019). https://doi.org/10.1016/j.opelre.2019.07.002
- 4. Varavin V. S., Dvoretskii S. A., Mikhailov N. N., Remesnik V. G., Sabinina I. V., Sidorov Yu. G., Shvets V. A., Yakushev M. V. and Latyshev A. V., Optoelectron. Instrument. Proc. **56**, 456–469 (2020).

https://doi.org/10.3103/S8756699020050143

- 5. Vogt A., Shutt S., Frei K. and Fiederle M., Journal of Crystal Growth. **477**, 114–117 (2017). https://doi.org/10.1016/j.jcrysgro.2017.02.048
- 6. Sidorov Yu. G., Dvoretsky S. A., Varavin V. S., Mikhailov N. N., Yakushev M. V. and Sabinina I. V., Semiconductors **35** (9), 1045–1053 (2001).
- 7. Wichrowska K., Wosinski T., Domagala J. Z., Kret S., Chusnutdinow S. and Karczewski G., Semicond. Sci. Technol. **36** (4), 045022 (2021).

https://doi.org/10.1088/1361-6641/abbd0d

8. Ahmed T., Tan X., Li B. Y., Cook E., Williams J., Tiano S. M., Coffey B., Tenney S. M., Hayes D. and Caram J. R., ACS Nano. **19** (3), 3944–3952 (2025).

https://doi.org/10.1021/acsnano.4c17596

9. Kozlov D. V., Rumyantsev V. V., Kadykov A. M., Fadeev M. A., Kulikov N. S., Utochkin V. V., Mikhailov N. N., Dvoretskii S. A., Gavrilenko V. I., Hubers H. W., Teppe F. and Morozov S. V., JETP Letters **109** (10), 657–662 (2019).

- 10. Feldman R. D., Austin R. F., Kisker D. W., Jeffers K. S. and Bridenbaugh P. M., Appl. Phys. Lett. **48**, 248–250 (1986). https://doi.org/10.1063/1.96571
- 11. Sidorov Y. G., Dvoretskii S. A., Varavin V. S., Mikhailov N. N., Yakushev M. V. and Sabinina I. V., Semiconductors **35**, 1045–1053 (2001). https://doi.org/10.1134/1.1403569
- 12. Varavin V. S., Dvoretskii S. A., Mikhailov N. N., Remesnik V. G., Sabinina I. V., Sidorov Yu. G., Shvets V. A., Yakushev M. V. and Latyshev A. V., Optoelectronics, Instrumentation and Data Processing. **56**, 456–469 (2021). https://doi.org/10.3103/S8756699020050143
- 13. Tyagi S., Goyal A., Rana S. S., Meena U. R., Mishra P., Pandey R. K., Dalal S., Pandey A., Garg A. K., Kumar S. and Singh R., J Mater Sci: Mater Electron. **35**, 982 (2024). https://doi.org/10.1007/s10854-024-12724-z
- 14. Svitashev K. K., Dvoretsky S. A., Sidorov Yu. G., Shvets V. A., Mardezhov A. S., Nis I. E., Varavin V. S., Liberman V. and Remesnik V. G., Crystal Research and Technology **29** (7), 931–937 (1994). https://doi.org/10.1002/crat.2170290703
- 15. Bratina G., Sorba L., Antonini A., Ceccone G., Nicolini R., Biasiol G., Franciosi A., Angelo J. E. and Gerberich W. W., Phys. Rev. B **48**, 8899 (1993).
- https://link.aps.org/doi/10.1103/PhysRevB.48.8899
- 16. Hwang Y., Ngugen V. Q., Choi J. S., Park S., Cho S., Kim T. H., Ha Y. and Ahn C. W., J. Korean Phys. Soc. **79**, 1057–1062 (2021). https://doi.org/10.1007/s40042-021-00337-2
- 17. Shvets V. A., Spesivtsev E. V., Rykhlitskii S. V. and Mikhailov N. N., Nanotechnol Russia **4**, 201–204 (2009).
- https://doi.org/10.1134/S1995078009030082

- 18. Shvets V. A., Marin D. V., Kuznetsova L. S., Azarov I. A., Yakushev M. V. and Rykhlitskii S. V., Journal of Optical Technology **91** (7), 496–501 (2024). https://doi.org/10.1364/jot.91.000091
- 19. Shvets V. A., Azarov I. A., Marin D. V., Yakushev M. V. and Rykhlitskii S. V., Semiconductors **53**, 132–137 (2019).
- 20. Moss T., Barrel G. and E`llis B. Poluprovodnikovaya optoe`lektronika. Moscow, Mir, 1976.
- 21. Shalimova K. V. Fizika poluprovodnikov. Mowcow, Energoatomizdat, 1985.
- 22. Yin J., Huang Q. and Zhou J., J. Appl. Phys. **79**, 3714–3717 (1996). https://doi.org/10.1063/1.361204
- 23. Mcgibbon A. J., Pennycook S. J. and Angelo J. E., Science **269** (5223), 519–521 (1995). https://doi.org/10.1126/science.269.5223.519
- 24. Kolodziejski L. A., Gunshor R. L., Otsuka N. and Choi C., J. vac. Sci. Technol. A **4**, 2150–2152 (1986). https://doi.org/10.1116/1.574045
- 25. Faurie J. P., Hsu C., Sivananthan S. and Chu X., Surface Science **168** (1-3), 473–482 (1986). https://doi.org/10.1116/1.574045
- 26. Zhang S., Zhang J., Qiu X., Wu Y. and Chen P., Journal of Crystal Growth. **546**, 125756 (2020). https://doi.org/10.1016/j.jcrysgro.2020.125756
- 27. Adachi S., Kimura T. and Suzuki N., J. Appl. Phys. **74**, 3435 (1993). https://doi.org/10.1063/1.354543
- 28. Shvets V. A., Marin D. V., Yakushev M. V. and Rykhlitskii S. V., Semiconductors **57** (6), 464–469 (2023).
- 29. Shvets V. A., Marin D. V., Yakushev M. V. and Rykhlitskii S. V., Semiconductors **58**, 67–72 (2024). https://doi.org/10.1134/S1063782624010147

About authors

Anastasia Alexandrovna Grekova, Process Engineer Cat. 2, RD&P Center ORION, JSC (111538, Russia, Moscow, Kosinskaya Ulitsa, 9). National Research Nuclear University MEPhI (115409, Russia, Moscow, Kashirskoye Shosse, 31). E-mail: ingo.tyan2@mail.ru

Evgeniy Alexandrovich Klimov, Head of Area, Candidate of Physics and Mathematics, RD&P Center ORION, JSC (111538, Russia, Moscow, Kosinskaya Ulitsa, 9). E-mail: klimov_evgenyi@mail.ru SPIN code 7826-3235, Author ID 153920

Alexander Nikolaevich Vinichenko, Leading Engineer of Area, Candidate of Physics and Mathematics, RD&P Center ORION, JSC (111538, Russia, Moscow, Kosinskaya Ulitsa, 9). National Research Nuclear University MEPhI (115409, Russia, Moscow, Kashirskoye Shosse, 31). E-mail: ANVinichenko@mephi.ru SPIN code 6466-4907, Author ID 725517

Igor Dmitrievich Burlakov, Deputy Director General for Innovations and Science, Doctor of Technical Sciences, Professor, RD&P Center ORION, JSC (111538, Russia, Moscow, Kosinskaya Ulitsa, 9). E-mail: idbur@orion-ir.ru SPIN code 6042-3634, Author ID 171368

PLASMA PHYSICS AND PLASMA METHODS

UDC 533.9; 534-16 PACS: 52.75Fk; 41.75Fr; EDN: VGCLXD 41.75Ht; 62.50Ef

Evaluation of the influence of plasma processes in the vacuum diode of Kalmar high-current electron accelerator on the development of shock-wave processes in targets

© E. D. Kazakov^{1,2,3,4,*}, M. Yu. Orlov¹, A. R. Smirnova^{1,3,4}, M. G. Strizhakov¹, K. A. Sunchugashev¹,L. M. Yusupova^{1,2}, S. I. Tkachenko^{1,3,4,5}

¹ National Research Center Kurchatov Institute, Moscow, 123182 Russia

*E-mail: kazakov_ed@nrcki.ru

² MPEI National Research Institute, Moscow, 111250 Russia

³ Moscow Institute of Physics and Technology (National Research University),

Dolgoprudny, Moscow Region, 141701 Russia

⁴ Keldysh Institute of Applied Mathematics of the Russian Academy of Science,

Moscow, 125047 Russia

⁵ Joint Institute for High Temperatures of the Russian Academy of Sciences,

Moscow, 125412

Received 11.11.2024; revised 13.01.2025; accepted 14.02.2025 Scientific specialty code: 1.3.9

The influence of diode plasma on the formation and propagation of compression and shock waves inside targets is considered as part of studying the impact of high-current electron beams on solid targets. Experimental studies were carried out on the Kalmar installation generating a high-current electron beam. For the purpose of evaluation, numerical modeling of processes occurring in the plasma-filled diode in terms of one-dimensional magnetohydrodynamics (MHD) was carried out. The modeling results confirm that plasma can provide the pressure sufficient to create the secondary compression waves observed during the experiment.

Keywords: diode plasma; high-current electron beam; transparent targets; shock-wave processes.

DOI: 10.51368/1996-0948-2025-2-55-61

Introduction

Studying the formation and propagation of shock waves inside various materials under powerful pulse impacts is of relevance, since the growing number of new composite and polymeric materials are finding use in aviation, rocket and space technology, shipbuilding and special applications [1]. Experimental research in this area has been conducted for over fifty years using various types of impact on samples [2–6]. The main instruments initiating the mechanical shock wave impact are ballistic and explosive

generators [7] and electroexplosive devices [8]. Along with them, high-power pulsed lasers, magnetic-pulse generators [9], as well as high-current electron and ion accelerators are actively used. This paper describes the features of shock-wave processes occurring in transparent materials impacted by a high-current electron beam generated by Kalmar installation (current up to 35 kA, diode voltage up to 350 kV, electron beam duration ≈ 100 ns).

Relatively high penetration power is among the specific features of such electron beams as a source of shock waves. Since the duration of beam action is about one hundred nanoseconds, the energy is released in the surface layer of not more than several hundred micrometers in thickness (up to 80 % of electrons are absorbed in the layer less than 100 microns thick), and the release time of such region is at least 500 ns, so the process of beam energy absorption can be considered isochoric. In most studies, various parameters the target surface are evaluated considering only the interaction of the electron beam with the target surface and release of the energy absorption region. However, after the electron beam has passed, plasma is formed in the diode gap [10], the influence of which is usually neglected. Some experimental results demonstrating dynamics of shock wave passing through the target [10, 11] give reason for considering the influence of diode plasma on the formation and propagation of shock waves inside the target in more details.

The issue of influence of diode plasma on the formation and propagation of compression and shock waves inside targets was brought up earlier during study of the impact of high-current electron beams on condensed targets. However, so far there are no findings that confirm or refute this. As a result of modeling the anode flame [12], quite extreme plasma parameters were obtained (average electron temperature $T_e \approx 10 \text{ eV}$, average concentration $n_e > 5 \times 10^{17} \text{ cm}^{-3}$). One-dimensional MHD modeling of the plasma column parameters that we undertook confirms the assumption that the plasma pressure can reach values sufficient to give rise to compression waves, which can be observed during experiments.

Experimental research

Experiments to study the influence of diode plasma on the formation and movement of shock and compression waves in transparent targets were carried out using Kalmar high-current accelerator [13]. Target samples made of various transparent materials were attached to the anode assembly plate. The residual pressure in the vacuum chamber was not more than 10^{-2} Pa.

The optical diagnostic system is based on probing the diode gap and/or target with laser radiation perpendicularly to the diode axis. Laser radiation passes via the diagnostic windows through the area under study. The image is transferred to the photocathode of SFER-6 electron-optical camera operating in streak image mode by means of the system of lenses and mirrors [9]. Since the typical durations of plasma and shock-wave processes differ by approximately an order of plasma processes magnitude, can identified quantitatively only on streak image It should be noted that plasma parameters in the anode region can take on values at which plasma cannot be identified with existing diagnostics.

Figure 1 shows the combined streak image recorded by the shadow photography method while simultaneously recording the plasma's own glow. One can see the shadow appearing against the background of the probing radiation in the upper part of the image. This shadow appears when the

refractive index changes as the compression or shock wave passes in a target attached to the rear surface of the anode plate. In the lower part of the image (below the time axis), the plasma's own glow in the accelerator diode can be observed. The probing radiation did not pass through the diode gap since it was blocked by the screen.

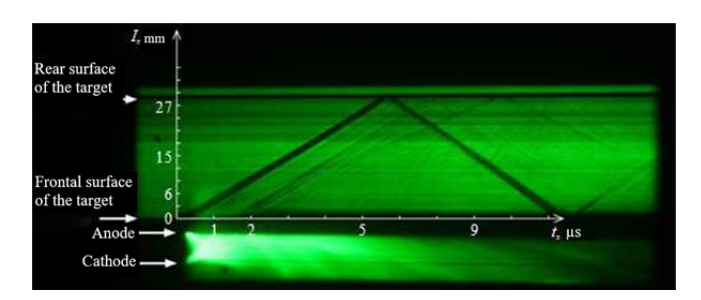


Fig. 1. The combined streak image recorded by the shadow photography method while simultaneously recording the plasma's own glow. The timeanalyzing slit is oriented along the beam axis. The energy of the electron beam in the shot was 450 J; the target was made of glass (LK-5)

As can be seen from streak image, during the first 300-400 ns a shock wave is formed, the propagation speed of which is ~5.4 km/s. One can see in the lower part of the streak image that, by the end of this time interval, the bright own glow spreading from the electrodes to the center covers the diode gap. It can be concluded that the radiating plasma fills up the diode gap. By the time equaling to 1.5-2 µs the plasma's own glow becomes less intense. After ~2 µs, multiple darkenings appear within the target volume, each may correspond to the propagation of in the compression waves material. Occurrence of these waves at the late stages of anode plasma expansion may be caused by the excessive pressure in the anode region arising in the plasma channel.

The current and voltage in the diode gap were measured using a shunt and a capacitive divider, respectively [14]. With the current and voltage known, one can determine the power and integral energy input by the beam

to the sample.

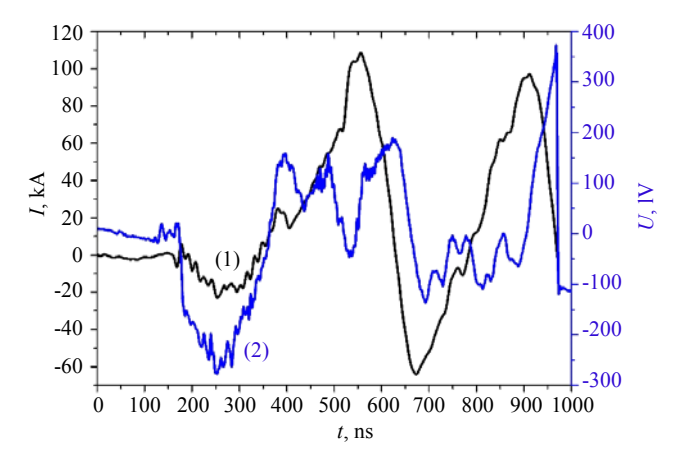


Fig. 2. The time dependences of the current (1) and voltage (2) measured at the diode gap

Figure 2 shows the characteristic time dependence of the electron beam current and conduction current through the The electron beam can be seen to be formed in the diode in the time interval from 150 ns to 350 ns; after which the diode gap is filled with plasma, which initiates the current reversal at ~400 ns. After the diode is closed by plasma, the alternating current can be observed, with its amplitude decreasing. The diode is closed due to its filling with plasma flows from the cathode and anode. Plasma appearing at the cathode is caused by the surface explosion (explosive emission), and the one appearing at the anode is caused by the interaction of a beam of high-energy electrons with the target surface. presence of current in the diode gap means that the plasma closing the diode has high conductivity.

Mathematical modeling

To determine the range of parameters at which diode plasma influences the generation of shock waves inside the target, a problem to model the processes occurring in the cylindrical plasma channel with current was

formulated. The plasma channel formation stage was not considered. This problem was solved in terms of one-dimensional (coordinate r is directed parallel to the target surface; the origin of coordinates is located at the point corresponding to the electron beam single-temperature axis) magnetohydrodynamics (MHD) in the cylindrical coordinate system. The system of MHD equations using Lanrange variables is written below:

$$\frac{dm}{dt} = 0,\tag{1}$$

$$\rho \frac{dv}{dt} = -\frac{\partial P}{\partial r} - \frac{1}{2\mu_0 r^2} \cdot \frac{\partial \left(r^2 B_{\phi}^2\right)}{\partial r},\tag{2}$$

$$\rho \frac{d\varepsilon}{dt} = -P \frac{\partial (rv)}{\partial r} + \frac{j^2}{\sigma}, \tag{3}$$

$$\frac{d\left(\mu B_{\varphi}\right)}{dt} = \frac{\partial}{\partial r} \left[\frac{1}{\sigma r} \cdot \frac{\partial \left(r B_{\varphi}\right)}{\partial r} \right],\tag{4}$$

 m_c is the carbon atom mass; v is the velocity; P is the flow pressure; μ is the permeability; $B_{\rm o}$ magnetic field induction; the $j = \frac{1}{\mu_0 r} \frac{\partial (rB_{\varphi})}{\partial r}$ is the current density; σ is the conductivity; T is the temperature; n is the concentration. describe To the thermodynamic properties of the medium, the plasma model and the Spitzer conductivity model were used. Initial and boundary conditions for the described problem were written using the results obtained from processing the experimental data: maximum plasma concentration at the initial moment was equal to $n_0 = 10^{17} \text{ cm}^{-3}$, initial radius of the cylindrical plasma column was equal to $r_0 = 1$ cm, initial plasma temperature was equal to $T_0 = 10 \text{ eV}$ induction at the outer magnetic field

where m is the mass; $\rho = m_c n$ is the density;

boundary of $(r_{\rm out})$ plasma channel $B_{\varphi}(r_{\text{out}},t) = \mu_0 I(t)/\{2\pi \quad r_{\text{out}}(t)\};$ the magnetic field and velocity field at the initial moment were set to zero. The model considered the singly-ionized plasma; the initial distribution of plasma concentration depending on the radius is cosine. The total current value was determined bv sinusoidal dependence $I(t) = I_{\text{max}} \sin(\omega t), \ \omega = (2\pi/400) \text{ ns}^{-1}.$

Figure 3 shows the radial dependence of the pressure in the plasma column obtained by the numerical simulation with $I_{\text{max}} = 100 \text{ kA}$.

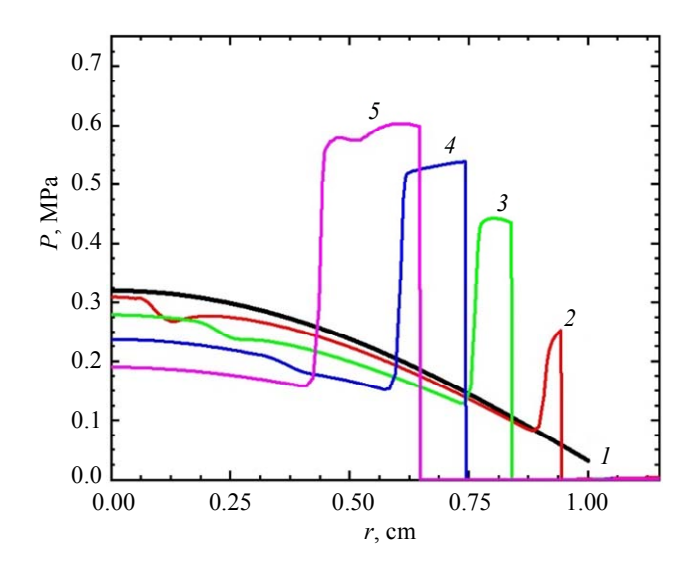


Fig. 3. The radial dependence of the pressure in the plasma column. The numbers indicate the time counted from the start of the conduction current (equal to 400 ns in Fig. 2): 1 – 0 ns, 2 – 100 ns, 3 – 200 ns, 4 – 300 ns, 5 – 400 ns

Figure 3 shows, the pressure increases near the outer surface of the plasma cylindrical sheath, and the region of the increased pressure shifts toward the axis of symmetry over time. This is due to the magnetic pressure pressing the low-density peripheral plasma toward the axis while the gas-dynamic pressure is simultaneously pushing the high-density substance away from the axis, thus forming a region with the increased density and consequently, with the increased pressure at the plasma region periphery.

Discussion of the results

When the electron beam interacts with the target surface, the torch of anode plasma is formed, and when high-power currents pass through the electrodes, plasma flow formed by explosive electron emission is separated from the cathode. At a certain moment, these two flows overlap the diode (see the lower part of the streak image in Fig. 1, which shows the plasma's own glow in the accelerator diode). thus forming conductance channel in the diode for the current passing after the pulse of subrelativistic electron beam, i.e. after 400 ns as shown in Fig. 2.

Figure 4 shows a transverse streak image: a image of the central part of the diode gap perpendicular to the diode axis is sweeped in time. As can be seen in Figure 4, the anode plasma reaches the recording region by the ~300th nanosecond; then, within ~100 ns, the diode gap is filled with almost uniform plasma, the transverse dimension of which increases from 0.5 cm to~ 1 cm by 400 ns, i.e., the radial velocity at the outer boundary being observed is equal to $\sim 3 \times 10^4$ m/s. After the time moment corresponding to 440 ns, the radiating plasma can be observed to be pressed along its outer visible boundary; in the same region (its thickness being ~1 mm), the plasma's own glow is more intense. According to the modeling results (Fig. 3), at the time corresponding 200–300 ns to from conduction current start in the plasma channel a pressing region of the same size and with the same pressing rate of $\sim 10^4$ m/s is formed; the pressure in this region is higher than in other parts of the plasma. Increase of the plasma pressure will lead to the increased pressure at the plasma column ends, which can give rise to another compression or shock

waves that are not directly related to the impact of the electron beam on the target surface. Thus, considering the processes occurring in the diode plasma can have a significant impact on the study of the dynamics of the formation and passage of compression and shock waves in solid targets.

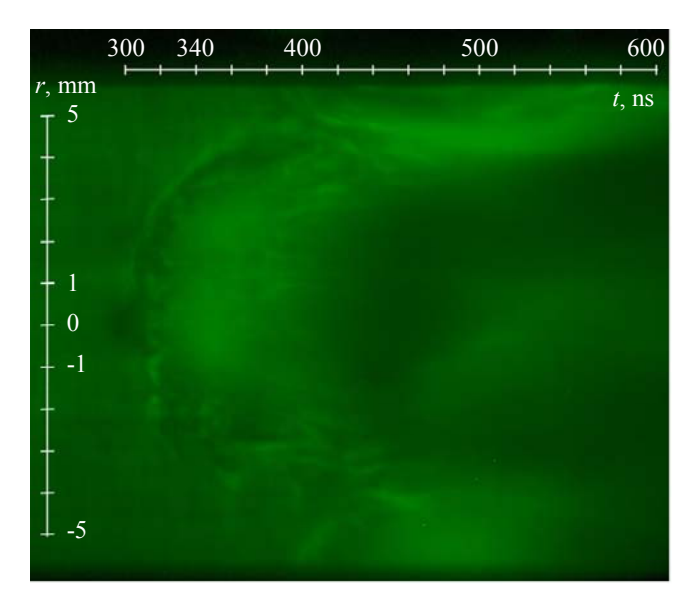


Fig. 4. The streak image recorded by the shadow photography method while simultaneously recording the plasma's own glow. The time-analyzing slit is oriented across the beam axis. The electron beam energy in the shot was 460 J

It is also worth noting that, as is shown in Fig. 1, some of these waves seem to change their propagation speed – they correspond to darkenings, the slope of which changes over time. The reason for the slope to change could be the process of wave formation not in the target surface region that corresponds to the beam axis, but, for example, near the outer boundary of the region where the beam and target interact. In this case compression waves will arrive at the region lying on the beam axis extension with different time delays, depending on the coordinate along the thickness of the target, which will cause the shadow with a slope changing along the target thickness.

Conclusion

Thus, both the experimental data and modeling results obtained in terms of onedimensional magnetohydrodynamics confirm that the processes occurring in the diode plasma should be taken into account when studying the dynamics of formation and propagation of compression and shock waves in targets. Moreover, considering that plasma parameters in the diode gap are quite extreme, the plasma can also significantly impact the degree of surface destruction of the materials being tested. To advance the research described herein, the more detailed analysis of the experimental data is suggested, including using the modeling results that we plan to obtain from the improved model.

Mathematical modeling was carried out with the support of the Russian Science Foundation (project No. 23-21-00248).

Experiments using Kalmar installation were conducted as part of the state assignment from the National Research Center Kurchatov Institute.

REFERENCES

1. Kovalenko V. A. and Kondratyev A. V., Aviation and space equipment and technology, No. 5, 14–20 (2011) [in Russian].

- 2. Rudakov L. I., Babykin M. V., Gordeev A. V. et al. Generation and focusing of high-current relativistic electron beams. Moscow, Energoatomizdat, 1990 [in Russian].
- 3. Grabovsky E. V., Vorobyov O. Yu., Dyabilin K. S., Lebedev M. E., Ostrik A. V., Smirnov V. P. and Fortov V. E., JETP Letters **60** (1), 1–4 (1984).
- 4. Lomov S. A. Introduction to the General Theory of Singular Perturbations. Moscow, Nauka, 1981.
- 5. Kanel G., Fortov V and Razorenov S., Physics-Uspekhi **50** (8), 771–791 (2007).
- 6. Didenko A. N., Ligachev A. E. and Kurakin I. B. Effect of charged particle beams on the surfaces of metals and alloys. Moscow, Energoatomizdat, 1987 [in Russian].
- 7. Kanel G. I., Razorenov S. V., Utkin A. V. and Fortov V. E. Shock-wave phenomena in condensed media. Moscow, "Yanus-K", 1996 [in Russian].
- 8. Ryabinin Yu. N., Technical Physics, No. 26, 2661 (1956).
- 9. Krivosheev S. I., Technical Physics **50** (3), 334–340 (2005).
- 10. Demidov B. A., Kazakov E. D., Kalinin Yu. G. et al., Instruments and Experimental Techniques, **63**, 370–374 (2020).
- 11. Demidov B. A., Kazakov E. D., Kalinin Yu. G. et al., Applied Physics, No. 6, 74–78 (2018) [in Russian].
- 12. Ananyev S. S., Bagdasarov G. A., Gasilov V. A. et al., Plasma Physics Reports **43**, 726–732 (2017).
- 13. Demidov B. A., Ivkin M. V., Petrov V. A. and Fanchenko S. D., Atomic Energy **46** (2), 111–116 (1979).
- 14. Kazakov E. D. et al., Plasma Physics Reports **47**, 803–813 (2021).

About authors

Evgeny Davidovich Kazakov, Deputy Head of the Department, Candidate of Physics and Mathematics, National Research Center Kurchatov Institute (123182, Russia, Moscow, Academician Kurchatov Square, 1). MPEI National Research Institute (111250, Russia, Moscow, Krasnokazarmennaya Ulitsa, 14). Moscow Institute of Physics and Technology (National Research University) (141701, Russia, Moscow Region, Dolgoprudny, Institutsky Per., 9). Keldysh Institute of Applied Mathematics of the Russian Academy of Science (125047, Russia, Moscow, Miusskaya, 4). E-mail: kazakov_ed@nrcki.ru SPIN code 2936-1306, Author ID 184827

Mikhail Yurievich Orlov, Research Engineer, National Research Center Kurchatov Institute (123182, Russia, Moscow, Academician Kurchatov Square, 1). E-mail: mosgotron@gmail.com

Anna Romanovna Smirnova, Junior Research Assistant, graduate student, National Research Center Kurchatov Institute (123182, Russia, Moscow, Academician Kurchatov Square, 1). Moscow Institute of Physics and Technology (National Research University) (141701, Russia, Moscow Region, Dolgoprudny, Institutsky Per., 9). Keldysh Institute of Applied Mathematics of the Russian Academy of Science (125047, Russia, Moscow, Miusskaya, 4). E-mail: anya4113@gmail.com SPIN code 8607-4923, Author ID 1254979

Mikhail Gennadievich Strizhakov, Research Assistant, National Research Center Kurchatov Institute (123182, Russia, Moscow, Academician Kurchatov Square, 1). E-mail: strizhakov_mg@nrcki.ru SPIN code 1430-1600, Author ID: 824117

Kirill Alexandrovich Sunchugashev, Laboratory Assistant, National Research Center Kurchatov Institute (123182, Russia, Moscow, Academician Kurchatov Square, 1). E-mail: 1032182603@pfur.ru

Liliya Maratovna Yusupova, Laboratory Assistant, student, National Research Center Kurchatov Institute (123182, Russia, Moscow, Academician Kurchatov Square, 1). MPEI National Research Institute (111250, Russia, Moscow, Krasnokazarmennaya Ulitsa, 14). E-mail: yusupova_lilia_m@mail.ru

Svetlana Ivanovna Tkachenko, Professor, Doctor of Physics and Mathematics Science, National Research Center Kurchatov Institute (123182, Russia, Moscow, Academician Kurchatov Square, 1). Moscow Institute of Physics and Technology (National Research University) (141701, Russia, Moscow Region, Dolgoprudny, Institutsky Per., 9). Keldysh Institute of Applied Mathematics of the Russian Academy of Science (125047, Russia, Moscow, Miusskaya, 4). United Institute of High Temperatures of the Russian Academy of Science (125412, Russia, Moscow, Izhorskaya Ulitsa, 13, bld. 2). E-mail: tkachenko@phystech.edu SPIN code 8352-8420, Author ID 108014

PLASMA PHYSICS AND PLASMA METHODS

UDC 532.5, 537.39 PACS: 68.03.Hj

Visualization of the electric field in transformer oil using suspended water microdroplets

© V. A. Panov*, A. S. Saveliev, Yu. M. Kulikov

Received 10.03.2025; revised 02.04.2025; accepted 07.04.2025 Scientific specialty code 1.3.9

A method for visualizing electric field lines in a dielectric based on electrohydrodynamic (EHD) destruction of small droplets is proposed. The advantage of the method is a significantly lower seeding density of tracers as compared to solid particles, which reduces the influence of the dispersed phase on the resulting EHD flow and electrical strength of the medium. The proposed approach allows introducing destructible tracer drops into individual areas under study, including into the area of lower potential values, which reduces the probability of partial breakdowns during diagnostics. The effectiveness of the approach is confirmed by comparing experimental visualization data with calculation results.

Keywords: electric field lines; visualization; high-voltage oil-filled equipment; EHD streaming; Taylor cone; droplets; water.

DOI: 10.51368/1996-0948-2025-2-62-68

Introduction

The behavior of drops in an electric field has been attracting the interest of scientists for many decades. The results of these studies have found application in various fields such as meteorology [1, 2] (raindrops), liquid drop model in nuclear fission [3], (movement) of aerosols [4]. A hundred years ago, Zeleny [5], as well as Wilson and Taylor [6], proved by way of the experiment that a drop suspended in a capillary (pendant drop) and a soap bubble

attached to a plate (sessile soap bubble) experience deformation in the electric field. What is more important, however, when electric field strength modulus on the surface of the pendant drop and sessile bubble was high enough, they became conical and emitted a thin stream that broke up into droplets. Papers [7, 8] discovered the similar behaviour exhibited in the presence of the electric field by a spherical pendant drop, which was initially electrically neutral. Unlike the pendant drop and sessile soap bubble, a neutral drop in the strong electric

field forms two opposite conical ends and emits streams of positively and negatively charged droplets in opposite directions. The conical menisci formed in the electric field are now known as Taylor cones [9], while emission of thin streams from cone tips is referred to as electrohydrodynamic (EHD) tip streaming [10] or cone EHD streaming [11].

The findings of many authors allow to reveal the universality of these phenomena: emission of charged streams from conical surfaces and their decomposition into aerosols consisting of charged micro (nano) droplets (electrospraying) are common to various, allegedly unrelated situations during production processes and natural phenomena, including electrospray ionization mass spectrometry (ESIMS) [12], raindrops in thunderclouds [13], as well as printing and coating [14].

The droplet electrohydrodynamics has advanced into an independent discipline due to the papers of Taylor [15, 16], who gave criticism of previous research in this area and proposed his own theoretical leaky dieletric model (LDM). He also described stable minor deformation of a (single-phase) droplet. Later this model was repeatedly tested, and more accurate models emerged [15–21]. subsequent works researched the complex topologies of interphase boundaries associated with multiphase emulsion droplets, the development of instabilities in emulsions, their decomposition (demulsification), and control of microparticles movement at the interphase boundary.

Although this area has been researched for many decades, most research efforts are of an academic nature, and only recently a series of works of applied significance has appeared [22–34].

The present study aims to extend the findings of droplet electrohydrodynamics to

high-voltage engineering problems. This paper proposes the method for visualizing electric field lines, which is based on the comparison of laboratory and numerical experiments findings. The approach is based on visualizing trajectories of microdroplets formed as a result of decomposition of streams flowing from conical menisci of drops (Taylor cones) under the influence of the electric field.

Experimental setup

The experimental setup diagram is shown in the figure. 1. Two immiscible liquids are poured into vessel (1) with planeparallel transparent walls made of organic glass: poorly conducting water (2) and transformer oil (3). A pointed high-voltage needle electrode (4) and a cylindrical electrode (5) with a rounded edge at the working end, which is connected to the "ground" through measuring resistor R_s with a resistance of 25 Ω , are immersed in oil and water, respectively. The voltage is supplied through the limiting resistor R_b (5 k Ω) to electrode (4) using semiconductor highvoltage switch (6) of the "half-bridge" type when a rectangular TTL pulse is formed at its input using digital pulse generator G. The voltage rise and fall front at the output of switch (6) is about 0.1 µs, which is much faster than the phenomena described herein.

The voltage amplitude was $V_0 = 20 \text{ kV}$, and the open state duration of switch (6) was 400 μ s. Since the high-voltage source ("DC" Fig. 1) cannot provide the sufficient output current (hundreds of milliamps) in case of breakdown of the interelectrode gap, high-voltage storage capacitor C with the capacity of 0.7 μ F is added to the electrical circuit in parallel with the source. To measure the voltage on high-voltage electrode (4), a high-

voltage probe 1:1000 is connected at point A, and a signal from this probe is sent to the digital storage oscilloscope.

To measure the current in the circuit, the voltage at point B is supplied to the oscilloscope. A signal from generator G, as well as an exposure sync pulse from high-speed digital video camera (8), are sent to other channels of the oscilloscope.

To visualize the occurring processes, background lighting (incandescent lamp (7)) and video camera (8) are used, with container (1) placed in between. The video camera lens is focused on the plane containing the electrode axis. The electrical breakdown is

forced in liquids in advance according to the mechanism described in [35–37]. As a result, small (about 50 µm) water droplets appear in the oil in the interelectrode region (9). Since the lens depth of field is relatively small, the droplets that are close to the straight line containing the electrode axes can be seen as dark circles (Fig. 2). The droplets that are farther from this line, i.e. beyond the lens depth of field can be seen as fuzzy rings or half rings (Fig. 3). After water droplets are formed in the interelectrode space, the potential difference develops between the electrodes to deform and destroy them (Fig. 3).

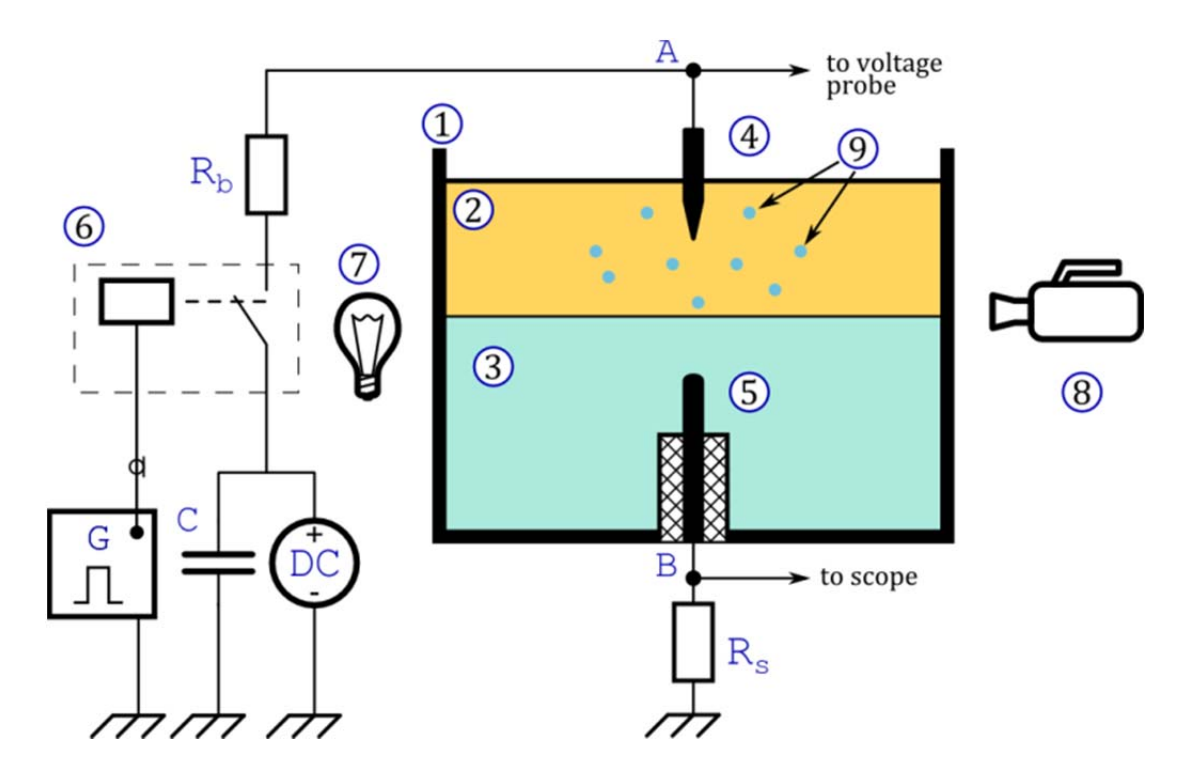


Fig. 1. Experimental setup diagram

Mathematical model

The problem is modeled in the axisymmetric setup. The electrode system is assumed to be immersed in a cylinder of 80 mm in diameter which is equal to the side of

the experimental cell. The tip of the oil-immersed electrode is 3 mm away from the interphase boundary, the total thickness of the oil layer is 15 mm, the distance from the pin electrode surface to the interphase boundary is also 3 mm. The diameter of the

cylindrical section of the pointed electrode is 1 mm, that of the cylindrical electrode – 1.8 mm. The radius of the needle tip rounding is 70 μ m. Properties of materials filling the subdomains of calculation: water with relative permittivity $\epsilon_w = 78$, transformer oil with $\epsilon_o = 2$. Since liquids are considered to be ideal dielectrics, the electrostatic approximation described by the below system of equations is used:

$$\vec{E} = -\nabla V,$$

$$\vec{D} = \varepsilon \vec{E},$$

$$\nabla \cdot \vec{D} = \rho_{v},$$

where \vec{E} – electric field vector, V – electrostatic potential, \vec{D} – electric displacement vector, ε – relative permittivity of the medium, ρ_v – volume charge density.

Spatial discretization of the system of equations is based on the finite element method. Values in cells are interpolated using second-order Lagrange polynomials. The following conditions are set at the boundaries: 1) condition of axial symmetry, 2) high-voltage potential $V_0 = 20 \text{ kV}$ is set on the surface of the pointed electrode, 3) zero charge $(\vec{n} \cdot \vec{D} = 0)$, 4) zero potential (grounding) is set on the surface of the cylindrical electrode. The domain calculation is covered with a triangular mesh of the finer size near the high-voltage electrode to ensure the best resolution of high voltage values. The maximum size of an element within the medium volume is 1 mm. the minimum size is 10 μm. The element size at the boundary of the high-voltage electrode does not exceed 10 µm. The total amount of mesh elements is 505,516 cells. The relative tolerance of the iterative solver is 0.001. Due to the small size of droplets as compared to the size of the discharge gap, the electric field calculated without considering their presence.

Results and discussion

The figure 2 shows the image of the discharge gap and visible part of electrodes before the voltage pulse is applied. Water droplets acting as future tracers of electric field lines look like dark circles in the upper half of the image occupied by transformer oil. The dark strip adjacent to the water-oil interface is a shadow of the water meniscus that appears on the wall of the discharge cell at the stage of droplet formation through the electrical breakdown of the same gap. The misalignment of electrodes which can be seen on the photo is caused only by the difference in refractive indices of water and oil and the camera' set angle of view. Prior to the experiment the alignment is checked by directly touching the two electrodes on their axis.

Figure 3 shows water droplets before and at the end of voltage pulse sending. Initially, spherical droplets (top figure, 0 µs) begin to deform under the impact of the external electric field: they are stretched along the electric field lines. The visualization of electric field lines becomes even more adequate for the droplets, at which poles pointed peaks emitting fine droplets are formed. For example, droplet 1 in figure 3, by the end of the pulse, has almost completely decomposed into two clouds of fine droplets towards the high-voltage and grounded electrodes due to being in the region of the stronger field as compared to droplets 2 and 3. Droplet 2 is also fragmented, but since it is far from the electrode, the droplet is more drawn out and less streamed, which has beneficial for the quality of visualization of the electric field lines. The comparison with the calculated pattern of the electric field lines shown in the lower part of figure 3 reveals that the course of the lines is well aligned with the direction of deformation and streaming of the droplets.

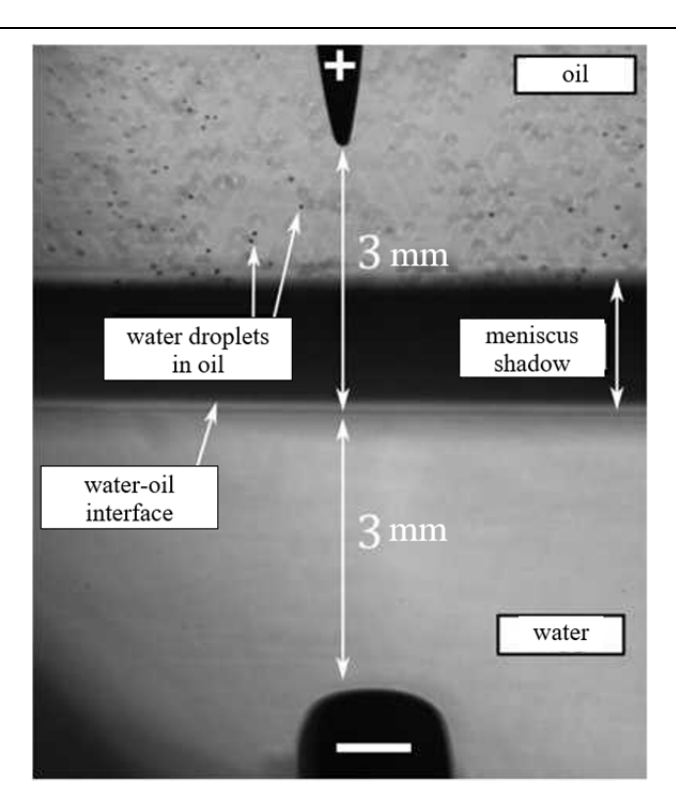


Fig. 2. View of the discharge gap before the voltage pulse is sent

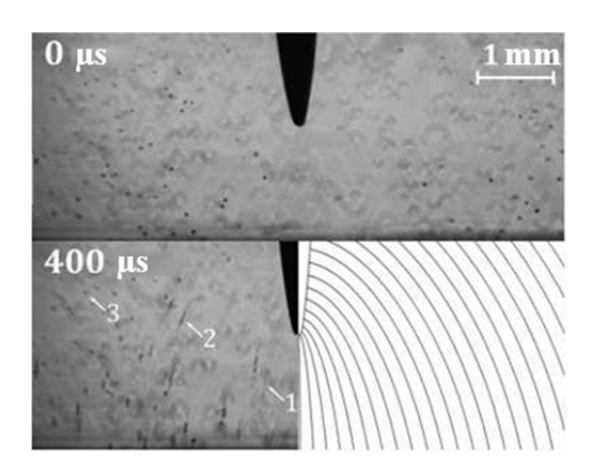


Fig. 3. Deformation and streaming of water droplets distributed in oil under the action of the voltage pulse with the amplitude of 20 kV and a duration of 400 µs (moments 0 and 400 µs). The second half of the lower image is supplemented with the calculated pattern of the electric field lines which was built for the experimental parameters

Conclusions

The method for visualizing the pulsed electric field lines in a dielectric liquid, which consists in observing the direction of deformation and streaming of droplets of a second liquid placed in the first one, has been proposed. The method has been tested using the water droplets placed in transformer oil, with the pulsed voltage fed to the needle-shaped high-voltage electrode. With the droplets used as tracers, the response time of

the droplets to the external field and their noticeable deformation is only 100 µs in the experiment conditions under consideration. The fragmentability of droplets lowers the requirements for the tracer seeding density and also allows positioning them locally in the area of concern. With the lower seeding density, the impact on the electrical strength of the medium is decreased, which reduces the probability of partial breakdowns during diagnostics.

REFERENCES

- 1. Rayleigh L., Philos Mag **14** (87), 184–186 (1882).
- 2. Sartor J. D., Physics Today **22** (8), 45–51 (1969).
- 3. Bohr N. and Wheeler J. A., Physical Review **56** (5), 426–450 (1939).
- 4. Taflin D. C., Ward T. L. and Davis E. J., Langmuir **5** (2), 376–384 (1989).
- 5. Zeleny J., Physical Review **10** (1), 1–6 (1917).
- 6. Wilson C. T. R. and Taylor G. I., Mathematical Proceedings of the Cambridge Philosophical Society **22** (5), 728–730 (1925).
- 7. Nolan J., Proc R Ir Acad Sect A **37**, 28–39 (1926).
- 8. Macky W., Proceedings of the Royal Society of London. Series A. Containing Papers of a Mathematical and Physical Character **133** (822), 565–587 (1931).
- 9. Taylor G., Proceedings of the Royal Society of London. Series A. Mathematical and Physical Sciences **280** (1382), 383–397 (1964).
- 10. Collins R. T., Jones J. J., Harris M. T. and Basaran O. A., Nature Physics **4** (2), 149–154 (2007).
- 11. Cloupeau M. and Prunet-Foch B., Journal of Electrostatics **22** (2), 135–159 (1989).
- 12. Fenn J. B., Mann M., Meng C. K., Wong S. F. and Whitehouse C. M., Science **246** (4926), 64–71 (1989).
- 13. Brazier-Smith P. R. and Jennings S. L. J., Q J R Meteorol Soc **99** (422), 776–786 (1973).
- 14. Lee D.-Y., Shin Y.-S., Park S.-E., Yu T.-U. and Hwang J., Applied Physics Letters **90** (8), 081905 (2007).
- 15. Taylor G. I., Proceedings of the Royal Society of London. Series A. Mathematical and Physical Sciences **291** (1425), 159–166 (1966).
- 16. Melcher J. R. and Taylor G. I., Annual Review of Fluid Mechanics **1** (1), 111–146 (1969).
- 17. Saville D. A., Annual Review of Fluid Mechanics **29** (1), 27–64 (1997).
- 18. Zholkovskij E. K., Masliyah J. H. and Czarnecki J., Journal of Fluid Mechanics **472**, 1–27 (2002).
- 19. Schnitzer O. and Yariv E., Journal of Fluid Mechanics **773**, 1–33 (2015).

- 20. Bazant M. Z., Journal of Fluid Mechanics **782**, 1–4 (2015).
- 21. Mori Y. and Young Y.-N., Journal of Fluid Mechanics **855**, 67–130 (2018).
- 22. Geng H., Feng J., Stabryla L. M. and Cho S. K., Lab on a Chip **17** (6), 1060–1068 (2017).
- 23. Jia Y., Ren Y., Hou L., Liu W., Deng X. and Jiang H., Small **13** (46), 1702188 (2017).
- 24. Loscertales I. G., Barrero A., Guerrero I., Cortijo R., Marquez M. and Gañán-Calvo A. M., Science **295** (5560), 1695–1698 (2002).
- 25. Song R., Abbasi M. S. and Lee J., Microfluidics and Nanofluidics **23** (7), 92 (2019).
- 26. Tucker-Schwartz A. K., Bei Z., Garrell R. L. and Jones T. B., Langmuir **26** (24), 18606–18611 (2010).
- 27. Xie J., Jiang J., Davoodi P., Srinivasan M. and Wang C.-H., Chemical Engineering Science **125**, 32–57 (2015).
- 28. Bhaumik S. K., Roy R., Chakraborty S. and DasGupta S., Sensors and Actuators B: Chemical **193**, 288–293 (2014).
- 29. Wehking J. D. and Kumar R., Lab on a Chip **15** (3), 793–801 (2015).
- 30. Xi H.-D., Guo W., Leniart M., Chong Z. Z. and Tan S. H., Lab on a Chip **16** (16), 2982–2986 (2016).
- 31. Guan X., Hou L., Ren Y., Deng X., Lang Q., Jia Y., Hu Q., Tao Y., Liu J. and Jiang H., Biomicrofluidics **10** (3), 034111 (2016).
- 32. Huo M. and Guo Y., Polymers **12** (2), 335 (2020).
- 33. Lecuyer S., Ristenpart W. D., Vincent O. and Stone H. A., Applied Physics Letters **92** (10), 104105 (2008).
- 34. Nguyen V. D. and Byun D., Applied Physics Letters **94** (17), 173509 (2009).
- 35. Panov V. A., Kulikov Yu. M., Vetchinin S. P., Pecherkin V. Ya. and Vasilyak L. M., Plasma Sources Sci. Technol. **32**, 095020 (2023).
- 36. Panov V. A., Vasilyak L. M., Pecherkin V. Ya., Vetchinin S. P. and Kulikov Yu. M., Applied Physics, No. 4, 5–10 (2022) [in Russian].
- 37. Panov V. A., Kulikov Yu. M., Pecherkin V. Ya., Vasilyak L. M. and Saveliev A. S., Applied Physics, No. 6, 5–10 (2023) [in Russian].

About authors

Vladislav Aleksandrovich Panov, Senior Research Assistant, Candidate of Physics and Mathematics, Joint Institute for High Temperatures of the Russian Academy of Sciences (125412, Russia, Moscow, Izhorskaya Ulitsa, 13, bld. 2). E-mail: panovvladislav@gmail.com SPIN code 5821-2776, Author ID 755538

Andrei Sergeevich Saveliev, Senior Research Assistant, Candidate of Physics and Mathematics, Joint Institute for High Temperatures of the Russian Academy of Sciences (125412, Russia, Moscow, Izhorskaya Ulitsa, 13, bld. 2). E-mail: fisteh@mail.ru SPIN code 6888-7369, Author ID 866343

Yurii Matveevich Kulikov, Senior Research Assistant, Candidate of Physics and Mathematics, Joint Institute for High Temperatures of the Russian Academy of Sciences (125412, Russia, Moscow, Izhorskaya Ulitsa, 13, bld. 2). E-mail: kulikov-yurii@yandex.ru SPIN code 7719-8459, Author ID 1130937

PLASMA PHYSICS AND PLASMA METHODS

UDC 533.9.07 PACS: 52.75.Hn EDN: QHEIAV

Study of the dynamics of arc discharge burning in the methane-hydrogen-containing atmosphere in the alternating current plasma torch

© Yu. D. Dudnuk*, A. A. Safronov, V. N. Shiryaev, M. I. Vasilyev, O. B. Vasilieva

Institute for Electrophysics and Electric Power of Russian Academy of Sciences,
Saint Petersburg, 191181 Russia
* E-mail: julia_dudnik-s@mail.ru

Received 19.12.2024; revised on 24.01.2025; accepted 07.04.2025 Scientific specialty code: 1.3.13

The results of the study of the dynamics of arc discharge burning in the electric arc chamber of an alternating current plasma torch with the power of up to $10 \, kW$ are presented. The measurements were carried out using graphite and tungsten electrode tips at the atmospheric pressure in the following ranges of plasma-forming gas flow rates: H_2 up to $0.08 \, g/s$ and mixture H_2+CH_4 up to $0.1 \, g/s$. Characteristic stages of discharge development were established, among which contracted, diffuse including formation of a plasma plume, and transient types of arc discharge were observed.

Keywords: plasma torch; alternating current; arc discharge; high-speed video recording.

DOI: 10.51368/1996-0948-2025-2-69-75

Introduction

The study of arc plasma burning modes is one of the most important tasks of modern low-temperature plasma physics. Due to their unique properties, such as high temperature and energy density, arc discharges are widely used in various fields of science and technology, including metallurgy, welding technologies, coating technologies, plasma chemistry, powder material production technologies, etc. Despite the number of papers [1–5] devoted to the study of arc plasma, some aspects of its behaviour remain underexplored.

Being widely used in industrial processes, plasma torches require a deep

understanding of the mechanisms for the arc discharge to form and exit stably. Traditional diagnostic methods based on measuring electrical parameters are often not enough to fully describe the dynamic pattern of arc burning, especially under conditions of rapid temporal and spatial changes. High-speed photo and video shooting is an effective means of visualizing and analyzing arc burning processes in the discharge chamber. This method allows recording instantaneous changes in the arc structure, following its movement and deformation, and identifying key mechanisms of plasma interaction with surrounding surfaces. Modern digital cameras with high resolution and frame rate allow a detailed analysis of temporal and spatial

characteristics of the arc discharge, which is critical for understanding and optimizing the operation of plasma torches.

Due to their ability to generate high-enthalpy gas flows, plasma torches during plasma-chemical synthesis intensify chemical processes in the gas phase while the reaction zone and size of the process equipment become much smaller and the yield of the useful product grows.

The electric arc that occurs between the electrodes in the plasma torch chamber creates conditions for the high-temperature plasma to form. The main parameters that influence the arc burning dynamics include temperature, current density, gas pressure and components composition of the plasmamedium. forming The arc combustion dynamics influences the uniformity temperature distribution of the and concentration of active particles in the plasma volume. Inhomogeneous distribution of these parameters can lead to uneven chemical reactions and, as a consequence, to a decrease in the yield of target products. For this reason, the optimization of these parameters allows achieving maximum efficiency of plasmachemical processes and increasing the yield of useful products.

The goal of this paper is to study the processes of arc discharge formation and development using photo and video shooting methods. This will allow establishing the temporal and spatial characteristics of the arc discharge, such as shape and dimensions of the arc channel, radiation intensity, etc. The measurements were carried out using graphite and tungsten electrode tips at the atmospheric pressure in the following ranges of plasma-forming gas flow rates: H₂ up to 0.08 g/s and mixture H₂+CH₄ up to 0.1 g/s. Plasma torch operating modes have been analyzed, and arc burning modes have been described.

Experimental unit and measurement methods

The studies were carried out using the experimental setup, which scheme is shown in Figure 1 and which comprises an alternating current plasma torch [6, 7], a power source, a plasma-forming gases cooling and a supply system, as well as a set of measuring instruments.

The plasma torch includes two housings made of 12X18N10T stainless steel. Each housing contains a water-cooled electrode unit with replaceable graphite output inserts. The electrode unit consists of a water-cooled housing and an electrode with a tip fixed to its end. The tip can be made of various materials, as tungsten, graphite or copper. The housing has a channel for tangential supply of plasma-forming gas, which forms a spiral gas-vortex flow the cools and stabilizes the arc channel. A flange fixed to the nozzle unit that makes a space between the housing and inner wall for feeding the cooling water that ensures heat removal from the arc ignition zone. The electrode channels are arranged coaxially and connected to the electric arc chamber, which can operate as a reaction chamber acting as a plasma-chemical reactor when the material to be processed is added.

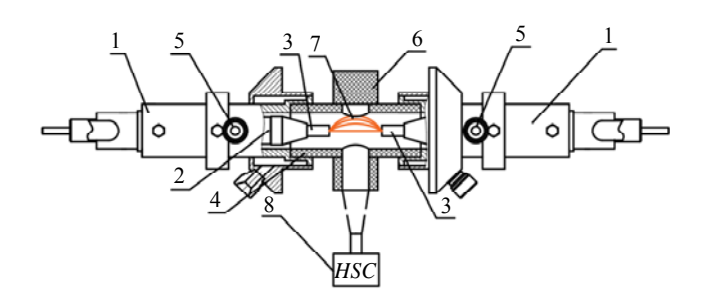


Fig. 1. Schematic view of the plasma torch and observation method using high-speed photo and video shooting: 1 – housing; 2 – electrode; 3 – tip; 4 – sleeve; 5 – gas supply; 6 – electric arc chamber; 7 – arc; 8 – high-speed chamber

With the high voltage supplied between the electrode and the inner wall of the channel, the electrical breakdown of the interelectrode gap occurs, which results in arc formation. Forced by the tangential gas flow supplied into the channels, the arcs move to the electrode ends, then they move along the graphite insert, are blown out onto its end and are connected to the electrode from the opposite channel. Thus, the arc spreads from the end of one electrode to the end of another one. When the polarity changes, the same things occur on the other electrode. Formation of the vortex gas flow in the channels facilitates the efficient removal of excess heat from the central arc. thus preventing temperature gradients and associated instabilities of the plasma channel from being developed.

It should be emphasized that plasmaforming gases can be mixed in the plasma torch of this type without the need to stop and additionally readjust the device. This feature allows conducting various experiments, thus significantly reducing time and material amounts. To ensure the guaranteed ignition the device was started using argon with the flow rate of up to 0.5 g/s. Upon reaching a steady state, hydrogen was supplied within the operating flow rate range, while the argon supply was stopped. Later ballast gases were not used to maintain discharge burning.

High-speed shooting was carried out using Citius imaging High Speed Video Camera arranged perpendicularly to plasma torch axis. The camera is capable of shooting at up to 4000 frames per second (fps) in high resolution. The proper interfaces allow connecting the camera to a personal computer, which enables the remote control of shooting settings and real-time monitoring of the shooting process. This recording allowed locating the method arc conducting the detailed analysis of the temporal and spatial characteristics of the arc discharge.

Findings and discussion

As part of the research performed, a number of experiments were carried out using photo and video shooting. The hydrogen flow rate varied up to 0.08 g/s, methane flow rate – up to 0.02 g/s, and the plasma torch power varied within the range of up to 10 kW; the total duration of the experiment did not exceed 30 minutes.

The analysis of the measurement results considered both static characteristics reflecting the time-averaged ratios changing parameters and dynamic characteristics associated with changes in the arc burning process over time. The arc burning dynamics were recorded by means of the corresponding oscillograms: the current change over time was sinusoidal, and the voltage curve exhibited distinct ignition and extinction peaks when crossing zero.

The total duration of the voltage change half-period on the oscillogram can be divided into three parts. The first and third parts correspond to the lateral sides of the trapezoid – these are the stages of voltage increase and decrease in the interelectrode gap, when the arc discharge has not yet formed or has already ceased to exist. The middle part, which can be called the trapezoid "base", is characterized by voltage fluctuations around the average value and corresponds to the arc discharge lifetime. In some half-periods, a slight increase in voltage is observed closer to the middle of this interval. The amplitude magnitude of peak voltage fluctuations varies depending on the gas type and is within the range of 1.2 to 4 kV.

The result of high-speed video shooting of the discharge in the electric arc chamber of the plasma torch were files of the .avi format, which reflect the dynamics of various modes of the arc discharge under study. To clean the frames from the noise, which existed as constantly glowing areas near the electrodes, the .avi files were filtered. Among all the file frames, there was one whose integral

luminosity of the frame was minimum, that is, when the discharge was obviously absent. Next, the matrix of the frame with the minimum luminosity was subtracted from the matrix of each frame of the file. The result was a new .avi file with minimum noise. The new files provided were processed as follows. The sum of all matrix pixels with a resolution of [320 \times 306] of the next *j*-th frame was calculated. The result of summing was written to the *j*-th position of the new vector, the length of which corresponded to the number of frames in the .avi video file. According to this procedure, the dependence of the relative luminosity intensity on time was calculated for all the discharges under study. The relative luminosity intensity can be assumed to correlate well with the calculated discharge current power. Using the resulting vector of relative luminosity intensity of the discharge under study, the frequency characteristic of the process was determined using the Fourier transform "fft". For all discharge types, the fundamental frequency was 100 Hz with minor satellite frequencies that were multiples of the fundamental frequency.

The figures show successive frames from the video files recorded with Citius high-speed camera with the video shooting rate of 4000 frames per second and exposure of 10 us normal to the discharge plane. The frames show the electrode tip, from its material (tungsten and graphite) is torn out and carried away with the plasma flow upon application of the current pulse. The frames were selected as follows: with reference to the derived vector previously of relative luminosity intensity, the successive frames were selected, starting with the minimum value of the discharge luminosity, that is, from the discharge start until the maximum luminosity intensity was reached, and then decreasing frames with the discharge luminosity intensity were selected until the given discharge period extincted. The right inset in Figure 2 shows an example of a transient discharge, where the points on the discharge intensity curve mark the selected frame numbers from the video file, starting with number 235. The frames were selected similarly from the corresponding video files of other categories for Figures 3 and 4.

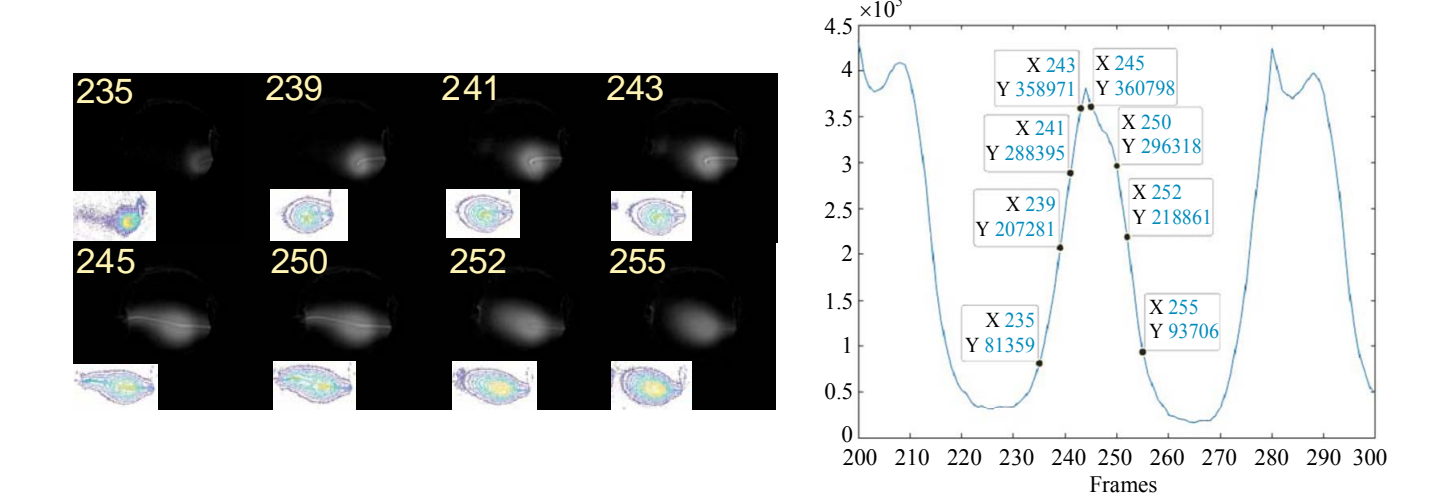


Fig. 2. Transient discharge mode with a pattern of radiation intensity distribution depending on the frame number, flow rate of hydrogen H_2 is 0.06 g/s, current is 6 A, power is 6 kW

Figure 2 shows the pattern of the transient discharge developing, including the initial formation of a plasma cloud near the

electrode, where the arc ignites (forms), without reaching the opposite electrode it bends (extends) to the end of the electrode

and is blown out by the plasma-forming gas flow towards the opposite electrode. After the maximum intensity values (frames 245 and 250) are reached, the arc moves back to the electrode where it was ignited. Note that a plasma cloud is observed around the arc tip at all stages. The diameter of the plasma cloud reaches 25–30 mm. This mode is observed at the plasma-forming hydrogen gas flow rate up to 0.06 g/s, in case of short heating of the electric arc chamber for several minutes and after reaching a steady-state mode, as well as in case of hydrogen-methane ratio of 6:1 during the first minutes of operation.

The contracted discharge is shown in Figure 3. It is typical for the hydrogen flow rate of 0.04–0.08 g/s and is observed in case of the "cold" chamber. Almost immediately, a clearly defined arc is formed, where the pressure of the self-magnetic field exceeds the gas kinetic pressure, thus resulting in contraction. As the discharge develops, an increase in the arc cross-section is observed. This may depend on the change in the pressure ratio of the self-magnetic field and gas-kinetic field in the favor of the latter's pressure. This can also explain the gradual curving of the arc by the working gas blown out.

Note that both the arc initiation (frame 145) and extinction in this half-period under consideration (frame 180) originated from the right electrode. In the next half-period, with the polarity changed on the electrodes, the arc ignites on the left electrode (frame 186). The weak section of the arc can also be

noticed around the opposite electrode. No arc radiation was observed between these areas. The sensitivity threshold of the video camera receiver is most likely to be lower than the arc luminosity in this area and it is not enough for being recorded. It can be assumed that if we used a more sensitive colour photodetector matrix, we could examine R, G and B matrices of this frame individually to see this area, probably, in more details.

Figure 4 shows the pattern of the discharge development referred to in the foreign scientific literature as a plasma plume [8, 9] (plasma cloud). Gas-dust plasma clouds were often observed during the experiments with arc discharges on graphite electrodes, a gradual expansion of plasma plume from frame to frame to occupy the half-space up to the middle of the interelectrode distance, which was ~30 mm. After the maximum luminosity of the discharge was reached, which corresponds to the maximum power (frames 241 and 244), the reverse process of plasma cloud contraction occurs until it completely extincts. It should be noted that there is a region of increased brightness in the near-electrode space, which resembles a forming arc; however, as can be seen from the lines of equal intensity, no clearly visible arc can be observed. The presence of a plasma cloud could only be recorded by mixing two types of plasma-forming gas, methane and hydrogen, in the ratios of 1:8, 1:6, 1:3. The main gas, hydrogen, was varied in the range of 0.06 g/s to 0.08 g/s, then methane was mixed into it at the rate of 0.01 g/s.

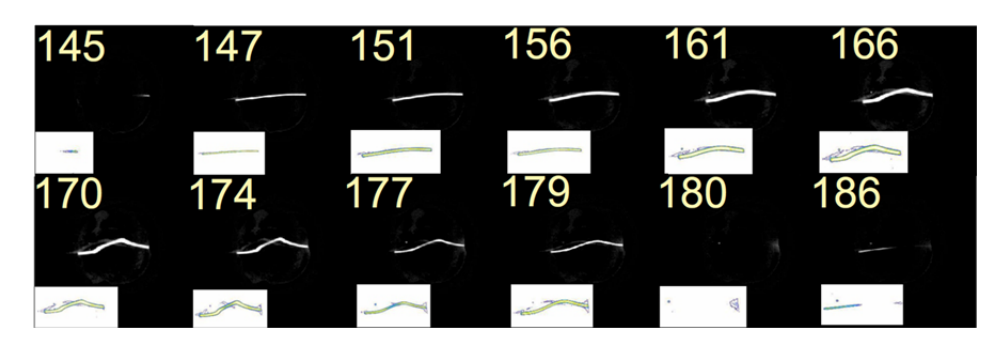


Fig. 3. Contracted discharge mode, flow rate of hydrogen H_2 is 0.06 g/s, current is 6 A, power is 6 kW

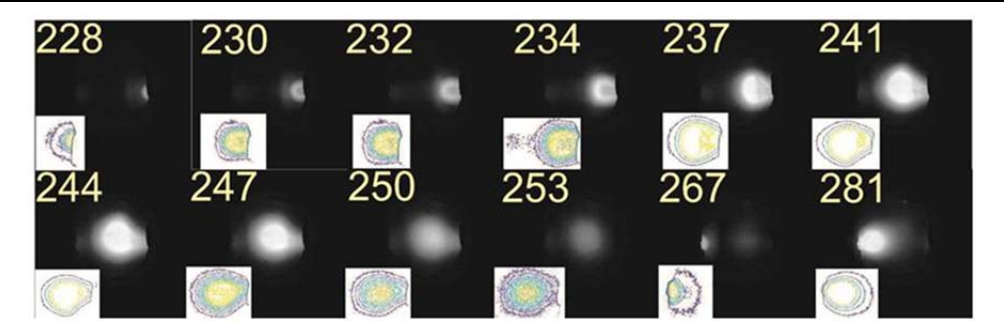


Fig. 4. Diffuse (plasma plume) discharge mode, mixture flow rate: hydrogen $H_2 - 0.08$ g/s and methane $CH_4 - 0.01$ g/s, current is 6 A, power is 7 kW

Considering that the setup was not changed during the experiments, the changeover from the intermediate (transition) discharge, with the plasma cloud formed at first near the electrode, to the contracted one and then to the plasma plume (plasma cloud), the different nature of the discharge can be explained by the ionization degree of the working gases used in the experiment and by the pressure difference.

Conclusion

The paper analyzes the burning dynamics features of arc discharge at the atmospheric pressure in the ranges of plasmaforming gas flow rates: H₂ up to 0.08 g/s and mixture H_2+CH_4 up to 0.1 g/s in the plasma alternating current torch. of Characteristic discharge stages development were established, among which contracted, diffuse including formation of a plasma plume, and transient types of discharge observed. Contracted were discharge is typical for the hydrogen flow rate of 0.04-0.08 g/s with a clearly defined arc body formed. The transient discharge mode was recorded at the flow rate of the plasmaforming gas, hydrogen, of up to 0.06 g/s and with the hydrogen and methane mixture ratio of 6:1; a plasma cloud with a diameter of 25-30 mm formed around the arc body was observed. The diffuse discharge mode with

the gas-dust plasma plume occurring took place in the modes of methane and hydrogen mixture ratios of 1:8, 1:6, 1:3.

REFERENCES

- 1. Finkelnburg W. and Maecker H., Elektrische Bögen und Thermisches. Plasma Handbuch der Physik Berlin **22** (1956); Moscow, Inostrannaya literature, 1961.
- 2. Raizer Yu. P., Physics of gas discharge. Moscow, MFTI, 2009 [in Russian].
- 3. German V. O., Glinov A. P., Golovin A. P., Kozlov P. V. and Lyubimov G. A., Applied Physics, No. 6, 108–115 (2021) [in Russian].
- 4. Stepanov E. Yu., Dolinovskaya R. V. and Shabalin S. A., Scientific and Technical Journal of St. Petersburg State Polytechnic University, No. 3–2 (154), 110–114 (2012) [in Russian].
- 5. Verameychyk A. I., Onysko S. R., Sazonov M. I. and Khvisevich V. M., Vestnik of Brest State Technical University, No. 3 (126), 79–81 (2021).
- 6. Kuznetsov V. E., Dudnik Yu. D., Safronov A. A., Shiryaev V. N., Vasilieva O. B., Gavrilova D. A. and Gavrilova M. A., Problems of thermonuclear energy and plasma technologies. Proc. of the III Intern. Conf. Tarusa, 2023. pp. 67–68.
- 7. Dudnik Yu. D., Kuznetsov V. E., Safronov A. A., Shiryaev V. N. and Vasilyeva O. B., Physics St. Petersburg St. Petersburg, 2024, pp. 273–275 [in Russian].
- 8. Pickin C. and Young K., Sci Technol Weld Join. **11** (4), 1–3 (2006).
- 9. Bartkowiak K. and Vasilyev M., 3rd Pacific Intern. Conf. on Applications of Lasers and Optics, PICALO 2008. Conf. Proc. 2008, pp. 267–272.

About authors

Yulia Dmitrievna Dudnik, Research Assistant, Federal State Budgetary Scientific Institution Institute for Electrophysics and Electric Power of the Russian Academy of Sciences (191181, Russia, Saint Petersburg, Dvortsovaya Emb., 18). E-mail: julia_dudnik-s@mail.ru SPIN code 7170-7912, Author ID 670805

Alexey Anatolyevich Safronov, Department, Head, Leading Research Assistant, Federal State Budgetary Scientific Institution Institute for Electrophysics and Electric Power of the Russian Academy of Sciences (191181, Russia, Saint Petersburg, Dvortsovaya Emb., 18). E-mail: 9932553@mail.ru SPIN code 5771-1927, Author ID 37228

Vasily Nikolaevich Shiryaev, Senior Research Assistant, Federal State Budgetary Scientific Institution Institute for Electrophysics and Electric Power of the Russian Academy of Sciences (191181, Russia, Saint Petersburg, Dvortsovaya Emb., 18). E-mail: shiryaev_vasily@mail.ru SPIN code 6728-5133, Author ID 37225

Mikhail Ivanovich Vasiliev, Research Assistant, Federal State Budgetary Scientific Institution Institute for Electrophysics and Electric Power of the Russian Academy of Sciences (191181, Russia, Saint Petersburg, Dvortsovaya Emb., 18). E-mail: milavas@mail.ru SPIN code 6836-0810, Author ID 162131

Olga Borisovna Vasilieva, Research Assistant, Federal State Budgetary Scientific Institution Institute for Electrophysics and Electric Power of the Russian Academy of Sciences (191181, Russia, Saint Petersburg, Dvortsovaya Emb., 18). E-mail: vasilieva_olg@mail.ru SPIN code 7691-1515, Author ID 161866

PLASMA PHYSICS AND PLASMA METHODS

UDC 621.383.327.53 PACS: 52.80.Mg EDN: LPCHXW

High-current photoemission glow discharge in Xe-Cs mixture

© A. M. Martsinovsky¹, S. V. Gavrish^{2,*}, D. G. Korenyugin³, A. S. Guslin³, V. N. Kuzin³

¹ Ioffe Institute, Saint Petersburg, 194021 Russia
² Scientific and Industrial Enterprise "Melitta", LLC, Moscow, 117997 Russia

* E-mail: svgavr@list.ru

³ Peter the Great St. Petersburg Polytechnic University, Saint Petersburg 195251 Russia

Received 17.02.2025; revised 04.03.2025; accepted 07.04.2025

Scientific specialty code: 2.2.1

An unusual high-current photoemission glow discharge was discovered in Xe–Cs mixture. Its burning voltage is several times lower, while the current density is 1–2 orders of magnitude higher than those of a regular glow discharge in pure xenon and cesium. Such discharges developed in cesium illuminating lamps of pulse-periodic discharge when they were heated by the alternating voltage before the supply of high-current operating pulses at a xenon pressure of 20 torr and within a wide range of cesium pressures from 10⁻⁶ to 1 Torr. Such discharges may be caused by photoemission from W–Th–Cs structures on the electrodes under the influence of strong UV radiation from the cathode layer.

Keywords: glow discharge; xenon; cesium; mercury-free illuminating lamps; photoemission; thermal emission; UV radiation; cathode layer; current-voltage characteristic.

DOI: 10.51368/1996-0948-2025-2-76-83

Introduction

High-pressure cesium illuminating high-current lamps of pulse-periodic discharge (PPD) feature a very successful combination of characteristics: they mercuryfree (environmentally safe), quite energy efficient (luminous efficacy up to 60– 70 lm/W), and provide the light exceptionally high quality (color rendering index R_a up to 95-98) with a spectrum approaching the solar one not only in the visible but also in the near UV band [1–3]. The latter feature allows them to be used in the Far North regions for indoor lighting

along with compensation for ultraviolet deficiency [4]. Another advantage of lamps under consideration is that, at high working pressures of cesium vapor ($P_{Cs} \sim 100$ Torr), the surface of the electrodes that are usually made of thoriated tungsten, adsorb cesium (in addition to thorium) that contributes to reduction of the work function much more considerably than thorium itself - down to 1.6–1.7 eV [5]. When the lamp is powered with alternating-polarity pulses (to maintain approximately the same thermal state of both electrodes), both of them are heated up to the temperatures of about 1200–1500 K, which is quite enough for ensuring the working pulse

currents of 50–100 A due to thermal emission, without the formation of erosive cathode spots. This operation mode of electrodes allows expecting long service lives of cesium lamps if the relevant electronic start equipment (ESE) will generate not only operating high-current pulses (like it was during its prototype tests [3]) but also ensure pre-heating of the discharge volume in the glow discharge mode upon lamp turning-on. As soon as the proper temperature of electrodes and "cold point" of the discharge tube (burner) that determines the cesium vapor pressure are reached, the lamp power circuit shall switch over to the mode of operating pulses delivery. Obviously, designing of such ESE firstly requires clarifying specific features of glow discharge ignition and development for "cold" lamps having a room temperature. This is the task of this work.

Experiment procedure

The heating was researched using two lamps with burners of different sizes. One lamp was a laboratory model where the discharge tube was placed in a pumped quartz tube with electrodes led out through rubber seals. The effective volume of the lamp was pumped using a backing vacuum pump with a nitrogen trap up to reach the pressure of $\sim 10^{-1}$ ⁴ torr. The discharge tube (see the photo in Fig. 1) made of monocrystal sapphire had 2r = 11 mm.internal diameter The experimental design included identical wire electrodes made of thoriated tungsten and wound over the core that had the working surface area of 1 cm². The distance between electrodes in this specimens was L = 35 mm(hereinafter burner 11/35).

The second lamp under research was single-capped, fit with an evacuated bulb and a much smaller burner: 2r = 5 mm, L = 22 mm (hereinafter burner 5/22), with the working surface area of its electrodes

equaling to $\sim 0.25 \text{ cm}^2$. External heating using a Nichrome helix could be carried out on the sealed tube. In both cases the burning gas is xenon which pressure at the room was $P_{Xe} = 20 \text{ Torr}$, temperature corresponds to the atom concentration of $N_{\rm Xe} \approx 6 \times 10^{17} \, {\rm cm}^{-3}$. At the temperature of 20 °C, the equilibrium of cesium vapor pressure over its liquid phase is very low - $P_{\rm Cs} \sim 3 \times 10^{-7} \text{ torr } (N_{\rm Cs} = \sim 10^{9 \text{ cm}-3}).$ For this reason, during heating, P_{Cs} is changing within very wide range, up to 1 torr ($N_{\rm Cs} = 10^{16} \, {\rm cm}^{-3}$) at the burner temperature of ~ 600 K, though cesium in the discharge remains a small, easily ionized additive.

The experiment procedure was made as close as possible to the actual operating conditions of ESE. The regulated AC mains voltage was supplied via the step-up transformer to the lamp connected to the line comprising the in-series active and inductive ballasts and a current shunt. In its turn, the voltage from the lamp was supplied to the horizontal deflecting plates of the oscilloscope while the voltage from the current shunt was supplied to the vertical enabling plates, thus the continuous monitoring of the lamp's current-voltage characteristic on the screen. To research the heating, the ballast resistance was set to the limiting the discharge immediately after ignition to the level under 1 A thus preventing an arc with an erosive cathode spot. After that the line voltage was supplied to the lamp and smoothly (but fast enough to minimize heating of the cesium film condensing on the internal wall of the discharge tube upon lamp switching-off [6]) until the moment when the discharge glow appears in the interelectrode space. The amplitude of the voltage supplied at this moment was registered as the voltage of discharge ignition in the cold lamp, and was then increased so that to ensure the desired initial heating current. Increasing this current and switching over to the conditions of abnormal glow discharge was supposed to allow determining the maximum permissible currents and voltages at which cathode spots do not develop yet.

Results of measurements and discussion

Fig. 1 and 2 show the discharge evolution while the lamp with burner 11/35 was being heated, that is the photos of the discharge glow and family of dynamic current-voltage characteristics. As can be seen in Fig. 1, the glowing pattern of the discharge after ignition and during the entire heating is really typical for the glow discharge, which means a distinct positive column with a brighter discharge channel of the diameter determined by the tie to the electrodes and an intensive white cathode glow. The thickness of the latter was significantly decreasing as the burner temperature was growing and, as a result, the cesium vapor pressure was increasing. The current-voltage characteristics of the lamp have symmetrical (Fig. 2) two parts corresponding to the positive and negative semiperiods of the heating voltage, each consisting of two branches: discharge branch (which is the actual current-voltage characteristic of the discharge) with the current growing so fast that is can be considered almosxyt vertical, and the preignition one. The slope of the pre-ignition branch is similar for the positive and negative branches of the current-voltage characteristic and is determined by resistance of the cesium film adsorbed on the discharge tube surface (its thicker, nontransparent part can be well seen on photos, Fig. 1). Both discharge branches are almost similar, and their minor difference is likely to be caused by the difference in design of electrode assemblies and dissimilar heat removal via lead wires. They could be regarded as the starting sections of also virtually vertical currentvoltage characteristic of the normal mode of the usual glow discharge while the ignited

discharge – as the glow discharge in xenon. However, such interpretation comes at odds with the relatively high discharge currents at the vertical branch end of the current-voltage characteristic, associated low voltages and, which is the most important, unproductive attempts to change over to the abnormal mode.

Actually, the maximum current on the characteristics in Fig. 2 is 0.08 A. If we evaluate the area of cathode glow contact with the electrode by the type of cathode glow, then this area shown in the first two photos corresponds to the end surface of the niobium bushing $\sim 1 \text{ cm}^2$, and therefore the normal current density reduced to pressure $j_n/P_{\rm Xe}^2$ is ~ 200 μ A/Torr². This exceeds by an order of magnitude the same parameter of the glow discharge in pure xenon (16 µA/Torr² [7]). But if discharge branches remained vertical until the currents $\sim 1 A$, when switching over to the mode of abnormal glow discharge was attempted, the difference becomes as high as two orders of magnitude. The difference of several times is also observed between the normal voltage of the glow discharge, which, in xenon, is equal to 306 V, and in cesium – to 340 V [7], and the vertical branch voltage, which is as early as during the first seconds of heating (for the yet cold lamp) proves to be much lower $\sim 50 \text{ V}$ and remains virtually unchanged during heating (Fig. 2). Such significant difference proved the fact that, even at minimum concentrations of cesium atoms, the unusual discharge is ignited in the Xe–Cs system.

The changing pattern of current-voltage characteristic and discharge glow configuration were reproduced similarly during heating of the sealed tube with a much smaller burner sized 5/22, the research results of which are shown in Fig. 3. The current-voltage characteristic corresponding to the initial heating stage (photo a1) was likely to have two symmetric discharge branches at virtually the same voltage of 50 V.

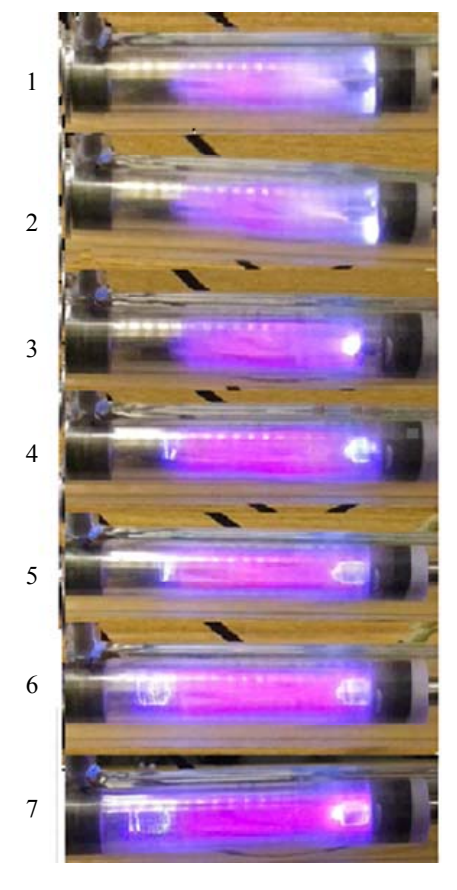
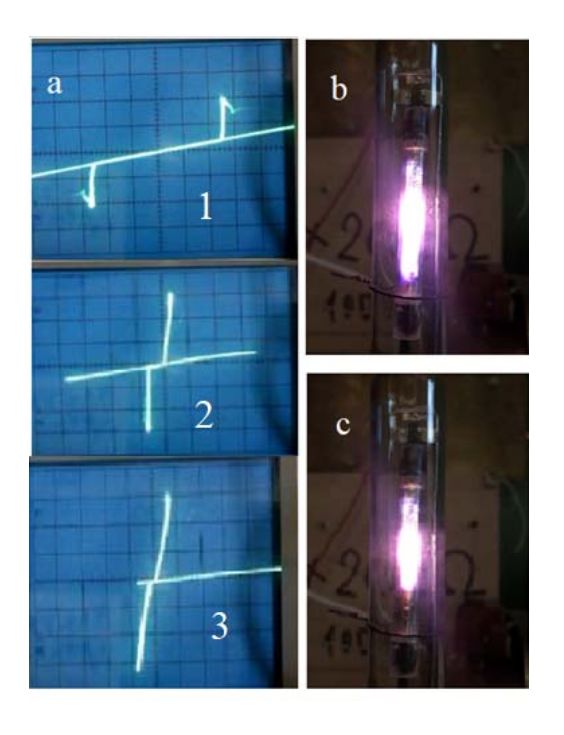


Fig. 1. Evolution of discharge glow during heating of the lamp with burner 11/35. Time after breakdown 1 – 12 s; 2 – 16 s; 3 – 1 min.; 4 – 1 min. 25 s; 5 – 2 min. 14 s; 6 – 3 min.; 7 – 4 min. After that the glow does not change for up to 10 min.



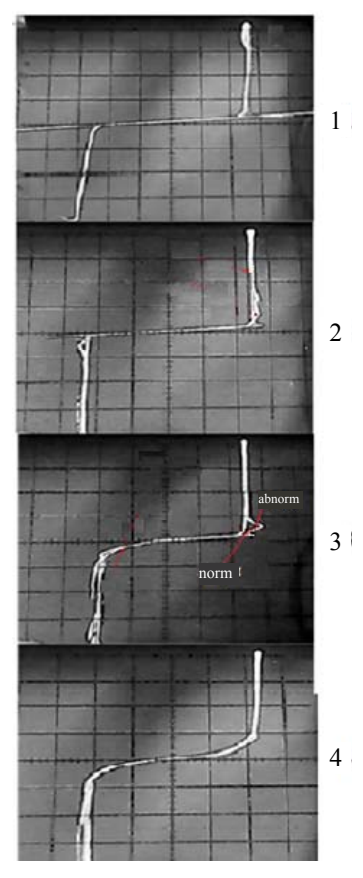


Fig. 2. Change of lamp's current-voltage characteristic during heating. Scale: x = 20 V/div., y = 50 mA/div., zero at the center of the coordinate axes on the screen. t: 1-1 s; 2-1.5 min.; 3-2 min.; 4-3 min., after that the current-voltage characteristic does not change for up to 10 min.

Fig. 3. Evolution of the current-voltage characteristic during heating of the lamp with burner 5/22: 1 – 3 min.; 2 – 7 min.; 3 – 8 min. 30 s from the start of heating. Scale: 1 – 20 V/div and 100 mA/div; 2, 3 – 100 V/div and 100 mA/div

These characteristics agree with the symmetric discharge glow (photo b1) when the cathode glow envelops both electrodes almost similarly. The initial heating current in this mode was noticeably higher and equaled to 0.15 A, increasing up to 0.32 A by the end of this process, which is 4 times as high than in the case shown in Fig. 1. Since the diameter of the positive column's discharge channel, which is associated with electrode sizes, is ~ 2.5 times smaller for burner 5/22, the maximum current density and, therefore, the plasma concentration in the column is approximately 20 times higher for the mode shown in Fig. 3. The high concentration of ions explains the white-pink color of the glow this burner. discharge in The concentration of cesium ions in this discharge state seems to be already high enough for contribute recombination continua to significantly to the radiation of the positive column plasma.

The most important thing when heating of burner 5/22 was that increase of the heating current along with the relatively small burner size, which allowed to increase the electrodes temperature and cesium pressure to the value at which the discharge was able to change over to the arc mode, with the burner voltage dropping from 50 V to several volts and the discharge branch of the currentvoltage characteristic developing a noticeable slope. The processes that could be observed visually took place at first with the first electrode (Fig. 3, 2a, 2b). Here the cathode glow enveloping the electrode changed to the end tie to the electrode. Since there was no bright point (cathode spot), the tie was mostly diffuse, that is the cathode current was maintained by the thermal emission of heated electrode. Breakdown was immediately followed by arcing: at first for one electrode. for both (current-voltage characteristic 3a in Fig. 3). For burner 5/22, the end surface area of the niobium bushing ~ was 0.25 cm², and the reduced normal current density $j_n / P_{xe}^2 \sim \text{was } 2000 \, \mu\text{A/torr}^2 \text{ at}$

the end of the vertical section, becoming an order of magnitude higher when attempting to change over to the abnormal mode.

Since the current-voltage characteristic of the discharge almost does not change during heating of the lamp when the concentration of Cs atoms grows by several orders of magnitude, the above specific features of the discharge in xenon with cesium shall be mainly related to the change in emission characteristics of electrodes as they adsorb Cs atoms. For the cesium adsorbed coating to be formed on the surface of electrodes, quite minimum concentrations of Cs atoms in the burner volume suffice, especially that coatings are quite stable at a low temperature of the adsorbing surface (about the liquid-phase temperature of cesium and lower). Whereas decrease of the work function down to $\phi_k \approx 1.7 \text{ eV}$ shall result in increase of both ion-electron and photoelectric emissions.

When energies of bombarding ions are low $\varepsilon_i < \sim 1$ keV, the emission occurs based on their ionization energy E_i [8]. Ion is neutralized on the surface by the metal's conduction electron with energy consumed ϕ_k and with an excited atom formed, after which the remaining energy $E_i - \phi_k$ is transferred to another conduction electron as the atom is deexcited. And if $E_i - \phi_k > \phi_k$, this electron has a probability of exiting the metal. This higher the difference, the higher such probability is. Similarly, an excited atom with excitation energy $E^* > \phi_k$ getting on the metal surface is able to cause the electron emission.

According to [8], as tungsten is being bombarded, the ion-electron emission factor for ion Xe^+ ($E_i = 12.3 \text{ eV}$) is virtually constant for the entire range of low ε_i and not high - $\Upsilon_i = 0.02$, because for polycrystalline W $\phi_k \approx 4.7 \text{ eV}$, and the exceedance $E_i - 2\phi_k = 2.9 \text{ eV}$ is low. But if Cs atoms are adsorbed on the surface and $\phi_k = 1.7 \text{ eV}$, $E_i - 2\phi_k = 8.9 \text{ eV}$, and Υ_i shall increase significantly. According to empirical dependence $\Upsilon_i(E_i - 2\phi_k)$ given in [8], we will

have Υ_i (9 eV) \approx 0.12. Therefore, during adsorption of cesium on the electrodes, the ion-electron emission for xenon shall increase considerably due to Xe+ ions. While for Cs⁺ ions $E_i - 2\phi_k = 3.89 - 3.4 \approx 0.5 \text{ eV}$ is very low. Correspondingly, both Υ_i and their contribution to the electron emission shall be as well. This explains the weak of dependence the current-voltage characteristic on the cesium pressure during lamp heating, although Cs atoms are easily ionized due to the Penning process.

But if ionization is the main source of cathode electrons, even its strong growth during adsorption of cesium on the electrodes surface cannot explain why the currentvoltage characteristic is vertical and abnormal mode does not develop. Indeed, in this case the discharge current is carried by ions both at small and at large Yi in the high-field region. The difference is that in the first case the generation of one electron requires many ionizations in the high-field region while in the second case fewer ionizations required. For this reason, the higher density of the ion current is required in this region to increase the discharge current after the point of the normal mode changing to the abnormal one at any Y_i . The positive space charge and potential drop along the high-field region will increase correspondingly to extent increased ion current. This determines the voltage growth as the current on the currentvoltage characteristic of the discharge's abnormal mode is growing no matter how high Υ is. These considerations are confirmed by the fact that Yi is almost the same for argon with pure tungsten as for W-Xe+Cs, even reaching 0.2–0.3 for Ne and He, but the glow discharge for all these pure gases has a clearly defined anomalous section of the current-voltage characteristic.

Whereas the second factor, which is the increase in photoemission when there is an adsorbed layer of Cs on the electrodes surface, can be, in fact, the reason for the absence of the discharge's abnormal mode in

Xe+Cs mixture. But this requires the assuming photoemission growth to the value, at which this mechanism becomes the main one ensuring the electron current from the cathode. In this case the current in the highfield region is carried by the electrons emitted by the cathode, and to increase the discharge current, the same cathode's electron emission is required. But this will require the growing number of excitations of Xe atoms followed by the glow rather than the increase in the number of ionizations. The discharge structure remains while parameters change completely, Due to the fact that no intensive ionization is required in the cathode layer, the cathode voltage drops from 300 V to 50 V. Such insignificant drop is likely to result in significant decrease of the electric field strength near the cathode, which means that the energy of accelerating electrons will be mostly consumed for excitation of Xe atoms and generation of resonance radiation that ensures the emission of electrons from the cathode rather than their ionization. But since the cathode drop still noticeably exceeds the ionization potential of the Xe atom, the low current is maintained. When ion contribution to the discharge current is negligibly small, it is quite likely that it will not only compensate for the space charge of the electron current, but also retain a small positive charge in the high-field region, since the contribution of the Xe⁺ ion to the space charge in $(M/m)^{1/2}$ is ≈ 500 times greater than that of the electron. In this case, as the discharge current grows, for the extra electric current to pass in the cathode region, the increase in the voltage drop therein will not be required, and, at the first approximation, the radiation intensity that determines the current of the electron emission from the cathode will be proportional to this current. But this condition is exactly the condition for the current-voltage characteristic to run vertically – additional quanta required to generate additional electrons are produced by these electrons due to the increase in the

energy entering the discharge as the current grows.

According to the experiment during which the electrode was illuminated by the LED light and the maximum current on the current-voltage characteristic was one and a half times as high, photoemission is the main contributor to the electric current from the cathode in the discharge under study. And there are reasons for it. First, due to the reduced work function of the electrodes during cesium adsorption, photoemission covers virtually the entire visible radiation spectrum of the cathode layer. Second, formation of W-Th-Cs structures significantly increase the work function similarly to the photomultiplier. Third, the cathode layer radiation has an especially structure which spectral is especially beneficial for the photoemission. On the highfield segment, resonance lines of the Xe atom $(\lambda = 119, 125, 130 \text{ and } 147 \text{ nm})$ must be the first to be excited, since their photon energy is higher than not only the work function of the monoatomic cesium film adsorbed tungsten (~ 1.7 eV) but also the Cs atom ionization (3.89 eV). In the positive column of the regular glow discharge in xenon, resonance lines carry away about a half of the radiation energy [9]; on the high-field segment of the cathode layer, they must be the first to be excited because their share in its radiation shall be at least the same. Such significant decrease of ϕ_k shall increase the photoemission in this spectrum region drastically. This is the main factor. The combination of the intensive resonance radiation of xenon atoms with the low work function of cesium coatings on the electrodes determines the specific features of the glow discharge in the Xe-Cs mixture. These specific features do not exist separately in xenon or cesium. Finally, the flow of excited Xe atoms to the cathode gives rise to the same emission of electrodes and is equivalent to photoemission.

Photoemission and impact of the natural external illumination can be also the factors that cause the drop of ignition voltage U_{ign} observed in cold lamps. This value was equal to 460 V for burner 11/35 U_{ign} . For it $P_{\text{Xe}}L = 70 \text{ Torr} \cdot \text{cm}$ it corresponds $U_{\text{ign}} = 2000 \text{ V}$ on the xenon-specific Paschen curve, which is 4 times is high. For the lamp with burner 5/22, $P_{Xe}L = 45 \text{ Torr} \cdot \text{cm}$, with $U_{\text{ign}} = 1400 \text{ V}$ derived from the Paschen curve, which is 3 times as high as 500 V obtained experimentally. Such significant drop of the ignition voltage means that high photoemission factors and presence of even small cesium amounts change the avalanchetype mechanism of breakdown in pure xenon drastically.

From a practical outlook, low ignition and burning voltages of the photoemission discharge make it much easier to design preheating ESE for PPD lamps, while due to relatively high currents the temperature of electrodes shall grow quite fast. The only thing that requires confirmation is that the transition to the arc mode being observed corresponds to the diffuse tie to the electrodes. In this case the cathode sputtering of the electrodes is reduced almost to nothing, because the contribution of the ion-electron emission to the electron current from the cathode, which seems to be very insignificant, while the cathode drop of the voltage is several times lower.

Conclusion

Research of the discharge ignition with cold electrodes in cesium illuminating lamps revealed the unusual "high-current" form of the glow discharge that is formed and burns at considerably lower voltages and at the currents that are 1–2 orders of magnitude higher than that of the regular glow discharge in pure xenon or cesium. Essential characteristics of such high-current glow

discharge were obtained, a number of its patterns were established preliminarily. The specific features of a high-current glow discharge in xenon with cesium added are supposed to be caused by the formation of W-Th-Cs film structures on the electrodes with the low work function and high photoemission in relation to the short-wave resonance radiation of xenon atoms in the layer. The high-current cathode discharge mode is extremely favourable for designing ESE for cesium PPD preheated lamps, since it prevents erosion-induced cathode spots that shorten the service life of the light source. From the standpoint of both physics of gas discharge and practical significance, further, more detailed, research of the high-current glow discharge in steadystate modes and, first of all, spectroscopic study of the phenomena described herein, is of great interest.

The authors are thankful to their colleagues A. A. Bogdanov and I. I. Stolyarov for valuable and useful discussions.

REFERENCES

- 1. Baksht F. G. and Lapshin V. F., Usp. Prikl. Fiz. (Advances in Applied Physics) **5** (6), 525 (2017) [in Russian].
- 2. Gavrish S. V., Kaplan V. B., Martsinovsky A. M. and Stolyarov I. I., Applied Physics, No. 5, 78 (2019) [in Russian].
- 3. Bogdanov A. A., Gavrish S. V., Koval' V. V., Martsinovsky A. M. and Stolyarov I. I., Applied Physics, No. 6, 16 (2020) [in Russian].
- 4. Bogdanov A. A., Gavrish S. V., Martsinovsky A. M. and Stolyarov I. I., University Journal. Physics and Mathematics **16** (1.1), 369 (2023).
- 5. Taylor J. B. and Languir I., Phys. Rev. **44**, 423 (1933).
- 6. Gavrish S. V., Applied Physics, No. 6, 84 (2018) [in Russian].
- 7. Rokhlin G. N., Razryadnye istochniki sveta. Moscow-Leningrad, Energoatomizdat, 1960, p. 230.
- 8. Djbretsov L. N. and Gooojunjva M. V., Emission Electronic. Moscow, Nauka, 1966 [in Russian].
- 9. Grigorjan G. M., Demjanov A. V., Djatko N. A. and Kochetov I. V., Fizika Plasmy **47**, 562 (2021) [in Russian].
- 10. Bohan P. A. and Sorokin A. R., J. Tech. Phys. **55** (5), 88 (1985) [in Russian].

About authors

Artemy Markovich Marcinovsky, Senior Researcher, Candidate of Physical and Mathematical Sciences, loffe Physico-Technical Institute RAS (194021, Russia, St. Petersburg, Ulitsa Polytekhnicheskaya, 26). E-mail: amartsinovsky@gmail.com Author ID 20607

Sergey Viktorovich Gavrish, Dept. Head, Doctor of Technical Sciences, Scientific and Industrial Enterprise "Melitta", LLC (117997, Russia, Moscow, Ulitsa Miklukho-Maklaya, 16/10). E-mail: svgavr@list.ru SPIN code 3089-4957, Author ID 503331

Dmitry Gennadievich Korenyugin, Senior Lecturer, Peter the Great St. Petersburg Polytechnic University (195251, Russia, Saint Petersburg, Ulitsa Polytekhnicheskaya, 29). E-mail: polarisdk@mail.ru SPIN code 9098-5391, Author ID 536530

Anton Sergeyevich Guslin, student, Peter the Great St. Petersburg Polytechnic University (195251, Russia, Saint Petersburg, Ulitsa Polytekhnicheskaya, 29)

Vladimir Nikolayevich Kuzin, student, Peter the Great St. Petersburg Polytechnic University (195251, Russia, Saint Petersburg, Ulitsa Polytekhnicheskaya, 29)

PHYSICAL SCIENCE OF MATERIALS

UDC 53.06 PACS: 87.50.wp, 78.70.Ps

EDN: UIVSCB

Optical properties of calcium tungstate doped with various lanthanides (Pr, Nd, Eu, Ce, Sm)

© P. D. Kuznetsova*, E. A. Mukhanova, K. K. Volik, I. A. Pankin, A.V. Soldatov

International Research Institute of Smart Materials of the Southern Federal University,
Rostov-on-Don, 344090 Russia
* E-mail: pkuznecova@sfedu.ru

Received 29.09.2024; revised 09.01.2025; accepted 07.04.2025 Scientific specialty code: 1.3.8

The impact of doping with rare earth elements, in particular with triple-charged lanthanides Ln^{3+} (Ln = Pr, Nd, Eu, Ce, Sm), on the luminescent properties of calcium tungstate featuring a scheelite structure produced by the microfluidic method was studied. The results of X-ray excited optical luminescence (XEOL) allow stating that doping with europium leads to the most intense luminescence of scheelite. A quantitative analysis of the elemental composition of scheelite samples obtained by the microfluidic method was carried out using the X-ray fluorescence analysis method, as well as a qualitative analysis of the X-ray absorption spectra (XANES) near absorption L_3 -edge of W for Eu-substituted tungstate, as a sample providing the highest fluorescence yield.

Keywords: XEOL; scintillator; photodynamic therapy; XANES; microfluidics.

DOI: 10.51368/1996-0948-2025-2-84-89

Introduction

Photodynamic therapy (PDT) is the modern approach in cancer treatment which uses a photosensitiser which, when excited, usually in the optical range, is able to generate the reactive oxygen species (ROS) which, in turn, are able to locally cause the apoptosis of pathogenic cells and tissues where photosensitiser molecules are concentrated [1, 2]. The PDT mechanism can potentially be considered as an effective non-invasive method for treatment of deep-seated tumors, provided the systems can be excited

using the penetrating ionizing radiation, for example, in the gamma or X-ray range. This version of the approach is known as the X-ray photodynamic therapy. However, although the first works on the application of X-ray radiation for exciting the photosensitiser and subsequent generation of ROS were published as long as a half a century ago [3], the current implementation of this technique on the widespread requires basis develop biocompatible nanoparticles comprising heavy elements and featuring the highly efficient absorption of ionizing radiation and subsequent transfer the energy to

photosensitiser molecules [4]. When the highly efficient energy transfer is achieved, this mechanism can lead to local death of cancer cells even at low radiation load rates.

Introduction of rare earth elements (REE) such as lanthanides into the structure. which exhibit scintillation properties due to electronic transitions within f-orbitals [5, 6]. allows creating more efficient phosphors, while variability of dopant types and concentrations allows shifting emission spectrum density of phosphors [7], thereby allowing to use a larger number of photosensitizers. Calcium tungstate with a scheelite structure, which is widely used in medical imaging studies and may find application in theranostics, has a promising potential as a host lattice [8]. Modern synthesis methods, such as a microfluidic technique, allow producing more defective structures, including those with a distorted without crystal lattice. long-term treatment.

The findings of the optical and structural analysis of the calcium tungstate's defective structures obtained during the research, which can be used to form nanocomposites for X-ray photodynamic therapy, are provided herein.

Reagents

Doped scheelite was produced using sodium tungstate dihydrate Na₂WO₄×2H₂O (M.W.: 329.86 g/mol, 98 %, Sisco Research Laboratories Pvt. Ltd.), anhydrous calcium chloride CaCl₂ (M.W.: 110.98 g/mol, ≥93 %, europium(III) Sigma-Aldrich), chloride hexahydrate EuCl₃×6H₂O (M.W.: 446.07 g/mol, 99.99 %, REacton), neodymium(III) chloride hexahydrate NdCl₃×6H₂O (M.W.: 358.69 g/mol, 99.99 %, REacton), anhydrous samarium(III) chloride SmCl₃ (M.W.: 256.72 g/mol, 99.9 %, Alfa Aesar), cerium(III) chloride anhydrous CeCl₃ (M.W.: 246.48 g/mol, 99.5 %, Alfa Aesar), praseodymium(III) chloride hexahydrate PrCl₃×6H₂O (M.W.: 355.36 g/mol, 99.99 %, REacton).

Production procedure

To produce materials with the theoretical formula $Ca_{0.925}Ln_{0.05}WO_{4}$ $(Ln^{3+} = Pr^{3+}, Nd^{3+}, Eu^{3+}, Ce^{3+}, Sm^{3+})$ using the microfluidic method, two solutions were prepared: solution A contained 0.3 mol/L of sodium tungstate dihydrate, solution B contained 0.278 mol/L of anhydrous calcium chloride and 0.015 mol/L of lanthanide salt. The solutions were put in separate syringes and secured in high-precision pumps in the microfluidic platform. After that the flows of solutions A and B were mixed through a Yshaped connector and the resulting mixture was fed through a polyethylene terephthalate (PET) tube with an internal diameter of 1.0 mm and a length of 1 m at different rates: the A:B rate ratio was either 1:1 or 1:4, as in [9]. The flow rates were set equaling to 5 µl/s for solution A and to 5 µl/s or 20 µl/s for solution B. The white precipitate formed during the reaction was collected in a separate collecting tube, precipitated by centrifuging at 10,000 rpm for 10 minutes, decanted, washed with bidistilled water three times, and dried at 60 °C.

Equipment

X-ray patterns were obtained by means of Bruker D2 Phaser desk-top X-ray diffractometer (Germany) at 30 kV, 10 mA Cu K_{α} radiation using a low-background cell. The range is $2\theta - 10^{\circ}$ – 60° , the step is 0.01° . The elemental composition was analyzed using Bruker M4 TORNADO X-ray

microfluorometer (Germany). The obtained quantitative values of the elemental composition were averaged based on results of measurement at 20 points on the sample surface with measurement duration of 10 s per point. X-ray excited optical luminescence XEOL was measured using a special bench designed on the basis of commercial Cary Eclipse fluorimeter (Australia) and RAP90-5 X-ray tube and previously described in [10].

The emission slit width of the fluorimeter was 10 nm, and the exposure time was 0.1 s per point of the recorded XEOL signal. The operating parameters of the X-ray tube were 35 kV and 1.6 mA. X-ray absorption spectra in the XANES (X-ray

absorption near edge structure) region were measured by the structural material engineering station of the Kurchatov synchrotron radiation source [11] using the silicon Si(311) monochromator for changing the energy of incident X-ray radiation on the sample.

Findings and discussion

According to the X-ray phase analysis data (Fig. 1), the samples produced by the microfluidic method are single-phase, and the X-ray pattern peaks correspond to the data of PDF-2 record with number 00-077-2236, CaWO₄ of the scheelite structure.

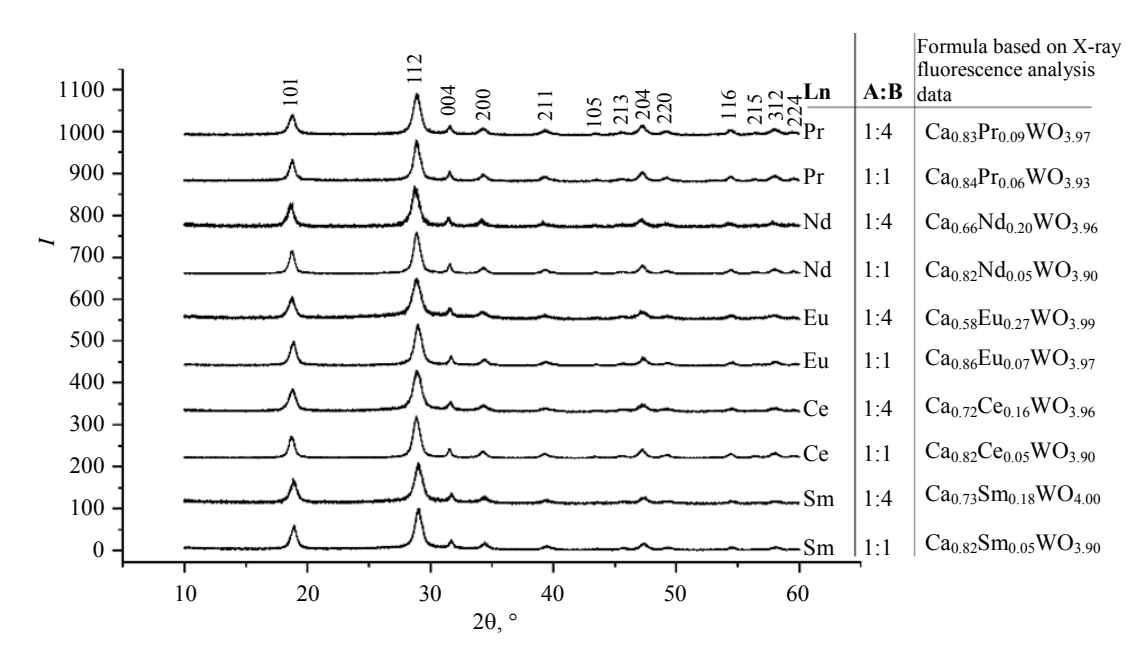


Fig. 1. X-ray patterns of CaWO₄:Ln samples where Ln = Pr, Nd, Eu, Ce, Sm, obtained by the microfluidic method with different ratios of flow rates: A (Na₂WO₄×2H₂O) to B (CaCl₂/LnCl₃)

The elemental composition of the materials was determined using X-ray fluorescence analysis. The atomic percentage was recalculated based on the tungsten (W) content assumed to be equal to one. In this way, quantitative values of the content were obtained for calcium (Ca) and lanthanides

(Pr, Nd, Eu, Ce, Sm). The quantitative content of oxygen atoms was calculated based on the electrical neutrality principle. The stoichiometric formulas of the samples under study are given in Fig. 1. A degree of calcium substitution by the Ln³⁺ cation has been found dependent on the ration of flow rates. As can

be seen from the findings of the quantitative elemental analysis, the degree of substitution varies between 5 % and 7 % at the similar flow rates for all dopants. But as the flow rate of mixture B increases up to $20 \,\mu\text{l/s}$, the degree of substitution of Ca ions rare earth elements ions is seen to grow considerably, by $16-27 \,\%$, except for Pr, where the increase of flow B rate results in the degree of substitution of 9 %.

The samples containing Eu as a dopant were taken for XANES. These samples were prepared as powders and densely applied on the kapton. To calibrate the energy scale of the recorded X-ray absorption spectra, a reference sample – a tungsten oxide (WO₃) pellet placed between the second and third ionization chambers – was analyzed simultaneously. Normalization, calibration of the energy position and averaging of several measurement results were carried using DEMETER software [12].

Normalized XANES spectra obtained beyond L_3 -edge of tungsten are shown in The more intense absorption Fig. 2. maximum observed in the CaWO₄:Eu sample can be explained by the higher density of free states on the d- or d-p-hybridized tungsten shells as compared to those in the tungstencontaining precursor. Peak I located at 10213 eV, is a "white line" corresponding to the oxidation state of tungsten +6. Peak II corresponds the tetrahedron-shaped to environment of tungsten for CaWO₄:Eu, and as for Na₂WO₄×2H₂O precursor, octahedral complexes are most likely to form due to the presence of crystalline water, which manifests itself in splitting of d-orbitals into two sublevels: e_g at 10230 eV and t 2g at 10220 eV. According the **XANES** spectroscopy data, tungsten atoms in the sample obtained have a tetragonal coordination corresponding to the scheelitetype structure.

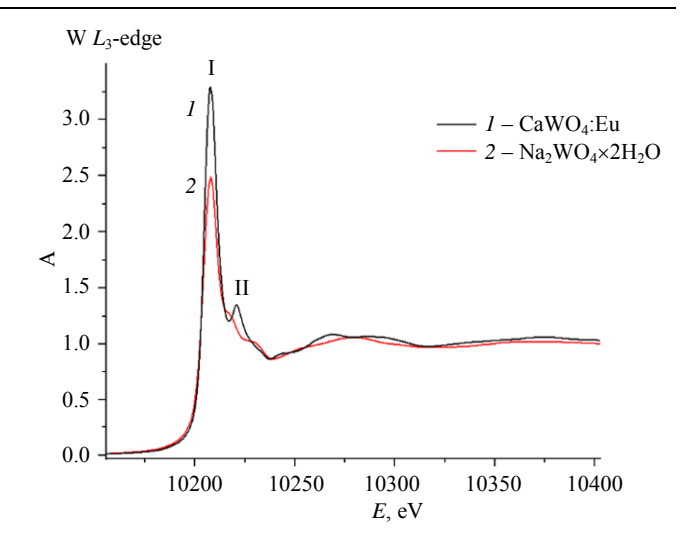


Fig. 2. XANES spectra beyond L_3 -edge of tungsten for $CaWO_4$:Eu (A:B=1:1) as compared to tungsten-containing precursor Na_2WO_4 ×2 H_2O , where A is normalized absorption

According to the literature data, pure calcium tungstate in the XEOL spectra exhibits a wide peak ${}^{1}T_{2} \rightarrow {}^{1}A_{1}$ at 450 nm due to the Jahn-Teller effect, which affects the degenerated excited states of the tetrahedron WO_4^{2-} [13]. As shown in Fig. 3, doping with intensifies the initial lanthanides luminescence of calcium tungstate and transfers the emission into the visible range, thus allowing to use a wide range of sensitizers. Adding Eu³⁺ and Nd³⁺ ions provides the maximum intensification of the initial scintillation of calcium tungstate around 450 nm, since ¹T₂ energy levels of complex WO₄²⁻ resonate with the lanthanide transitions 4f→4f. Simultaneously, Sm³⁺ and Ce³⁺ ions effectively capture the excited state energy of the host matrix due to closely spaced energy levels, which leads to the nonradiative relaxation and quenching of luminescence. Whereas the high sensitivity of lanthanides' emission characteristics towards the crystalline environment of the host lattice applied to praseodymium results in competition between the intrinsic luminescence of Pr³⁺ ions and WO₄²⁻ states due to nonresonant interaction [14].

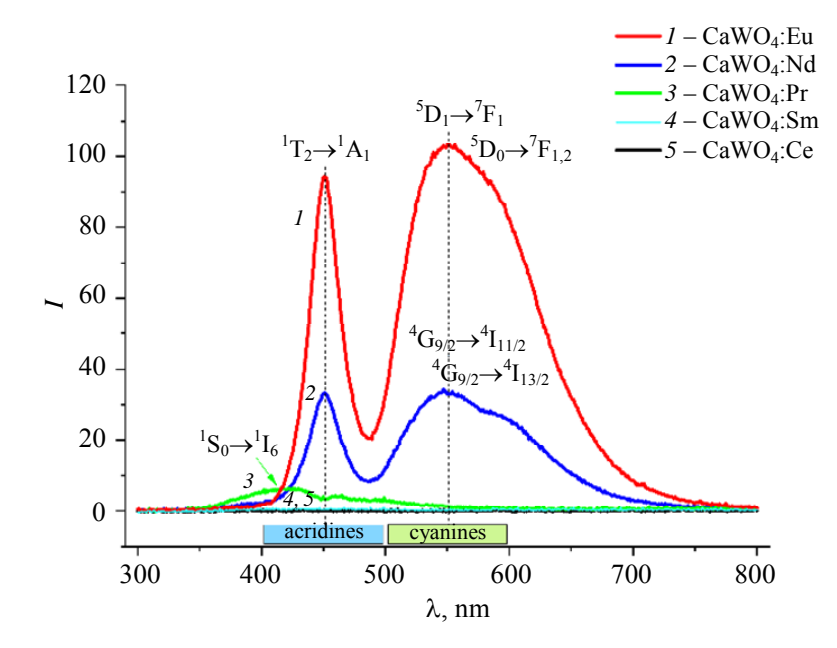


Fig. 3. Spectra of XEOL samples obtained at similar rates of flows A (Na₂WO₄×2H₂O) and B (CaCl₂/LnCl₃)

Conclusion

- The microfluidic method is effective for low-temperature doping of scheelite using lanthanides.
- Four-fold increase of the rate of the flow containing doping elements results in the exponential growth of the Ca→Ln substitution percentage. The maximum substituent concentration amounted to 27% (for the Eu substituted sample).
- The most effective substitutes of calcium in scheelite, which contribute to a significant increase of the radiation intensity when irradiated in the X-ray range, are europium (+3)and neodymium Praseodymium (+3) exhibits the inherent luminescence, but suppresses the scintillation of the tungstate ion. Doping with samarium (+3) and cerium (+3) results in complete quenching of the X-ray luminescent properties.
- The obtained X-ray phosphors can be potentially used for X-ray PDT combined with photosensitizers of the acridine group (adsorption maximum of 400–500 nm) and cyanine group (adsorption maximum of 500–600 nm).

The study was carried out with financial support from the Ministry of Science and Higher Education of the Russian Federation within the framework of the state assignment in the field of scientific activity No. FENW-2023-0019.

REFERENCES

- 1. Diamond I., Mcdonagh A., Wilson C., Granelli S., Nielsen S. and Jaenicke R., Lancet **300** (7788), 1175–1177 (1972).
- 2. Dolmans D., Fukumura D. and Jain R., Nat. Rev. Cancer. **3** (5), 380–387 (2003).
- 3. Dougherty T. J., Grindey G. B., Fiel R., Weishaupt K. R. and Boyle D. G., JNCI **55** (1), 115–121 (1975).
- 4. Zhang T., Zheng H., Zhang F., Chu C., Liao T., Xie L., Liu G. and Cai W., J. Lumin **261**, 119862 (2023).
- 5. Maksimchuk P. O., Hubenko K. O., Bespalova I. I., Sorokin A. V., Borovoy I. A. and Yefimova S. L., J. Mol. Liq. **330**, 14–16 (2021).
- 6. Luo Z., Mao D., Li X., Luo J., Gong C. and Liu X., Coord. Chem. Rev. **508**, 215773 (2024).
- 7. Gu C., Wang Z., Pan Y., Zhu S. and Gu Z., Advanced Materials **35** (1), (2023).
- 8. Lei L., Wang Y., Kuzmin A., Hua Y., Zhao J., Xu S. and Prasad P. N., eLight **2** (1), 17 (2022).
- 9. Chen Z., Song Q., Ni L., Jiang J. and Yu Y., J. Environ. Chem. Eng. **9** (6), 106528 (2021).

- 10. Medvedev P. V., Pankin I. A., Soldatov M. A., Polozhentsev O. E. and Soldatov A. V., Opt. Spectrosc. **130** (6), 409–417 (2022).
- 11. Chernyshov A. A., Veligzhanin A. A. and Zubavichus Y. V., Nucl. Instrum. Methods Phys. Res. A **603** (1–2), 95–98 (2009).
- 12. Ko J. Y. P., Hu Y., Armelao L. and Sham T.-K., J. Phys. Conf. Ser. **190**, 012078 (2009).
- 13. Ravel B. and Newville M., J Synchrotron Radiat. **12** (4), 537–541 (2005).
- 14. Xiang Z., Jiang C., Liu C., Xie J. and Li H., eLight **2** (1), 6 (2022).

About authors

Polina Dmitrievna Kuznetsova, laboratory assistant, International Research Institute of Smart Materials of the Southern Federal University (344090, Russia, Rostov-on-Don, Andrey Sladkov St., 178/24). E-mail: pkuznecova@sfedu.ru SPIN code 9722-8406, Author ID 1288722

Elizaveta Andreevna Mukhanova, Head of the research laboratory, Candidate of Chemical Sciences, International Research Institute of Smart Materials of the Southern Federal University (344090, Russia, Rostovon-Don, Andrey Sladkov St., 178/24). E-mail: kand@sfedu.ru SPIN code 4212-9848, Author ID 223100

Kirill Konstantinovich Volik, laboratory assistant, International Research Institute of Smart Materials of the Southern Federal University (344090, Russia, Rostov-on-Don, Andrey Sladkov St., 178/24). E-mail: kvolik@sfedu.ru SPIN code 2535-0515, Author ID 1288534

Ilya Andreevich Pankin, Head of the research laboratory, Candidate of Physics and Mathematics, International Research Institute of Smart Materials of the Southern Federal University (344090, Russia, Rostovon-Don, Andrey Sladkov St., 178/24). E-mail: pankin@sfedu.ru SPIN code 3152-7393, Author ID 793405

Alexander Vladimirovich Soldatov, Head of the research group, Doctor of Physics and Mathematics, International Research Institute of Smart Materials of the Southern Federal University (344090, Russia, Rostovon-Don, Andrey Sladkov St., 178/24). E-mail: soldatov@sfedu.ru SPIN code 2132-5994, Author ID 1685

PHYSICAL SCIENCE OF MATERIALS

UDC 534-16 PACS: 62.25.-g

Study of acoustic properties of van der Waals heterostructures containing the WSe₂ monolayer using the hypersonic microscopy

© N. Yu. Frolov*, A. Y. Klokov, A. I. Sharkov, S. N. Nikolaev, M. A. Chernopitsky, S.I. Chentsov, M. V. Pugachev, A. V. Shupletsov, V. S. Krivobok, A. Y. Kuntsevich

Lebedev Physical Institute of the Russian Academy of Sciences, Moscow, 119991 Russia *E-mail: frolil199999@gmail.com

Received 18.10.2024; revised 09.12.2024; accepted 14.04.2025 Scientific specialty code: 1.3.7

Elastic properties of the lavered heterostructure of $Al/hBN/WSe_2$ (monolayer)/ hBN/Al_2O_3 were studied using a picosecond ultrasonic technique. Time dependences of the change in the phase of the reflection coefficient of the sample caused by propagation of the elastic pulse excited by a femtosecond laser were measured during the experiment. A map built to describe the spatial distribution of the modulus of the response Fourier spectrum components for different frequencies allowed to localize the region of the heterostructure containing the WSe₂ monolayer. By means of a mathematical model of the multilayer structure response, the elastic parameters of heterostructure Al/hBN/WSe2(monolayer)/hBN/Al2O3 were estimated, in particular rigidities of layer interfaces.

Keywords: picoacoustics; laser hypersound; mechanical properties; van der Waals heterostructures; monolayer.

DOI: 10.51368/1996-0948-2025-90-96

Introduction

In recent years, the use of van der Waals (VdW) materials in micronanoelectronics has been advancing incrementally. This trend is primarily caused by the wide range of unique properties exhibited such materials. by Forming heterostructures based on such properties significant setting the characteristics of final optical and electronic devices as well as their compact arrangement and higher efficiency [2, 3].

For example, transition metal dichalcogenides (TMDs) that are an advanced platform for atomically thin flexible

optoelectronics [4, 5] have become widely popular. Monochalcogenide compounds are also of great interest for use in visible and near IR photodetectors due to their narrowforbidden band [6]. Graphene is demonstrating its potential as an element of atomically thin tactile sensors [7], acoustic coatings [8], and elements of micro- [9] and nanoelectromechanical [10] systems.

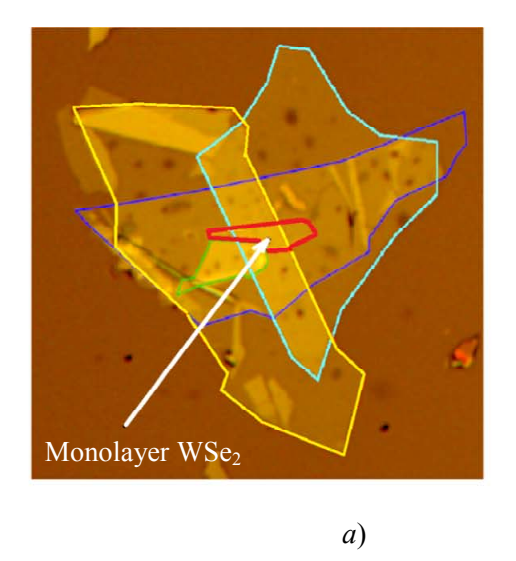
It should be noted that assembling van der Waals heterostructures requires high precision [11], since the performance of such heterostructures is strongly dependent on both the lateral homogeneity of layers themselves and quality of their interfaces influencing the mechanical and acoustic properties of the structure. They, in turn, may have significant influence on the transport of charge carriers and phonons, for which reason such studies are of high priority.

Today, the most effective approach for studying the mechanical and acoustic properties of van der Waals heterostructures is the picosecond acoustics method, where an optically excited short elastic pulse is used as a tool for diagnosing materials. This elastic pulse propagates deeply into the sample and is partially reflected at the interfaces. The coefficient of elastic pulse reflection from the layers interface is also dependent on the quality of contact between the VdW layers [12, 13].

In this paper we focused on studying the acoustic properties of heterostructure Al/hBN/WSe₂(monolayer)/hBN/hBN/Al₂O₃ and its interfaces, as well as the influence of the WSe₂ monolayer on the elastic pulse spectrum characteristics within the heterostructure.

Experiment description

This paper provides the results of studying the heterostructure containing the WSe₂ monolayer encapsulated between thin layers (~12 nm) of hBN (Fig. 1a). hBN layers were produced by peeling off with a Scotch tape on oxidized Si. While the WSe₂ monolayer was produced by the laminating method using gold, which is described in [14]. Then, the heterostructure was assembled on the Al₂O₃ substrate with (001) orientation by dry hot transfer [15] in ambient conditions. A thin Al film (~30 nm thick) sprayed on by electron beam evaporation acted as generator of elastic pulses in the structure upon absorption of laser radiation. The layers were characterized by means of atomic force microscopy during assembly of the heterostructure. The WSe₂ monolayer was identified using Raman scattering spectroscopy and photoluminescence measurements (Fig. 1b) [16].



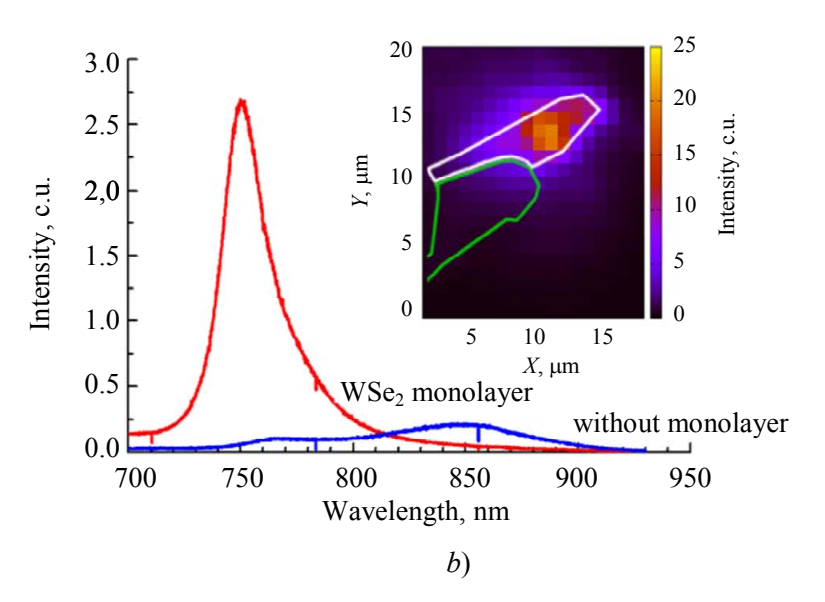


Fig. 1. a) – photo of the structure: the region where the WSe₂ monolayer was located is red, blue, hBN layers are yellow and light blue, WSe₂ layer is green, multilayer Wse₂ is green; b) – photoluminescence spectra of mono- and multilayer WSe₂ at 300 K; the inset shows the spatial map of photoluminescence in the wavelength range of 738–760 nm after excitation at the wavelength of 472 nm

Pulses of coherent phonons in the heterostructure were optically generated and recorded using a two-colour pump-probe setup (Fig. 2), which allowed measuring changes in the complex reflection coefficient

with temporal and spatial resolution. The source of laser radiation was a femtosecond Ti:Sa laser generating pulses of linearly polarized radiation at the wavelength $\lambda = 800 \text{ nm}$ with a duration $\tau_{pulse} = 160 \text{ fs}$ and

repetition frequency of $f = 76 \,\mathrm{MHz}$. The second harmonic laser pulse of the source, when absorbed by aluminum, generated a picosecond elastic pulse that propagated perpendicularly to the surface deeply into the sample and was partially reflected from the heterostructure interfaces. Propagation of the elastic pulse, in turn, caused changes in the sample's reflection coefficient recorded with the second light pulse at the wavelength of the source, which was focused at the same point as the excitation pulse.

The experiment measured the time dynamics of the reflection coefficient phase in different areas of the structure by means of a delay line that allowed changing the time delay of the probing pulse relative to the excitation pulse. Due to use of the Sagnac interferometer the sensitivity of the setup to minor phase changes was increased significantly [17].

The resulting responses were a combination of a high-oscillating part associated with propagation of the elastic pulse in the structure and a slow thermal contribution. After the slow component was substracted, the Fourier spectral analysis of the obtained time responses was performed.

To model the elastic response of the structures, a multilayer one-dimensional model similar to that of [18] was used. The bond between two contacting layers is considered to be ideal (acoustic mismatch) if displacement of two adjacent points belonging to different materials is the same. However, the case of acoustic mismatch is actually often not realized, especially in case of laminate materials, and such contact is considered to be non-ideal.

To take into account the influence of interface nonideality on the elastic response of the system, a "spring" contact model was used in the calculations. Within this model, the contacting layers are linked to each other with weightless springs evenly distributed over the entire contact area.

In this case the equivalent stiffness of these springs η , which is a quantitative

characteristic of the elastic bond of the layers, was one of the key interface parameters in the calculations. The values obtained for the total stiffness of springs and characteristic frequencies of the interfaces under consideration $(f_0 = \eta(Z_1 + Z_2) / 2\pi Z_1 Z_2$, where Z_1 and Z_2 are acoustic impedances of contacting layers) are given in Table 1. Frequency f_0 characterizes the frequency dependence of the elastic wave's reflection coefficient at a non-ideal interface [13]:

$$R_{\text{eff}} = \frac{R - if / f_0}{1 - if / f_0},$$

where $R = (Z_1 - Z_2)/(Z_1 + Z_2)$ is the elastic wave's reflection coefficient at a non-ideal interface. For frequencies that are much lower than f_0 , $R_{\rm eff} \approx R$, so the interface can be considered ideal.

For frequencies that are greater than f_0 , the value of the elastic wave's reflection coefficient is greater than for the ideal interface case, while the interface is described as non-ideal.

The calculations assumed the fact that the first few tens of picoseconds are not enough for the elastic pulse to propagate throughout the entire heterostructure, so the influence of layers and interfaces manifests itself over time, with different layers and interfaces influencing different parts of the response. This allows to sequentially expand the model by adding new layers to it while increasing the time interval over which the response is analyzed. Layer parameters obtained at the previous stages of calculations are considered to be known. Such technique of fitting-up allows to reduce the modeling time significantly and increase the reliability of parameter determination.

Results

Elastic response was measured in the sample regions having different compositions. Thus, far from the heterostructure, the

response is determined exclusively by the aluminum film and its interface with the Al₂O₃ substrate. As can be seen in Fig. 2a, arrival of the laser pulse was immediately followed by a short positive spike of 1–2 ps in duration, which was associated with strong heating of electrons by the pumping radiation, after which damped oscillations were developing smoothly. Two broad peaks can be clearly seen on frequencies of 35 and 120.5 GHz of the Fourier spectrum. These two lines are caused by vibrations of the aluminum film as a whole (low-frequency peak), as well as by with the presence of the elastic pulse repeatedly reflected from the film boundaries (high-frequency peak).

Highlighted in purple in Fig. 2a is the modeled response. The calculations allowed estimating the photothermal and photoelastic parameters of the aluminum film, as well as the equivalent stiffness of the interface between the film and the substrate (table). The estimated aluminum thickness (30 nm) perfectly agrees with the value measured with a quartz thickness gauge during the sputtering operation. The spectrum width (Fig. 2c) proved to be large for two reasons: due to the leakage of sound wave energy into the sapphire substrate, as well as due to the viscoelastic damping in the polycrystalline Al film (damping length is $1.25 \times 10^{17}/\omega^2$, m).

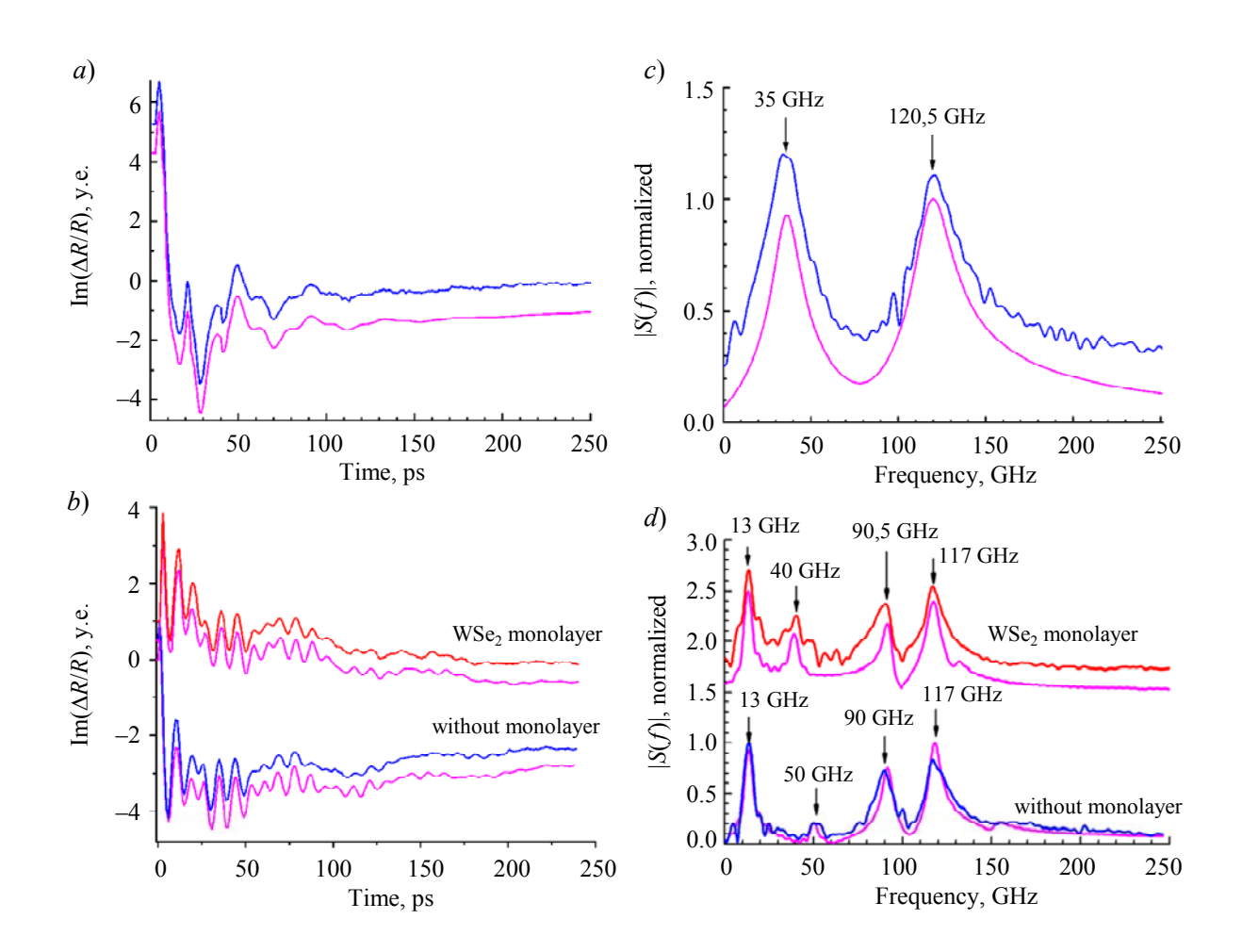


Fig. 2. Experimental dependencies of photoresponse (a and b) and their Fourier spectra (c and d) in the structures: Al/Al_2O_3 – (a and c); $Al/hBN/WSe_2$ (monolayer)/hBN/ Al_2O_3 (b and d, red curves) and $Al/hBN/hBN/Al_2O_3$ (b and d, blue curves). Highlighted in purple in all figures are calculated dependencies

Table

Calculated acoustic parameters of the interfaces under study.

AM stands for acoustic mismatch (ideal contact)

| Interface | Structure configuration | $\eta, 10^{18} \text{ N/mm}^3$ | f_0 , GHz |
|------------------------------------|--|--------------------------------|-------------|
| Al/Al ₂ O ₃ | Al/Al ₂ O ₃ | 8.7 ± 2.6 | 114 |
| Al/hBN | Al/hBN/hBN/Al ₂ O ₃ | 8.4 ± 0.6 | 258 |
| | Al/hBN/WSe ₂ (monolayer)/hBN/Al ₂ O ₃ | 2.0 ± 0.7 | 61.5 |
| hBN/Al ₂ O ₃ | Al/hBN/WSe ₂ (monolayer)/hBN/Al ₂ O ₃ | AP | |
| hBN/WSe ₂ | Al/hBN/WSe ₂ (monolayer)/hBN/Al ₂ O ₃ | AP | |

The responses from the heterostructure regions without the WSe_2 monolayer (Al/hBN/hBN/Al₂O₃, blue curve in Fig. 2b) and with the WSe₂ monolayer (Al/hBN/WSe₂) (monolayer)/hBN/Al₂O₃, red curve in Fig. 2b) have a more complex structure due to the elastic pulse propagation in the hBN layers and WSe₂ monolayer, and the elastic response damps more slowly. Their spectra prove to be more complex because reflections from both Al/hBN, hBN/WSe₂ and hBN/Al_2O_3 interfaces add to natural frequencies. The spectral lines become narrower both due to the increased acoustic length of the system and to the higher reflection coefficient at the hBN/Al₂O₃ interface. Additionally, characteristic and reproducible feature associated with the presence of the WSe₂ monolayer could be observed in these spectra. It consisted in the shift of the hBN collective mode from 50 GHz to 40 GHz (Fig. 2d).

Modeling of experimental responses showed that this feature of the spectra could described bv introducing into calculation model the δ-distributed mass $m = 1.4 \times 10^{-5} \text{ kg/m}^2$ that corresponds approximately two masses of the WSe₂ with monolayer, which well agrees photoluminescence measurements and Raman scattering spectroscopy results.

The sensitivity of the collective mode frequency to the WSe₂ monolayer is due to the sufficiently high value of complex reflection coefficient R^* of the δ -distributed mass:

$$R^* = \frac{if / f_0^*}{1 - if / f_0^*},$$

where $f_0^* = \frac{z}{\pi m}$, Z is the wave impedance of the WSe₂ monolayer environment. In this case $f_0^* \sim 160 \text{ GHz}$, and at f = 40 GHz $|R^*| = 0.25$.

Upon estimating the parameter of bond rigidity at the hBN interfaces with a WSe₂ monolayer, these interfaces were found to be described in terms of the ideal contact of layers accurately enough. As for the interface of two hBN layers, the coefficient of reflection from the boundary between them tuned to be equal to zero, that is, the acoustic contact is ideal, and two hBN layers are equivalent to one layer of the total thickness.

The derived feature of the spectrum not only characterizes the WSe₂ monolayer, but also reveals the spectrum sensitivity of the picoacoustic method to the heterostructure composition, the individual and to monolayers as well. To demonstrate this possibility graphically, the responses of the sample region outlined with a white frame in Fig. 3a were measured. Then their Fourier spectra were calculated, and the spatial distribution pattern of the modulus of the response spectral component at the frequency of 40 GHz was made, corresponding to the collective mode of the heterostructure with the WSe₂ monolayer (Fig. 3b). The structure region comprising the monolayer can be clearly seen in this image. This allowed to locate the WSe₂ monolayer spectrally. Thus, this research method supplemented by depth profiling of elastic properties which may be used as a tool of hypersonic tomography of such heterostructures.

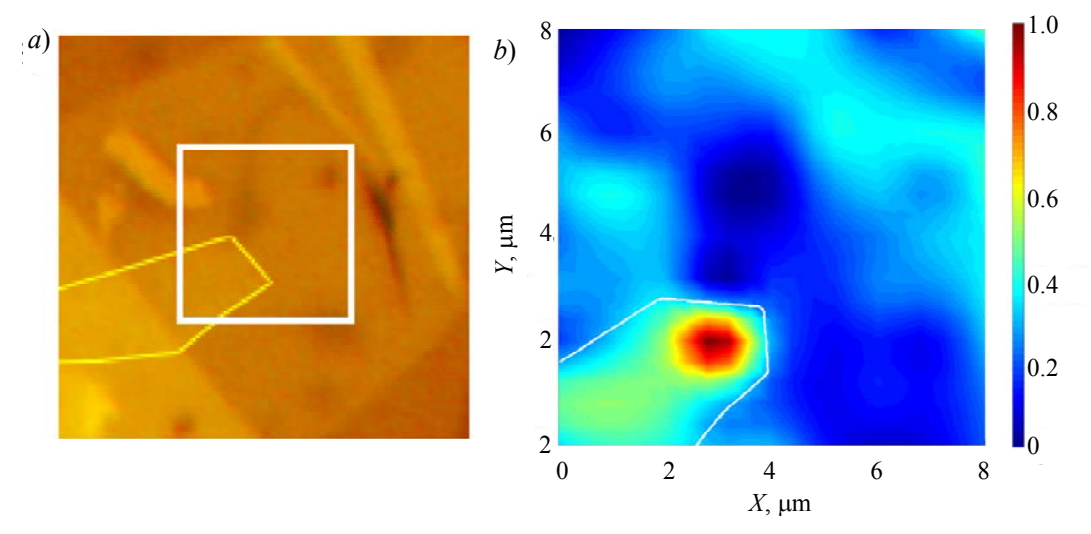


Fig. 3. a) – photo of the structure as seen in the optical microscope, the scanning area is outlined with a white frame; b) – map of the spectral component distribution at the frequency of 40 GHz within the outlined area

Conclusion

Here the elastic properties of the layered Al/hBN/WSe₂ heterostructure (monolayer)/hBN/Al₂O₃ were studied using optical pump-probe method. The the sensitivity of the method proved to be sufficient spectrally identify to monolayer. This allowed to locate the WSe₂ monolayer acoustically. Modeling of the structure response made enabled estimating the elastic parameters of the WSe₂ monolayer and hBN layers, in particular, determining the rigidity of van der Waals bonds at the structure interfaces.

The results obtained confirm the high potential of the picoacoustic method for characterizing van der Waals materials and heterostructures based on them.

The paper has been prepared with the financial support of the Russian Science Foundation (grant No. 23-22-00444).

REFERENCES

1. Vialla F. and Del Fatti N., Nanomaterials **10** (12), 2543 (2020).

- 2. Britnell L. et al., Science **335** (6071), 947–950 (2012).
- 3. Sup Choi M. et al., Nature communications **4** (1), 1624 (2013).
- 4. Lopez-Sanchez O. et al., Nature nanotechnology **8** (7), 497–501 (2013).
- 5. Lee H. S. et al., Nano letters **12** (7), 3695–3700 (2012).
- 6. Gomes L. C. and Carvalho A., Physical Review B **92** (8), 085406 (2015).
- 7. Chen Y. et al., Advanced Functional Materials **29** (41), 1900959 (2019).
- 8. Kim J. M. et al., Macromolecular Research **25**, 190–196 (2017).
- 9. Khan Z. H. et al., Journal of Physics D: Applied Physics **50** (5), 053003 (2017).
- 10. Fan X. et al., Microsystems & Nanoengineering **6** (1), 17 (2020).
- 11. Geim A. K. and Grigorieva I. V., Nature **499** (7459), 419–425 (2013).
- 12. Greener J. D. G. et al., ACS nano **13** (10), 11530–11537 (2019).
- 13. Greener J. D. G. et al., Physical Review B **98** (7), 075408 (2018).
- 14. Huang Y. et al., Nature communications **11** (1), 2453 (2020).
- 15. Pizzocchero F. et al., Nature communications **7** (1), 11894 (2016).
- 16. Klokov A. Y. et al., Nano Letters **22** (5), 2070–2076 (2022).
- 17. Tachizaki T. et al., Review of Scientific Instruments **77** (4), 043713 (2006).
- 18. Klokov A. Y. et al., Journal of Applied Physics **127** (15), (2020).

About authors

Nikolay Yurievich Frolov, junior research assistant, graduate student, Lebedev Physical Institute of the Russian Academy of Sciences (119991, Russia, Moscow, Leninsky Prospect, 53). E-mail: frolil199999@gmail.com SPIN code 1514-3041, Author ID 1288584

Andrey Yuryevich Klokov, leading research assistant, candidate of physics and mathematics, Lebedev Physical Institute of the Russian Academy of Sciences (119991, Russia, Moscow, Leninsky Prospect, 53). E-mail: klokov@lebedev.ru Author ID 121230

Andrey Ivanovich Sharkov, senior research assistant, candidate of physics and mathematics, Lebedev Physical Institute of the Russian Academy of Sciences (119991, Russia, Moscow, Leninsky Prospect, 53). E-mail: shark@sci.lebedev.ru Author ID 33305

Sergey Nikolayevich Nikolaev, senior research assistant, candidate of physics and mathematics, Lebedev Physical Institute of the Russian Academy of Sciences (119991, Russia, Moscow, Leninsky Prospect, 53). E-mail: nikolaev-s@yandex.ru SPIN code 6963-3322, Author ID 880828

Maxim Alexandrovich Chernopitsky, junior research assistant, candidate of physics and mathematics, Lebedev Physical Institute of the Russian Academy of Sciences (119991, Russia, Moscow, Leninsky Prospect, 53). E-mail: 66chemax@gmail.com SPIN code 6529-1510, Author ID 1219510

Semyon Igorevich Chentsov, research assistant, candidate of physics and mathematics, Lebedev Physical Institute of the Russian Academy of Sciences (119991, Russia, Moscow, Leninsky Prospect, 53). E-mail: semtch@gmail.com SPIN code 2361-8799, Author ID 1288583

Mikhail Vladimirovich Pugachev, junior research assistant, Lebedev Physical Institute of the Russian Academy of Sciences (119991, Russia, Moscow, Leninsky Prospect, 53). E-mail: m.pugachev@lebedev.ru

Alexey Vladimirovich Shupletsov, junior research assistant, Lebedev Physical Institute of the Russian Academy of Sciences (119991, Russia, Moscow, Leninsky Prospect, 53). E-mail: shuplecovav@lebedev.ru SPIN code 6413-3082, Author ID 1061429

Vladimir Svyatoslavovich Krivobok, leading research assistant, doctor of physics and mathematics, Lebedev Physical Institute of the Russian Academy of Sciences (119991, Russia, Moscow, Leninsky Prospect, 53). E-mail: krivobokvs@lebedev.ru. Author ID 135304

Alexander Yuryevich Kuntsevich, leading research assistant, doctor of physics and mathematics, Lebedev Physical Institute of the Russian Academy of Sciences (119991, Russia, Moscow, Leninsky Prospect, 53). E-mail: alexkun@lebedev.ru SPIN code 2192-4863, Author ID 160851

PHYSICAL SCIENCE OF MATERIALS

UDC 539.234, 621.793.18 PACS: 81.15.-z

EDN: RAHNOS

Synthesis of TiN coatings in Cu vapor on T15K6 alloy using the hybrid plasma technology

© A. P. Semenov, D. B.-D. Tsyrenov*, N. S. Ulakhanov, I. A. Semenova

Institute of Physical Material Science of the Siberian Branch of the Russian Academy of Sciences,
Ulan-Ude, 670047 Russia

* E-mail: dmitriyzak@mail.ru

Received 09.10.2024; revised 04.11.2024; accepted 26.02.2025 Scientific specialty code: 1.3.5

The synthesis of TiN coatings on T15K6 alloy in Cu vapor based on gas-discharge processes of vacuum-arc evaporation of Ti in nitrogen-containing plasma and magnetron ion-plasma sputtering of Cu is described. The following process parameters of the synthesis of TiN-Cu composite coatings have been determined: arc discharge current of 90 A, magnetron discharge glowing current of 0.5 A and voltage of 400 V, gas mixture pressure in the vacuum chamber of 2.4 Pa, growth surface temperature of 473 K, the synthesis time ~of 15 min, cleaning time of the substrate growth surface of 10 min, bias voltage of 160 V. Electron probe microanalysis of the structure confirms the copper content of ~5.57 at.% in the coatings under study over the entire coating profile. The microhardness of coatings is 38-42 GPa.

Keywords: gas discharge plasma; vacuum arc evaporation; ion-plasma sputtering; composite coating.

DOI: 10.51368/1996-0948-2025-2-97-102

Introduction

When synthesized with copper added, TiN-Cu coatings composite having structure nanocrystalline exhibit high hardness and plasticity [1, 2]. Cu atoms, when localized to form coating [1] along the boundaries of TiN crystallites, prevent the columnar structure of TiN crystallites from growing and lead to nanostructuring of superhard TiN-Cu coatings with an average grain size of ~20 nm. The dependence of the coating hardness on the copper content has a non-monotonic pattern. The maximum hardness value is achieved at relatively low copper concentrations [1] \sim (1–2) at. %, with a nanocomposite structure formed in the TiN coatings being synthesized.

Among the most advanced processes that allow high precision copper filling during synthesis of composite nanostructured TiN-Cu coatings, there are gas-discharge devices combining two gas-discharge processes: are evaporation of Ti and magnetron sputtering of

Cu, designed as a plasma-chemical reactor [3]. This combination has a potential enabling the controlled sizing of crystallites in a coating being built-up, which is extremely important because the nanostructure and, consequently, the microhardness and crack resistance of coatings are dependent on the concentration of an impurity component, the copper, to a certain extent. Controlling the parameters of vacuum arc and magnetron discharges while building up coatings [4, 5] facilitates controlling the ratio of evaporated and sprayed components.

This paper discusses the synthesis of TiN-Cu composite coatings based combination of the Τi vacuum-arc evaporation process and Cu magnetron sputtering process [3, 6, 7] and describes the surface microstructure of TiN-Cu composite coatings, their X-ray diffraction analysis, electron probe microanalysis and microhardness.

Experiment procedure

TiN-Cu composite coatings were synthesized in the vacuum chamber of the plasma-chemical reactor [3]. The vacuum chamber comprises vacuum-arc evaporator 1 and planar magnetron 2 (see Fig. 1). Vacuumarc evaporator 1 is positioned horizontally and provides the evaporation of the watercooled cathode by a cathode spot of vacuum arc discharge. The cathode has a 60-mm diameter and is made of titanium grade BT-1-0. The arc discharge current is 60-90 A, the pressure of working gas, nitrogen, is 2.6×10⁻¹ ¹–12 Pa, glowing voltage is 35-45 V. Planar magnetron 2 is positioned vertically. The magnetron power supply capacity is ~3 kW, the output voltage is up to 10^3 V. Water cooling of permanent magnets ensures stable operation of the magnetron.

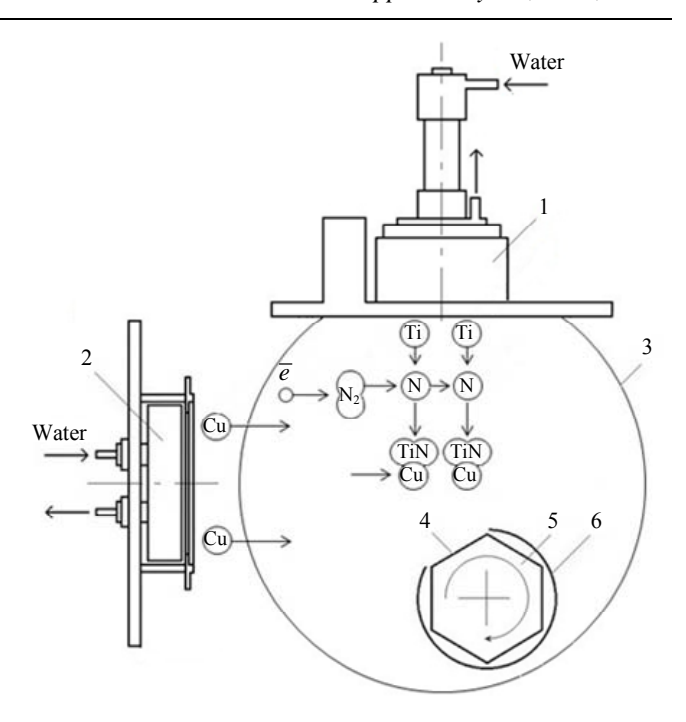


Fig. 1. Schematic diagram of the synthesis of TiN-Cu composite coatings: 1 – vacuum-arc evaporator; 2 – planar magnetron; 3 – vacuum-arc discharge plasma; 4 – substrates; 5 – substrate holder; 6 – screen

The sputtering rate of the copper target is controlled by the magnetron discharge power. The sputtering efficiency is controlled by adding ~20 % of argon to the total volume of the working nitrogen and argon mixture in the gas mixer. The magnetron supported the stable operation within the plasma-forming gas pressure range of 2.6×10⁻¹–12 Pa. The magnetron discharge current is 0.2-0.7 A. The discharge glowing voltage during the experiments was 340-450 V. The discharge glowing current and voltage depend on the pressure of the nitrogen and argon gas mixture. The distance from the evaporator cathode to the substrates 4 is 230 mm. Replaceable hexagonal plates of type 11114 (HNUM) as per GOST 19068-80 made of T15K6 hard alloy are used as substrates. Generally, they are used for straight-turning tools and end cutters. Drum-type substrate holder 5 allowed fastening up to

substrates. During building up of TiN-Cu coatings the growth surface of the initial substrate is oriented at an angle of 45° to the normals of the mutually perpendicular planes of the evaporated titanium cathode and sputtered copper cathode. Spare substrates shall be covered with screen 6. When the coating building-up is finished, the substrate holder rotates to an angle of 60° and the next substrate is extended out of the screen, opening the growth surface for building up a coating. The distance from the magnetron cathode to the substrate is within the range of The reference voltage of 120–140 mm. 160–180 V supplied to the substrate holder enables ion cleaning of the growth surface to inclusions: the surface remove gas preparation time is 4–10 min.

Findings and discussion

TiN-Cu composite coatings of ~6 μm in thickness were synthesized on substrates 4 (see Fig. 1) by initiating a chemical reaction between titanium vapor and atomic nitrogen in copper vapor, in conditions of dissociation in nitrogen-containing plasma 3 of molecular nitrogen $N_2 \leftrightarrow 2N$ by plasma electrons, vacuum-arc evaporation by a cathode spot of titanium vapour and ion-plasma sputtering of copper vapor. Process parameters of the synthesis: arc discharge current of 90 A, magnetron discharge glowing current of 0.5 A and voltage of 400 V, gas mixture pressure in the vacuum chamber of 2.4 Pa. At first, the hard alloy surface is cleaned, activated and heated up to ~473 K for ~10 minutes with metal-containing ions and plasma-forming gas ions, the bias voltage equaling to 160 V. The surface temperature of T15K6 hard alloy measured with TXA thermoelectric (chromel-alumel). transducer After that, under the synthesis process parameters, the achieved surface temperature of the hard

alloy is steady-state, and the TiN-Cu coating is synthesized for 15 minutes at a constant temperature of ~473 K.

Fig. 2 shows the surface microstructure of TiN-Cu composite coatings. The metallographic analysis of the TiN-Cu composite coating surface structure was performed using METAM PB-21 optical microscope equipped with VEC-335 digital camera and NEXSYS ImageExpert Pro 3.0 software package. The coating is uniform wit clear grain boundaries.

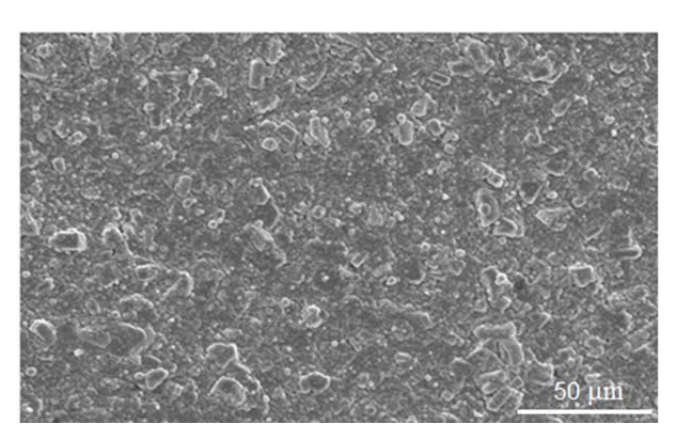


Fig. 2. Surface microstructure of TiN-Cu coating (500×magnification)

Fig. 3 shows the X-ray pattern of the TiN-Cu coating synthesized on the surface of T15K6 alloy. The X-ray phase analysis of the coatings was carried out by means of D2 diffractometer Phaser Bruker using LYNXEYE linear detector for powder and decoding of X-ray diffractography with DIFFRAC.EVA patterns software package with the ICDD PDF2 international database. According to the X-ray phase analysis completed, reflections of the TiN coating (111), (200), (202), (222), (311) having different crystal lattices and volume fractions are observed along with the WC reflections (001), (100), (101), (110), (002), (111), (200), (201), (112) and Ti_2C (111), (200), (202), (311), (222), (422) belonging to T15K6 alloy. According to the X-ray phase analysis, there are no copper reflections in the

composite layer. Whereas the electron probe microanalysis (electron probe microanalysis of the coating structure was performed using JSM-6510LV JEOL electron microscope (Japan) with INCA Energy 350 Oxford

Instruments microanalysis system (Great Britain)) of the coating structure confirms that there is copper in the coatings under study throughout the entire coating profile (see the table).

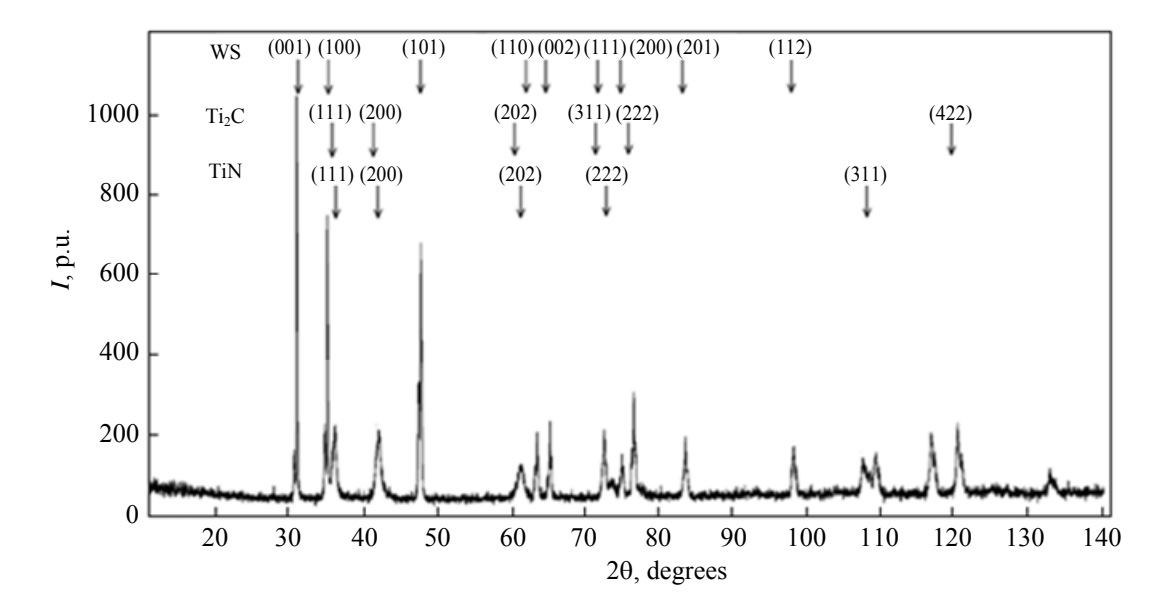


Fig. 3. X-ray pattern of TiN-Cu coating

Table Elemental composition (in at.%) of TiN-Cu coating

| No. | Al | Ti | Cu | W |
|------|------|-------|------|------|
| 8.91 | 0.23 | 79.81 | 5.57 | 5.48 |

Since copper does not form its own crystalline phase and is not part of the crystal lattice of other phases, it is probably located at the boundaries of crystallites in an amorphous or X-ray-amorphous state. As in [2, 5, 6], during the reaction of Ti and N in Cu vapor, copper is displaced to the boundary between TiN grains. Copper prevents the columnar structure of TiN crystallites from growing, thus contributing the nanostructuring of TiN-Cu composite coatings. On the one hand, it is shown by the low affinity of Cu for N. Nitrogen does not form compounds with Cu (copper does not directly combine with nitrogen; nitrogen nitride Cu₃N cannot be produced). On the

other hand, the phase diagram of the Ti-Cu system shows [8] that intermetallics are not formed steadily at low atomic percentages of copper; moreover, TiCu, Ti₂Cu, Ti₂Cu₃, TiCu₃ intermetallics are formed at high atomic percentages of copper and at temperatures of ~1073–1173 K. The time needed for copper atoms to form a closed shell around a growing TiN crystallite determines the growth duration of nanosized TiN crystallites, and, as a consequence, the size thereof.

The microhardness of the formed layers measured using ПМТ-3 M was microhardness tester equipped with a digital **NEXSYS** camera and **Image**Expert MicroHardness 2 program for indentation image processing as per GOST 9450-76 (using the Knoop indentation restoration method). The microhardness of coatings is 38-42 GPa.

Conclusion

TiN-Cu composite coatings of ~6 μm in thickness were synthesized on replaceable hexagonal plates of type 11114 (HNUM) as per GOST 19068-80 made of T15K6 hard alloy by initiating a chemical reaction between titanium vapor and atomic nitrogen in copper vapor, in conditions of dissociation in nitrogen-containing plasma of molecular nitrogen by plasma electrons, vacuum-arc evaporation by a cathode spot of titanium vapor and ion-plasma sputtering of copper vapor. The following process parameters of the synthesis of TiN-Cu composite coatings have been determined: arc discharge current of 90 A, magnetron discharge glowing current of 0.5 A and voltage of 400 V, gas mixture pressure in the vacuum chamber of 2.4 Pa, growth surface temperature of 473 K, the synthesis time ~of 15 min, cleaning time of the substrate growth surface of 10 min, bias voltage of 160 V. According to the X-ray phase analysis, there are no copper reflections in the composite layer. Electron probe microanalysis of the structure confirms the copper content of ~5.57 at.% in the coatings under study over the entire coating profile. The microhardness of coatings is 38–42 GPa.

According to the results of testing TiN-Cu coatings in real operating conditions under critical loads on replaceable hexagonal plates made of T15K6 and fixed on the straight-turning tool for cutting structural steel 40X on 16K20 screw-cutting lathe, the coatings did not fail (chips, peeling) in the contact area of the cutting tool, which is a clear evidence that the TiN-Cu coating strongly adheres to T15K6 hard alloy applied using the hybrid plasma technology. The test results confirmed that TiN-Cu coatings can be used as wear-resistant ones. In addition, the following pattern was established in [9]: TiN-Cu coatings with the Cu concentration of ~12 at.% and microhardness of up to 45 GPa feature a low friction coefficient (0.2), high adhesive strength to the metal and hard alloy

substrate (> 30 N), higher degree of strain recovery (< 50 %), high wear resistance $(< 2600 \, \mu m^3/N \cdot m)$, good thermal stability (up to 1373 K), and higher oxidation resistance (up to 1073 K).

Thus, the diverse applicability of the simplified technology for changing the structure and phase composition make allows composite superhard creating coatings that significantly increase the surface microhardness of straight-turning tools and end cutters made of T15K6 hard alloy.

The paper has been prepared as part of the state assignment of the Ministry of Science and Higher Education of the Russian Federation, research project

FWSF-2024-0010

REFERENCES

- 1. He J. L., Setsuhara Y., Shimizu I. Miyake S., Surface and Coatings Technology 137 (1), 38-42 (2001).
- 2. Ivanov Yu. F., Koval N. N., Krysina O. V., Baumbach T., Doyle S., Slobodsky T., Timchenko N. A., Galimov R. M. and Shmakov A. N., Surface and Coatings Technology 207, 430–434 (2012).
- 3. Semenov A. P., Tsyrenov D. B-D. Semenova I. A. A method and device for synthesizing TiN-Cu composite coatings. Patent for invention No. 2649355 (RF). 2017.
- 4. Myung H. S., Lee H. M., Shaginyan L. R. and Han J. G., Surface and Coatings Technology **163–164**, 591–596 (2003).
- 5. Myung H. S., Han J. G. and Boo J. H., Surface and Coatings Technology 177-178, 404-408 (2004).
- 6. Tsyrenov D., Semenov A. and Smirnyagina N., Acta Polytechnica 55 (2), 136–139 (2015).
- 7. Semenov A. P., Tsyrenov D. B-D. and Semenova I. A., Instrum. Exp. Tech. **60** (6), 892–895 (2017).
- 8. Eremenko V. N., Buyanov Yu. I. and Prima S. B., Powder Metallurgy and Metal Ceramics **5**, 494–502 (1966).
- 9. Krysina O. V. Generation of gas metal plasma in low-pressure arc discharges for synthesis of multicomponent nanocrystalline protective coatings: Diss. Candidate of Technical Sciences. Tomsk, IHCE SB RAS, 2016.

About authors

Alexander Petrovich Semenov, Professor, Doctor of Technical Sciences, Institute of Physical Materials Science of the Siberian Branch of the Russian Academy of Sciences (670047, Russia, Ulan-Ude, Sakhyanova str., 6). E-mail: alexandersemenov2018@mail.ru SPIN code 8786-3514, Author ID 1700

Dmitry Badma-Dorzhievich Tsyrenov, research assistant, Institute of Physical Materials Science of the Siberian Branch of the Russian Academy of Sciences (670047, Russia, Ulan-Ude, Sakhyanova, 6). E-mail: dmitriyzak@mail.ru SPIN code 2691-1766, Author ID 176491

Nikolay Sergeevich Ulakhanov, junior research assistant, Institute of Physical Materials Science of the Siberian Branch of the Russian Academy of Sciences (670047, Russia, Ulan-Ude, Sakhyanova, 6). E-mail: nulahanov@mail.ru SPIN code 8147-1096, Author ID 949665

Irina Alexandrovna Semenova, leading research assistant, Candidate of Technical Sciences, Institute of Physical Materials Science of the Siberian Branch of the Russian Academy of Sciences (670047, Russia, Ulan-Ude, Sakhyanova, 6). E-mail: irene_sem@mail.ru SPIN code 5260-0530, Author ID 132287

= INFORMATION =

Rules for submission, reviewing and publishing of scientific papers (as revised in 2025)

1. The "Applied Physics" journal is mainly intended for urgent publication of short papers concerning recent achievements in physics that have a potential of applied (technical and scientific) use. The journal is included in the new List of the Higher Attestation Commission, which came into effect on December 1, 2015.

By sending the article manuscript to the journal's editorial board, the authors grant the editorial board, founder and publisher of the journal a free, non-exclusive right to publish it in Russian as an article in the printed version of the journal, in the electronic version of the journal in the Internet and on laser disks. At the same time the authors retain their intellectual rights to the article manuscript (including "copyright"). In this regard and considering Part Four (Section VII) of the Civil Code of the Russian Federation, the authors shall submit a letter to the editor in the following form:

License agreement for transfer of the publish right (publishing license agreement)

| We, | the undersigned, the manuscript authors, | |
|---------------|---|------------|
| grant the ed | ditorial board, founder and publisher of "Applied Physics" journal a free, simple (non-exclusive) | license to |
| publish the | article manuscript in both printed and electronic journal versions. | |
| We o | confirm that this publication does not violate the intellectual rights of other persons or organizations. | Signatures |
| of authors: _ | (full name, academic degree, date) | |

The article shall be signed by all authors. If there are several authors, the name of the author responsible for message exchange with the editorial board shall be indicated. The article manuscript shall be sent to the address of the journal's editorial board: 111538, Moscow, Kosinskaya st, 9, AO NPO Orion, editorial board of "Applied Physics" journal or by e-mail: advance@orion-ir.ru

- 2. The article manuscript shall be submitted to the editor only in Russian.
- 3. The article manuscript shall be accompanied by an expert opinion whether its publication in the open media is allowed, which shall be drawn up in accordance with the established procedure.
- 4. The article size (including figures, bibliography and the English-language part) shall not exceed **7 pages** of A4 format with single line spacing. (A larger article is proposed to be sent to the affiliated "Applied Physics Advances" journal intended for publication of detailed articles and reviews). The article material shall be submitted in printed form (on paper) and in electronic form on a CD/DVD disk with the text in Word format (font type Times New Roman, font size 12), and the text shall already include figures with captions under them in the proper places. However, overly detailed and cumbersome mathematical transformations and expressions should be avoided in the text. The article styling shall be as follows:
 - title of the journal section;
 - UDK index;
 - PACS classification code (https://publishing.aip.org/wp-content/uploads/2019/01/PACS 2010 Alpha.pdf);
 - article title;
 - initials and surnames of authors;
 - abstract of the article (10–15 lines describing the purpose of the paper and its main findings);
 - keywords;
 - scientific specialty code.
- 5. The main text of the article shall begin with the "Introduction" section clearly stating the purpose and objectives of the paper along with arguments in favor of its preparation against the background of the existing state of the problem addressed in the article. The further text of the article shall also have meaningful headings (sections and subsections) without being numbered. The article shall end with a separate section, "Conclusion," listing the main findings, conclusions that follow from them, and, if possible, proposals for the research advance and use of its findings.

The bottom of the first page of the text shall accommodate a separate paragraph (in bold) containing contact information about the author (or authors) (mandatory section): surname, first name, patronymic (in full), e-mail (of all authors), profiles and registration numbers in scientometric databases (SPIN code, RINTS Author ID, ArXiv Author ID, Orcid ID, Scopus Author ID), academic degree, title, position, postal address of the enterprise).

Also a person responsible for message exchange with the editorial board shall be specified.

Authors can suggest potential reviewers (2–3 people by indicating their full name, place of work, and email address). The proposed candidates shall not work in the institutions where the authors do.

104 Information

The main text shall be followed by the list of references called "Bibliography".

Examples of designations of references used in the "Bibliography" section.

Articles shall be referred to as follows: Surname, initials, journal title, year, volume, issue, page numbers.

Ivanov I. I. / Applied Physics. 2022. No. 1. P. 12–18.

Lang D. V. / J. Appl. Phys. 1974. Vol. 45. No. 7. R. 3023-3034.

Reference to **books**: Surname, initials, book title, city, publisher, year. (When a specific chapter or page in a book is referred to, the page number is placed after the year.)

Korn G., Korn E. Mathematical Handbook. - Moscow: Nauka, 1974.

Biberman L. M., Vorobiev V. S., Yakubov I. T. Kinetics of non-equilibrium low-temperature plasma. – Moscow: Nauka, 1982. P. 371.

Ultraviolet technologies in the modern world / edited by Karmazinov F.V. Kostyuchenko S.V., Kudryavtsev N.N. – Dolgoprudny: Intellekt, 2012.

Reference to **conference proceedings:** Surname, initials, title of publication, place and date of publication, page numbers.

Romanov A. V., Stepovich M. A., Filippov M. N. / Proceedings of the XVII International Conference "Radiation Physics of Solids". – Sevastopol, 2007. P. 592–599.

Reference to patents: Surname, initials, title, type, number, year.

Davydov S. G., Dolgov A. N., Yakubov R. H. Vacuum spark gap. Patent of invention No. 2654494 (RF). 2018.

Reference to **dissertations and Abstracts**: Surname, initials, title of paper (abstract), diss. ... Candidate (Doctor) of Physics and Mathematics, city, organization, year.

Grechikhin V. A. Development and analysis of computer algorithms for processing single-particle signals of laser Doppler anemometers: Abstract from diss. by Candidate of technical sciences. – Moscow: MPEI, 1996.

Further, detailed English-language information about the article required for indexing the entire journal, the given article and its authors in international scientometric databases shall follow, namely: PACS, article title, authors' surname and initials (English transliteration), enterprise, its postal address, author(s) e-mail, abstract, keywords, references; since the journal is also distributed abroad, the editorial board reserve the right to correct the English part of the text without changing its meaning.

Styling of the References in the English part of the article has its own peculiarities. In particular, if the cited book or monograph is a translation into Russian from a foreign publication, the original data of this publication (authors, book title, publisher, city or country, year of publication) shall be given, as well as the Russian publisher and the year of publication in Russian. Given below are the main examples of designation of used references in the References section:

Article from the journal:

Ivanov I. I., Applied Physics, No. 1, 12–18 (2022) [in Russian].

Lang D. V., J. Appl. Phys. 45 (7), 3023–3034 (1974).

Note: if a Russian journal has a printed English analogue, the English title of the analogue shall be used and page numbers shall be taken therefrom. If there is no English analogue, the English transliteration of the Russian name shall be used.

Book:

Korn G. and Korn E., Mathematical Handbook. New York-London, Mcgraw-Hill Book Company, 1968; Moscow, Nauka, 1974.

Ultraviolet technologies in the modern world / ed. Karmazinov F. V., Kostyuchenko S. V., Kudryavtsev N. N. Dolgoprudny, Intellect, 2012 [in Russian].

Conference proceedings:

Romanov A. V., Stepovich M. A., and Filippov M. N. Proc. XVII Intern. Meeting on Radiation Physics of Solid State. Sevastopol, 2007, pp. 592–599.

Patents:

Davydov S. G., Dolgov A. N., Yakubov R. H. Vacuum spark gap. Patent for invention No. 2654494 (RF). 2018. **Dissertations and Abstracts**:

Grechikhin V. A. Development and analysis of computer algorithms for processing single-particle signals of laser Doppler anemometers: Abstract. Diss. Candidate of Technical Sciences. M., MEI, 1996.

6. The list of references ("References") shall correspond to all references to external sources used in the text of the article. These references shall be enclosed in square brackets, for example, [1–3], [7, 8]. Internal references, i.e. references to formulas, figures and tables of the article shall be enclosed in round brackets, for example, formula (3), equation (1), (Fig. 2), (Table 3). Any references in figure captions or in the figures are not recommended.

Information 105

7. The number of figures and photos for a typical article shall not exceed 4. If one figure contains two, three or more variants of graphic (or photo) images of the type "Fig. 2a", "Fig. 2b", etc., each individual variant is considered as a separate figure. If the above limit number of figures (photos) is exceeded, the article is sent back to the authors for revision. Graphics (black and white and color) shall be put directly in the proper place in the article and in the proper scale. Next to the graph axes, the displayed physical quantities shall be indicated only (strictly!) using symbols (letters), and after a comma - the quantity dimension in Russian (in direct font). It is recommended to number different curves on graphs, even if they are identified by a different color or line type. Graphs shall be submitted only (strictly!) against the white background. Auxiliary grids are not allowed in the graph area.

- 8. Captions under the corresponding figures shall be out in the proper places in the text. Each caption shall be as short as possible, but meaningful in terms of its content. Any physical (technical) symbol included in the caption shall have its verbal explanation there.
- 9. Simple formulas shall be included in the text in the format of the text editor used; more complex formulas shall included using MathType formula editor. Standard mathematical notations (e.g. max, log, sin, exp, etc.) shall be typed directly. The same is true about figures and numbers. Formula numbers shall written in parentheses on the right. To indicate non-vector physical (technical) quantities using symbols, use only the Latin and Greek alphabets, while using a straight font for Greek letters, and an oblique font (italics) for Latin letters in the text. Vectors and matrices shall be marked by a bold, upright font (preferred) or an arrow above the italic vector symbol (less preferred). For subscripts and superscripts, use Arabic numerals, Latin or Greek letters, but if the index, usually a subscript, is a short (abbreviated) form of the Russian characteristic word, it is allowed to use Russian letters in its designation (uppercase font), for example $U_{\rm in}$, $I_{\rm out}$, $v_{\rm gr}$, etc. The dimension of physical quantities shall be always given only in Russian, using an uppercase font.
- 10. Tables shall be made in accordance with the following requirements: the top line contains the data name and dimensions; the following lines contain the data itself.
- 11. Formulas, tables and figures shall have their own separate continuous numbering system. If there are no additional (return) references to a specific formula in the text or it is used only once, it shall not be numbered. A table and/or a figure used only once do not require numbering either.
 - 12. Manuscripts and CD/DVD will not be sent back by the editorial board.
- 13. Authors (or an author) of each article after it is published in a journal issue have a right to receive an electronic version of the article in PDF format (Adobe Acrobat editor) from the editorial board.
- 14. When published in the journal, each article is accompanied by a footnote with the copyright symbol © placed before the author's name (authors' names). The article shall also specify the date the article was received by the editorial board.

